

© Copyright by Zhigang Pan 2016

All Rights Reserved

SHALLOW WATER BATHYMETRY USING FULL
WAVEFORM BATHYMETRIC LIDAR AND
HYPERSPSPECTRAL IMAGERY

A Dissertation

Presented to

The Faculty of the Civil and Environmental Engineering

University of Houston

In Partial Fulfillment

of the Requirements for the Degree

Doctor of Philosophy

in Geosensing Systems Engineering and Sciences

By

Zhigang Pan

August 2016

SHALLOW WATER BATHYMETRY USING FULL
WAVEFORM BATHYMETRIC LIDAR AND
HYPERSPECTRAL IMAGERY

Zhigang Pan

Approved:

Chair of the Committee
Craig L. Glennie, Ph.D.
Assistant Professor
Civil & Environmental Engineering

Committee Members:

William E. Carter, Ph.D.
Professor and Senior Research Engineer
Civil & Environmental Engineering

Christopher E. Parrish, Ph.D.
Associate Professor
Civil and Construction Engineering
Oregon State University

Michael J. Starek, Ph.D.
Assistant Professor
School of Engineering and Computing Sciences
Texas A&M University at Corpus Christi

Juan Carlos Fernandez-Diaz, Ph.D.
Senior Scientist
Civil & Environmental Engineering

Suresh K. Khator, Ph.D.
Associate Dean
Cullen College of Engineering

Craig L. Glennie, Ph.D.
Geosensing Systems Engineering & Sciences
Program Director

Acknowledgments

This small piece of research was made possible only with the contribution from many great people and their selfless contribution. I would like to express sincere gratitude to my advisor, Dr. Craig Glennie, for his continuous support of my study and related research. His guidance and immense knowledge helped with all the time spent researching, sharing results through publications, and writing the dissertation.

I would also like to thank the director, Dr. Ramesh Shrestha, and all the staff of NCALM, Dr. Juan Carlos Fernandez-Diaz, Abhinav Singhanian, Micheal Sartori, and Darren Hauser, for their hard work collecting all the state-of-the-art LiDAR and hyperspectral imagery data to validate the research ideas. I want to give special thanks to Laura Murphy for organizing our lab and all the happiness she brought us. I would like to thank all the fellow graduate students in the Geosensing Systems Engineering and Sciences program. This paper cannot hold all of your names but I will remember all the happiness we had and the difficulties we went through. In addition, I also want to thank Dr. Carl Legleiter, Brandon Overstreet and Dr. Michael Starek for their helpful comments and the collection of field data used in my dissertation.

Last but not the least; I want to thank my family and friends for spiritually supporting me throughout writing this dissertation and my life in general.

SHALLOW WATER BATHYMETRY USING FULL
WAVEFORM BATHYMETRIC LIDAR AND
HYPERSPSPECTRAL IMAGERY

An Abstract
of a Dissertation

Presented to

The Faculty of the Civil and Environmental Engineering
University of Houston

In Partial Fulfillment
of the Requirements for the Degree
Doctor of Philosophy
in Geosensing Systems Engineering and Sciences

By
Zhigang Pan

August 2016

Abstract

High resolution airborne hyperspectral imagery and high resolution, low pulse energy bathymetric full waveform LiDAR were investigated in this dissertation to investigate their capabilities for predicting shallow water column characteristics and bathymetry.

A continuous waveform transformation method was proposed in this dissertation and compared with other commonly used full waveform processing algorithms. Both single wavelength and dual wavelength bathymetry systems were investigated and the results indicate that a multiwavelength system is superior to a single wavelength for shallow water bathymetry estimation. Significant improvements in point density, multiple return detection, and accuracy were determined for full waveform bathymetric LiDAR.

Support vector regression (SVR) was proposed to retrieve shallow water bathymetry from hyperspectral imagery and compared to an established band ratio method. SVR significantly improved the shallow water bathymetry for the two rivers studied. Water turbidity was also determined from hyperspectral imagery using SVR simultaneously.

The full waveform was further evaluated by using a methodology that voxelizes the original waveforms to generate orthowaveforms that were evaluated for estimating water bathymetry and turbidity. The orthowaveforms outperformed full waveform estimates and were also utilized to retrieve water turbidity. Finally, the fusion of hyperspectral imagery and orthowaveforms was investigated and slightly improved both shallow water bathymetry and water turbidity estimations over using either dataset alone.

The hyperspectral observations were also studied in conjunction with a semi-analytical model to retrieve water column constituent concentrations and bathymetry simultaneously for a coastal region. Both a nonlinear optimization method and a model based SVR method are introduced to estimate water constituents and bathymetry. The bathymetry estimated with these two methods were compared to both bathymetric LiDAR and field measured water depths. The results show both advantages and limitations for hyperspectral imagery

bathymetry retrieval. The fusion of bathymetric LiDAR and hyperspectral imagery was also performed; however, the accuracy evaluation was not performed due to the lack of field water constituent concentrations measurements. More studies to optimally fuse these two remote sensing techniques need to be performed in the future.

Table of Contents

Acknowledgments	v
Abstract	vii
Table of Contents	ix
List of Figures	xi
List of Tables	xiii
1 Introduction	1
1.1 Background	1
1.1.1 Shallow Water Hyperspectral Imagery	2
1.1.2 Airborne LiDAR Remote Sensing of Shallow Water	7
1.2 Motivations and Objectives	12
1.3 Document Structure	17
2 Theoretical Background	19
2.1 Optical Properties of Water	19
2.2 Radiative Transfer Processes	20
2.2.1 Semi Analytical Model of Water Leaving Reflectance	20
2.2.2 Simplified Radiative Transfer for Hyperspectral Imagery	23
2.2.3 Radiative Transfer for Airborne Bathymetric LiDAR	32
3 Study Sites and Datasets	41
3.1 Study Area Description	41
3.1.1 Rusty Bend of the Snake River	41
3.1.2 Confluence of the Blue and Colorado River	42
3.1.3 East Pass of Destin	43
3.2 Airborne Hyperspectral Imagery Datasets	44
3.3 Airborne Bathymetric LiDAR Datasets	49
3.4 Acoustic Doppler Current Profiler Data	52
3.5 Water Turbidity Data	54
4 Performance Assessment of High Resolution Airborne Full Waveform Li- DAR for Shallow River Bathymetry	57
4.1 Overview	57
4.2 Method and Mathematical Model	60
4.2.1 Continuous wavelet transformation	60
4.2.2 Gaussian decomposition method	63

4.2.3	Empirical System Response Waveform Decomposition	65
4.2.4	Water Depth Generation	66
4.3	Results	69
4.3.1	Experiment I: Snake River Bathymetry Study	69
4.3.2	Experiment II: Blue/Colorado River study	74
4.3.3	Best Performance for Single Band Bathymetric LiDAR	81
4.4	Discussion	83
5	Estimation of Water Depths and Turbidity from Hyperspectral Imagery Using Support Vector Regression	87
5.1	Overview	87
5.2	Support Vector Regression	88
5.3	Results	91
5.4	Discussion	93
6	Fusion of LiDAR Orthowaveforms and Hyperspectral Imagery for Shallow River Bathymetry and Turbidity Estimation	97
6.1	Overview	97
6.2	Generation of Orthowaveforms	98
6.3	Experimental Setup and Results	102
6.3.1	Snake River Bathymetry Estimation	104
6.3.2	Blue/Colorado River Bathymetry Estimation	106
6.3.3	Comparison of full waveform and orthowaveform for bathymetry	109
6.3.4	Blue/Colorado River Turbidity Estimation	110
6.4	Discussion	112
7	Radiative Transfer Modeling of Remote Sensing Observations to Determine Shallow Water Characteristics	116
7.1	Overview	116
7.2	Methods	118
7.2.1	LiDAR Bathymetry	118
7.2.2	Nonlinear Least Square Optimization (nLSQ)	119
7.2.3	Model based Support Vector Regression (mSVR)	121
7.3	Results	122
7.3.1	nLSQ	122
7.3.2	mSVR	126
7.3.3	Comparison of nLSQ, mSVR and Conventional SVR	129
7.3.4	Fusion of LiDAR and Hyperspectral Imagery	132
7.4	Discussion	136
8	Conclusions and Future Research Directions	139
8.1	Conclusions	139
8.2	Future Work Directions	143
	Bibliography	146

List of Figures

Figure 2.1	Maximum detectable depth for hyperspectral imagery.	29
Figure 2.2	Depth uncertainty for hyperspectral imagery shallow water bathymetry retrieval.	30
Figure 2.3	Water depth accuracy for hyperspectral imagery.	31
Figure 2.4	Maximum detectable depth for bathymetric LiDAR system with varying water attenuation characteristics.	38
Figure 3.1	Study areas and the field data for the Snake River and the Blue/Colorado River.	43
Figure 3.2	Study area and the field data for the East pass, Destin.	44
Figure 3.3	Airborne hyperspectral imaging sensor, CASI-1500.	45
Figure 3.4	Sun glint removal for the hyperspectral imagery.	49
Figure 3.5	Airborne bathymetric LiDAR, Optech Aquarius sensor.	50
Figure 3.6	Optech waveform digitizer.	51
Figure 3.7	Sontek River Surveyor S5 sensor.	53
Figure 3.8	Discharge rate at USGS gauge station on the Snake River.	54
Figure 3.9	Discharge rate at USGS gauge station on the Blue/Colorado River.	55
Figure 3.10	Histogram of ADCP measured water depths for the East Pass.	55
Figure 3.11	White sand field measured spectrum.	56
Figure 3.12	WET Labs EcoTriplet.	56
Figure 4.1	Preprocessing of bathymetric full waveform returns.	61
Figure 4.2	Bathymetric full waveform examples.	62
Figure 4.3	Schematic graphic for ESR method.	67
Figure 4.4	Definition of point to plane distance for water depth generation.	69
Figure 4.5	Distribution of the number of full waveform returns for the Snake River.	70
Figure 4.6	Comparison of LiDAR depths to ADCP depths for the Snake River.	71
Figure 4.7	Distribution of the number of full waveform returns for the Blue/Colorado River.	74
Figure 4.8	Comparison of LiDAR depth to ADCP depth for the Blue/Colorado River.	75
Figure 4.9	Individual waveform with CWT peaks and actual water surface locations.	79
Figure 4.10	Profiles for the Blue/Colorado River.	80
Figure 4.11	Profiles for the Snake River.	81
Figure 4.12	The optimum single band water depth map for the Snake River and the Blue/Colorado River.	82
Figure 5.1	Soft margin Support Vector Regression.	89
Figure 5.2	RMSE and R^2 of OBRA and SVR for the Snake River water depths.	92

Figure 5.3	RMSE and R^2 of OBRA and SVR for the Blue/Colorado River water depths.	93
Figure 5.4	RMSE with varying water depth for the Snake River water depths.	94
Figure 5.5	RMSE with varying water depth for the Blue/Colorado River water depths.	95
Figure 5.6	RMSE and R^2 for the Blue/Colorado River water turbidity.	96
Figure 6.1	Schematic generation of orthowaveforms.	100
Figure 6.2	3D image cubes for hyperspectral imagery and orthowaveforms of the Snake River.	100
Figure 6.3	Average hyperspectral spectrum and orthowaveforms for the Snake River.	101
Figure 6.4	3D image cubes for hyperspectral imagery and orthowaveforms of the Blue/Colorado River.	102
Figure 6.5	Average hyperspectral spectrum and orthowaveforms for the Blue/Colorado River with varying water depth.	103
Figure 6.6	Average hyperspectral spectrum and orthowaveforms for the Blue/Colorado River with varying water turbidity.	103
Figure 6.7	Water depth and error maps for the Snake River.	105
Figure 6.8	RMSE distribution of water depths for the Snake River.	106
Figure 6.9	Water depth and error maps for the Blue/Colorado River.	108
Figure 6.10	RMSE distribution of water depths for the Blue/Colorado River.	108
Figure 6.11	Water turbidity and error maps for the Blue/Colorado River.	111
Figure 6.12	RMSE distribution of water turbidity for the Blue/Colorado River.	112
Figure 7.1	LiDAR bathymetry and the field measured ADCP depths.	119
Figure 7.2	A example of semi analytical model inversion with hyperspectral spectrum.	120
Figure 7.3	Modeled spectra with varying water depth.	121
Figure 7.4	Sensitivity analyses to determine the optimal calibration sample size.	123
Figure 7.5	Hyperspectral imagery inversion results with nLSQ optimization.	124
Figure 7.6	Hyperspectral imagery inversion results with nLSQ optimization and LiDAR depths constraint.	125
Figure 7.7	Hyperspectral imagery derived results with mSVR estimation.	127
Figure 7.8	Hyperspectral imagery derived results with mSVR and LiDAR depths constrained estimation.	128
Figure 7.9	Depth maps of the East Pass derived from hyperspectral imagery.	130
Figure 7.10	Histograms of derived water depth errors.	131
Figure 7.11	Comparison of derived water depths with ADCP water depths.	132
Figure 7.12	Fitting goodness maps of nLSQ and mSVR methods.	134
Figure 7.13	Distribution of the standard deviations of estimated parameters.	135

List of Tables

Table 2.1	Wavelength dependent parameters in the bi-optical modeling.	24
Table 2.2	Bi-optical parameterization.	25
Table 3.1	Principal airborne acquisition parameters for the study areas.	46
Table 4.1	Comparison of LiDAR depths to ADCP water depths for the Snake River.	71
Table 4.2	Statistics of different water surfaces for the Snake River.	73
Table 4.3	Comparison of LiDAR depths to ADCP water depths for the Blue/Colorado River.	76
Table 4.4	Statistics of different water surfaces for the Blue/Colorado River.	77
Table 4.5	Statistics for the leading edge detected water surfaces.	80
Table 4.6	The best performance of the single band LiDAR bathymetry.	82
Table 6.1	Statistics for hyperspectral and orthowaveform derived bathymetry for the Snake River.	105
Table 6.2	Statistics for hyperspectral and orthowaveform derived bathymetry for the Blue/Colorado River.	107
Table 6.3	Comparison of full waveform processing and orthowaveform for deriving water depths.	109
Table 6.4	Statistics for hyperspectral and orthowaveforms derived water turbidity for the Blue/Colorado River.	111
Table 7.1	Parameter constraints and initial values for the nLSQ solution.	122
Table 7.2	Statistics of hyperspectral imagery derived bathymetry products.	130

Chapter 1

Introduction

1.1 Background

Mapping shallow water bathymetry is essential for monitoring benthic spatial and temporal change. The evolution of shallow inland fluvial systems, such as rivers and lakes, and near shore coastal zone environments are tightly interconnected with human environmental, agricultural and recreational activities on and near water bodies. Therefore, scientific, resource management, defense and other communities need tools and algorithms to efficiently map water bathymetry, column characteristics, and substrate composition (Marcus and Fonstad, 2010). The use of field platforms to measure and evaluate these environments has prevailed in the last century, but catchment research or large scale holistic views of entire ecosystems indicate that approaches such as remote sensing are more feasible techniques to assess current conditions (Mumby *et al.*, 1999).

Acoustic sonar is a common technique used to readily produce detailed bathymetric maps and can operate in water depths ranging from meters to thousands of meters. Acoustic sonar systems have been successfully used for applications such as submarine detection, shallow and deep water bathymetric mapping, and nautical charting (Wilson *et al.*, 2007; Costa *et al.*, 2009). However, it is financially ineffective to map shallow water using acoustic instruments due to the reduced swath with decreasing water depth, which increases acquisition costs significantly (Costa *et al.*, 2009; Guenther, 2006). The logistical difficulties and safety risks in deploying acoustic instruments in non-accessible areas further limit its applications (Guenther, 2006). In contrast, airborne optical methods, such as hyperspectral imagery and bathymetric LiDAR are commonly used for shallow water bathymetric mapping. Passive imagery and bathymetric LiDAR sensors are installed on either aircraft or spacecraft that provide fast and effective earth surface observations.

1.1.1 Shallow Water Hyperspectral Imagery

Passive multispectral imagery has been utilized to retrieve bathymetry and water column characteristics for several decades (Lyzenga, 1978; Philpot, 1989; Lee *et al.*, 1998, 1999; Brando and Dekker, 2003). Solar radiance reflects off the water surface and enters the water column where it is attenuated exponentially and then partially reflected from the benthic layer. The radiance arriving at the airborne or satellite platform is thus a composite of water surface, water column, and benthic layer reflections. The received spectrum for each pixel consequently varies with substrate types, water column characteristics and water depth. By analyzing the received spectrum, the relationship between received radiance and physical parameters of the shallow water can be established, allowing the retrieval of water depth, water column characteristics and benthic reflectance simultaneously.

Satellite platforms are a major source of multispectral imagery and have previously been shown to be effective in retrieving water bathymetry with moderate to high spatial resolution. Pacheco *et al.* (2015) utilized medium resolution Landsat 8 imagery to derive water depths for a near shore area. Lyons *et al.* (2011) applied Quickbird high resolution imagery to retrieve water bathymetry using two different methods. Eugenio *et al.* (2015) used Worldview-2 multispectral imagery to retrieve water bathymetry for two coastal areas. Paringit and Nadaoka (2012) simultaneously retrieved water benthic cover and bathymetry from high resolution IKONOS data. Satellite imagery is effective to routinely monitor shallow water areas with relatively low cost, but suffers from acquisition difficulties due to weather conditions (e.g. presence of clouds) and relatively coarse spectral and/or spatial resolution (Fonstad, 2012). The flexibility of satellite imagery is also limited due to the fixed orbits of the satellites. Generally, satellite imagery is a compromise between either spatial or spectral resolution due to the limited number of photons detected by high altitude satellite platforms (Fonstad, 2012). In contrast to spaceborne multispectral imagery,

airborne systems at lower altitude generally increase both spatial and spectral resolution, enabling hyperspectral imagery collection. Hyperspectral imaging systems take advantage of light diffraction to record the reflected radiance intensity at various wavelengths. The spatial resolution of airborne hyperspectral imagery is partially determined by the acquisition altitude, due to a fixed field of view; however, there is still a tradeoff between spatial and spectral resolution because a high signal-to-noise ratio for the acquired imagery is desired (Fonstad, 2012).

The algorithms to retrieve water bathymetry from multi/hyperspectral imagery have been well documented in the existing literature. Lyzenga (1978) and Philpot (1989) introduced a radiative transfer model of the water column and a linear solution for water bathymetry retrieval using principal component analysis. The numerical radiative transfer model developed and implemented by Mobley (Mobley, 1994), referred to as *Hydrolight*, computes radiance distribution and derives natural water characteristics. This numerical software is widely used in the ocean color remote sensing community, but it is a forward model and not invertible. Lee *et al.* (1998) therefore proposed a semi analytical radiative transfer model for water remote sensing, and the proposed optimization scheme has also been utilized to retrieve water bathymetry and column characteristics simultaneously (Lee *et al.*, 1999). However, the semi analytical method requires an extensive calibration process of the passive imagery to achieve optimal estimation, making it difficult to implement. To alleviate the calibration requirements, Dierssen *et al.* (2003) and Stumpf *et al.* (2003) proposed a band ratio method to retrieve water depths from hyperspectral imagery and declared its efficacy for being more sensitive to changes in bottom depth than in substrate composition. Legleiter *et al.* (2004) further reviewed the underlying radiative transfer theory in the passive hyperspectral remote sensing of water, and evaluated both linear and band ratio methods to retrieve water depths for inland shallow rivers. Legleiter *et al.* (2009) simplified the radiative transfer model for shallow water and proposed a statistical approach to

search for the optimal band pair for water depths retrieval. In addition to the semi analytical model, linear solution and band ratio method, machine learning has also been investigated for water bathymetry retrieval. Sandidge and Holyer (1998) retrieved water bathymetry from airborne hyperspectral imagery using a neural network approach. Pan *et al.* (2015a) proposed using the full image spectrum instead of a single pair of bands and combined that with the support vector regression method to determine both water bathymetry and turbidity from hyperspectral imagery.

Advantages of hyperspectral remote sensing

1. The most significant advantage of hyperspectral imagery is the high resolution of the available spectral observations. For benthic substrate classification, the numerous bands of hyperspectral imagery benefit both supervised and unsupervised classification to distinguish different species (Cui and Prasad, 2015). Apart from species classification, spectral unmixing is also enabled with hyperspectral imagery by investigating the spectral mixture of different species quantitatively, which is called a "soft classification" (Legleiter and Goodchild, 2005). In addition to classification, hyperspectral imagery has improved the derived water bathymetry compared to the multispectral imagery (Legleiter *et al.*, 2002); a statistical method determining the optimal bands for bathymetry retrieval is also enabled with hyperspectral imagery (Legleiter *et al.*, 2009). The semi analytical model that solves for the water column constituents concentrations also requires fine spectral observations with mathematical nonlinear optimization (Brando and Dekker, 2003; Lee *et al.*, 1999).
2. Logistically, airborne hyperspectral imagery has higher deployment flexibility compared to spaceborne systems that generally have fixed orbits. The flexibility highlights its efficacy for periodic environmental monitoring tasks and quick response to natural hazard events. In addition to the logistical advantages, the use of passive

imagery is well documented including several algorithms to qualitatively and quantitatively estimate environmental characteristics. Various biophysical and environmental applications have been successfully studied with hyperspectral imagery for coastal and fluvial environments. For example, Brando and Dekker (2003) estimated concentrations of chlorophyll, colored dissolved organic matter and suspended matter from hyperspectral imagery and Gitelson *et al.* (2009) estimated chlorophyll-a concentration in turbid water using a three-band and a two-band model.

Limitations of hyperspectral remote sensing

Despite the significant advantages of the fine spectral and spatial resolution of hyperspectral imagery, limitations are also highlighted in its application to a range of fluvial and coastal monitoring and estimation problems.

1. Field data is critical for hyperspectral remote sensing in order to optimally calibrate the physical environmental parameters to the image observations. Even though methods without using field data exist (Fonstad and Marcus, 2005; Legleiter, 2015; Lee *et al.*, 1999; Brando and Dekker, 2003), substantial tuning of parameters and iterative computations impose significant difficulties for bathymetry retrieval. More studies, on the contrary, suggest the increased use of field data properly compensate for the atmospheric correction and varying water column optical properties (Philpot, 1989; Legleiter *et al.*, 2009, 2015; Stumpf *et al.*, 2003; Dierssen *et al.*, 2003). The requirement for adequate calibration samples for relating hyperspectral observations to physical water depths is a significant constraint especially for dangerous and inaccessible regions. In addition water depths only are estimated from the hyperspectral imagery and an independent estimate of the water surface is needed to provide referenced elevations of the benthic layer.
2. Hyperspectral imagery records an estimate of the contiguous received radiance in

digital numbers, which is a discrete observation. However, the received radiance drops below the detector sensitivity for deep water. For a fixed sensitivity detector, hyperspectral imagery generates contour-like water bathymetry whose accuracy decreases significantly as water depth increases (Philpot, 1989; Legleiter *et al.*, 2004). The degraded bathymetry products in deeper water impedes its application for bathymetric mapping due to difficulties in satisfying the standards given by the International Hydrographic Organization (IHO) (IHO, 2008).

3. Hyperspectral imagery is a passive imaging technique, and in order to ensure maximum penetration of the water column, optimal data collection time is near solar noon when the local solar elevation angle is close to the maximum. In addition, an increased sun glint around the solar noon is likely to further influence hyperspectral imagery bathymetry retrieval. This physical limitation imposes an extra logistical constraint on hyperspectral imagery collection. Furthermore, the optimum weather condition for hyperspectral imagery is clear skies with the absence of excessive water vapor in the atmosphere.
4. The radiative transfer process for downwelling irradiance in the water column is complex because the substrate type, water column characteristics and depth all affect the remote sensing observation simultaneously (Mobley, 1994). The maximum penetration of solar light is limited due to water attenuation and therefore turbid water further impedes the application of hyperspectral imagery. Varying substrate types also effect the observations and the derived water depths (Legleiter *et al.*, 2009; Pan *et al.*, 2015a). To acquire an accurate bathymetry map, extra consideration of water column reflection and varying benthic composition is necessary.

1.1.2 Airborne LiDAR Remote Sensing of Shallow Water

Airborne bathymetric LiDAR systems emit green laser pulses to penetrate the water surface and the backscattered laser energy from the benthic layer is captured. The selection of a visible green laser is because the water column exhibits less attenuation at this wavelength and because a green laser source (frequency doubled Nd:YAG) and detector are commercially available (Guenther, 2006). With accurate time of flight measurements recorded by the LiDAR system, the range is determined using the constant speed of light in the water column. The spatial position of each target is derived by combining the range, scan angle of the laser beam and the navigational information provided by the Global Navigation Satellite System (GNSS) and Inertial Navigation System (INS) on board (Glennie *et al.*, 2013). The spatial resolution of LiDAR point cloud is dependent on the flight altitude, laser pulse repetition frequency (PRF), field of view, etc. (Fernandez-Diaz *et al.*, 2014). An airborne bathymetric LiDAR is generally coupled with a near-infrared laser scanning system in order to produce seamless topobathy products and accurate water surface estimates (Fernandez-Diaz *et al.*, 2014; Tuell *et al.*, 2010; Allouis *et al.*, 2010); however, only the green laser pulses are used to measure water bathymetry.

Bathymetric LiDAR has a long history of estimating bathymetry that dates back to the 1960s when a pulsed airborne laser profiling system was first used to measure water depths (Guenther *et al.*, 2000). The initial impetus for airborne laser hydrography was to detect submarines for the purpose of military defense, and the first report to the public was given by the Syracuse University Research Center in Hickman and Hogg (1969). International cooperation between Canada, USA, Sweden, and Australia brought airborne hydrographic LiDAR from the experimental stage to an operational stage in the early 1980s (Guenther, 1985). In the 1990s, the Scanning Hydrographic Operational Airborne LiDAR Survey (SHOALS) was delivered to the U.S. Army Corps of Engineers (USACE) by Optech, the

Laser Airborne Depth Sounder (LADS) was developed by Tenix in Australia, and the HawkEye system was developed by Saab Aerospace in Sweden. After several decades of development, airborne bathymetry LiDAR is now commonly commercially available in the form of large, low resolution deep water systems. High resolution shallow water airborne bathymetric LiDAR systems began to be commercially available in the early 21st century. At present, there are several commercial systems available worldwide, including: the Experimental Advanced Airborne Research LiDAR (EAARL-B) from U.S. Geological Survey (USGS); Chiroptera, Dual DragonEye, and HawkEye systems developed by Airborne Hydrography AB, Sweden; Aquarius, Titan and Coastal Zone Mapping and Imaging LiDAR (CZMIL) developed by Teledyne Optech, Canada; and the VQ-820G and VQ-880G systems developed by Riegl, Austria (McKean *et al.*, 2009; Kim *et al.*, 2015; Tuell *et al.*, 2010; Fernandez-Diaz *et al.*, 2014; Pfennigbauer *et al.*, 2011). The recent evolution of single photon LiDAR detectors coupled with a green laser source also shows promising potential for bathymetric mapping (Degnan and Field, 2014; Shrestha *et al.*, 2012; Cossio *et al.*, 2009). With the exception of the single photon, EAARL-B, Riegl VQ-820G and Optech Aquarius single wavelength sensors, all the other sensors are equipped with both a green and a near-infrared (NIR) bands lasers. However, the green laser is always produced by doubling the near-infrared (1064 nm) output of the NdYAG laser for the dual wavelengths systems.

Airborne bathymetric LiDAR systems have been shown to be safe, cost-effective and accurate through many years of operation in moderate water depths (<80 m) where conventional acoustic systems are less effective (LaRocque and West, 1999; Guenther, 2006). Irish and Lillycrop (1999) showed that laser remote sensing is an integral tool for coastal engineering by providing efficient bathymetric maps. Collin *et al.* (2008) derived both high accuracy bathymetry from the SHOALS system and used the bottom backscatter to derive

benthic characteristics by extracting statistical parameters. Wang and Philpot (2007) examined the use of features from bathymetric LiDAR to discriminate coastal substrate types successfully. McKean *et al.* (2009) introduced the EAARL system for surveys of channels and floodplains. Fernandez-Diaz *et al.* (2014) also showed the effectiveness of a new compact high resolution bathymetric LiDAR system in various topographic and bathymetric applications.

Depending on how the ranges to targets are determined, two types of bathymetric LiDAR systems are presently commercially available: discrete and full waveform LiDAR systems. Discrete LiDAR is a system that records both the position and intensity information for up to 5 returns for each outgoing laser pulse. The discrete LiDAR generally utilizes a constant fraction discriminator (CFD) technique to detect returns in the backscatter laser pulse in real time (Guenther, 1985). However, while CFD is routinely used for topographic surveys, it is less desirable for bathymetry because of factors such as sensitivity to pulse shape and signal baselines (Guenther *et al.*, 2000). By contrast, full waveform LiDAR systems digitize and record the entire backscattered signal history of the reflected laser energy for subsequent post processing. Currently, most bathymetric LiDAR systems are capable of digital waveform recording generally at a temporal resolution of one nanosecond. Instead of using CFD, a post-mission evaluation of the laser propagation is enabled with advanced signal processing techniques to estimate ranges and other associated parameters from the recorded digital full waveforms. For topographic applications, abundant studies have been conducted to investigate the capabilities of full waveform LiDAR. For example, Parrish *et al.* (2014) evaluated several full waveform shape parameters and correlated them to salt marsh vertical uncertainty. Rogers *et al.* (2015) further related the full waveform shape parameters to biological parameters of the salt marsh area. Wang and Glennie (2015) voxelized the full waveform and fused it with hyperspectral imagery to improve land cover classification. Full waveform LiDAR has also been analyzed for some studies related to

bathymetric mapping. Through post mission analysis of the return full waveform, a posterior investigation on each laser pulse is possible to enable the extraction of more benthic, water column and water surface returns and subsequently allow the derivation of water column characteristics (Tuell *et al.*, 2010). Allouis *et al.* (2010) used the full waveform return from the near infrared channel to compensate for the water surface reflection in the green laser channel and successfully extracted a better bathymetric product. Both increased point density and more multi-component returns from each outgoing laser pulse were acquired through the use of full waveform processing techniques in Pan *et al.* (2015b).

Advantages of airborne bathymetric LiDAR

Compared to hyperspectral imagery for bathymetry retrieval, airborne bathymetric LiDAR actively emits laser pulses to penetrate the water column, and this distinct characteristic has some advantages:

1. Direct measurements of water depths are acquired by airborne bathymetric LiDAR. LiDAR utilizes the laser time of flight in water to derive the water bathymetry with a constant speed of light in water. Field data is not required for data calibration, making the system ideal for areas where it is dangerous and difficult to access on the ground. LiDAR measures the water surface and benthic layer geographical positions instead of water depths, therefore the benthic layer can be more readily compared to various bathymetry products without the influence of tides.
2. The principle of airborne bathymetric LiDAR indicates that its positional accuracy is mainly dependent on the timing accuracy because of the constant speed of light in one specific water (Legleiter *et al.*, 2015). Despite the stretching effect of water turbidity on the return laser pulse, water turbidity has a negligible effect on the water bathymetry estimation.
3. Airborne bathymetric LiDAR actively emits laser pulses, and the stronger energy of

the laser (compared to passive solar radiation) allows LiDAR to be more resilient to water and weather conditions, such as vapor, haze, and strong water surface solar reflections. It is also possible to customize a specific LiDAR system for deeper water by increasing laser power or detector sensitivity. Logistically, bathymetric LiDAR can be deployed at any time of day because it is an active energy source. Furthermore, the resolution of airborne bathymetric LiDAR is flexible and can be planned before acquisition.

Limitations of airborne bathymetric LiDAR

Despite the outstanding advantages of determining water depth independently using bathymetric LiDAR, there are also several significant drawbacks with these systems.

1. A major technical limitation of current bathymetric LiDAR is its monochromatic characteristic. In contrast to passive hyperspectral imagery, the single (or in some cases 2 or 3) band intensity recorded by an airborne bathymetric LiDAR provides limited spectral information. Although the substrate type has been successfully classified using water depth and benthic intensity information (Wang and Philpot, 2007), a quantitative assessment of complex multi-benthic compositions is still challenging with bathymetric LiDAR. The return intensity is attenuated by the water column and is also difficult to calibrate due to the nature of laser propagation in water, especially when multiple returns are present (Wagner *et al.*, 2006).
2. The derived water LiDAR bathymetry performance is affected by both water column characteristics and substrate type. More turbid water theoretically results in more water column scattering that is non-linearly mixed with the benthic and water surface returns. An increase of water turbidity degrades detection of the water surface in single band bathymetric LiDAR, which then degrades the retrieved water depth

accuracy (Pan *et al.*, 2015b). Outgoing laser pulse width is also critical for discrimination of the water surface from a shallow benthic layer (< 1 m); longer pulse widths can cause complex overlap of the benthic return, water column return and water surface return, which results in additional uncertainty in water depth determination (Guenther *et al.*, 2000).

3. Due to the continuing development and system enhancements of airborne bathymetric LiDAR, the standard algorithms used to analyze either the recorded full waveform signal or discrete data are evolving. The irregular distribution of recorded points requires specialized algorithms that are different from the regularized grid techniques derived for image processing. In addition to the technical limitations, only a few operational bathymetric LiDAR exist worldwide, and the financial cost for a bathymetric LiDAR survey is still relatively high compared to hyperspectral imagery collection due to the lower altitude for the current bathymetric LiDAR.

1.2 Motivations and Objectives

Motivations

Determination of water bathymetry using remote sensing techniques requires optimal strategies to analyze and extract useful information. Hyperspectral imagery provides a fine observation of the spectral response of features and theoretically has the potential to determine water bathymetry independently. However, limitations for the current solutions are also obvious. The linear solution proposed by (Lyzena, 1978; Philpot, 1989) is difficult to implement in shallow water environments because of the deep water correction required, which is often difficult to estimate. The deep water pixels in shallow water generally have significant spectral contributions from the benthic layer that can influence bathymetry estimation. The band ratio method, given in Legleiter *et al.* (2009), Stumpf *et al.* (2003) and Dierssen *et al.* (2003), utilizes a pair of optimal bands to determine water bathymetry while

the other less-optimal bands containing less information are discarded. To fully exploit the capability of hyperspectral imagery in terms of bathymetry estimation and remove the need for a deep water correction, a method for determining shallow water bathymetry is proposed and implemented in this dissertation using all of the spectral features simultaneously to take full advantage of all the available bands in the hyperspectral imagery.

In contrast to the empirical methods for determining shallow water bathymetry statistically, the semi analytical model proposed in Lee *et al.* (1999) estimates both water column constituent concentrations and water bathymetry simultaneously. This model has been widely used in various applications to derive water column characteristics and water depth (Lee *et al.*, 1999, 2001; Brando and Dekker, 2003; Brando *et al.*, 2009; Torres-Madronero *et al.*, 2009, 2014; Jay and Guillaume, 2014, 2016). Its superiority has also been demonstrated in comparisons with several empirical and analytical techniques. A nonlinear least square based optimization approach is introduced in this dissertation to inverse hyperspectral imagery for water column characteristics and bathymetry retrieval. However, the inversion approach requires an extensive mathematical model with empirically derived approximations, field measured spectra, and extensive parameter tuning to achieve accurate results. On the other hand, machine learning has been explored extensively in recent years for recognizing patterns and predicting attributes (Cui *et al.*, 2012; Cui and Prasad, 2015; Chang and Lin, 2011; Ma *et al.*, 2010). The established correlation between bathymetry (and turbidity) and observed spectra suggest promise for using machine learning to perform shallow water remote sensing (Pan *et al.*, 2015a). A model based machine learning scheme is then proposed to examine the possibility of deriving water bathymetry and column characteristics simultaneously.

Discrete bathymetric LiDAR has been shown to be effective for deriving shallow water depths in previous studies (Guenther, 2006; McKean *et al.*, 2009). However, full waveform

LiDAR shows additional promise because it records temporal backscatter that enables posterior investigation of the laser pulse interaction with targets along the laser path. Full waveform records theoretically contain information regarding each target within the laser beam cone of diffraction. Therefore optimal full waveform processing strategies to extract the echoes contained in the full waveform record has the potential to improve bathymetry estimation. For longer pulse width LiDAR systems over shallow water environments, the resultant waveform is a complex superposition of water surface, column and benthic returns. Full waveform processing requires the application of advanced signal processing techniques to decouple the return laser pulse mixture. Thus, to fully exploit the capability of airborne bathymetric LiDAR for shallow water bathymetry, a full waveform processing strategy is proposed in this dissertation and the resultant performance is examined.

Recent developments for producing voxelized waveforms from the individual recorded full waveform returns has been applied to different applications (Park *et al.*, 2014) and shown improved land cover classification accuracy (Jung and Crawford, 2012; Wang and Glennie, 2015). A voxelized waveform generally requires multi-angle scanning of the target object to create a synthesized voxelized waveform due to changes in geometrical properties with look angle (Wang and Glennie, 2015). However, water is a distinct object that is heterogeneous from any direction due to its near homogeneous attenuation in principle (Park *et al.*, 2014). A voxelized waveform strategy is introduced in this dissertation to produce an orthorectified waveform to remove the effect of direction on scanning. The voxelized waveform is then examined to estimate both shallow water bathymetry and water turbidity individually using a machine learning algorithm.

The prior listing of pros and cons for both hyperspectral imagery and bathymetric LiDAR allows us to conclude that each optical remote sensing technique has distinct advantages and limitations. The extensive spectral observations of hyperspectral imagery should be able to compensate for the single band spectral observations from bathymetric

LiDAR. In addition bathymetric LiDAR provides direct measurements of water depth that can be used to calibrate the empirical models used for processing of hyperspectral imagery. Therefore, an evaluation of fusion techniques to combine these two remote sensing observations for optimal bathymetry estimation is also performed. Fusion of these two sensors has been previously developed in remote sensing communities for both topographic and bathymetric applications. Statistical methods that fuse LiDAR and hyperspectral imagery in a feature space are common in topographic and forestry applications. For example, Dalponte *et al.* (2008) demonstrated an improved tree species classification with fusion of LiDAR and passive imagery data; Wang and Glennie (2015) used the fusion of full waveform LiDAR and hyperspectral imagery to enhance land cover classification significantly. In terms of coastal or fluvial applications, the fusion of hyperspectral imagery and LiDAR also improves the shallow water bathymetry significantly. Spectral physics based fusion strategies that consider the distinct characteristics of these two remote sensing techniques for derivation of both bathymetry and water column characteristics have been partially explored but are not common. For example, Torres-Madronero *et al.* (2009) showed the increase in accuracy of bioptical parameters estimation using the fusion of hyperspectral imagery and bathymetric LiDAR. Torres-Madronero *et al.* (2014) presented the fusion of both hyperspectral imagery and LiDAR derived bathymetry for improved benthic habitat unmixing. Similarly, Tuell *et al.* (2010) gave an overview of the advanced bathymetric LiDAR system: Coastal Zone Mapping and Imaging LiDAR (CZMIL) which has integrated these two optical remote sensing techniques for a more enhanced bathymetric solution, although specific algorithmic details were not provided. The use of laser beam attenuation coefficients derived from bathymetric full waveform was used to correct benthic return intensity, and therefore the resultant LiDAR return intensity, water attenuation and depths were fused with hyperspectral imagery as constraints to solve an optimization for water

column characteristics (Tuell and Park, 2004). It is difficult to acquire water column attenuation coefficients from full waveforms using compact LiDAR systems, especially for shallow water due to the complex mixture of water surface and benthic layer returns. The underlying optical physics in hyperspectral imagery and bathymetric LiDAR, however, still suggest that there are benefits to fusing these two optical remote sensing techniques. This fusion, for shallow waters, will be explored in this dissertation.

Objectives

Drawn from the motivations, the objectives of this dissertation are to propose and evaluate different methods for water bathymetry retrieval from hyperspectral imagery and airborne bathymetric LiDAR. The strategies and performance of each approach are examined individually, and the fusion of these two optical remote sensing techniques are introduced and evaluated in the dissertation. The original contributions of this dissertation lie in the following areas:

1. A full waveform LiDAR processing strategy is proposed to extract more points and multi-component returns and evaluate its performance; the comparison of several full waveform processing strategies is performed to investigate the optimal solution.
2. A machine learning strategy for retrieving shallow water bathymetry from hyperspectral imagery is proposed and compared to the commonly applied band ratio method. The proposed method is also utilized to estimate water turbidity from hyperspectral imagery.
3. A voxelized waveform strategy is proposed and evaluated for shallow water bathymetry retrieval. The voxelized waveform is also examined for retrieval of water turbidity. The comparison of voxelized waveform, full waveform and hyperspectral imagery for shallow water bathymetry is also performed.

4. A semi analytical spectrum model is introduced and a model based machine learning strategy is proposed and compared to the nonlinear least squares method. Various hyperspectral water bathymetry products are compared to both LiDAR and field measured water depths.
5. Different data fusion strategies are examined and the comparison to the performance of each single data set alone is presented to investigate its significance.

1.3 Document Structure

The document is structured to provide background details on how to improve shallow water bathymetry estimation from both airborne bathymetric LiDAR and hyperspectral imagery alone, and by fusion of these two remote sensing techniques. The two instruments performance in terms of bathymetry and water column characteristics estimation were evaluated independently and as a fused set. Therefore, the rest of dissertation is structured as follows:

- Chapter 2 reviews the radiative transfer models for hyperspectral imagery and airborne full waveform bathymetric LiDAR. The theoretical investigation of maximum penetration water depth as well as an accuracy analysis of each sensor is given.
- Chapter 3 introduces the study sites and all the data used in this dissertation, including hyperspectral imagery data, bathymetric LiDAR data and various types of *in-situ* field measurements;
- Chapter 4 presents the algorithm proposed for full waveform analysis and comparison to different waveform decomposition algorithms against discrete LiDAR outputs, and is based on the work presented in Pan *et al.* (2015a);
- Chapter 5 presents the algorithm proposed for hyperspectral imagery bathymetry and water turbidity retrieval and the comparison to a common band ratio method, and is

based on the work presented in Pan *et al.* (2015b);

- Chapter 6 presents a voxelization of bathymetric full waveforms and its application for deriving water depths and turbidity and comparison to hyperspectral imagery derived results. A feature fusion is also given to show enhanced bathymetry and turbidity estimates, and is based on the work presented in Pan *et al.* (2016b)
- Chapter 7 presents the inversion of hyperspectral imagery for bathymetry and water column constituent concentration estimation using a semi analytical model. A model based support vector regression method is also given and compared to the semi analytical model inversion. Various bathymetry products are compared to the LiDAR bathymetry and field measured water depths.
- Chapter 8 provides conclusions and gives future research directions.

Chapter 2

Theoretical Background

2.1 Optical Properties of Water

The optical properties of water are critical to understanding light propagation in the water column. Dissolved organic and inorganic matter in the water and non-dissolved suspended particles simultaneously influence the observed light field of water. Consequently, the optical properties, especially for natural waters, show temporal and spatial variations and seldom resemble pure water. The optical spectra also reflect the environmental and biophysical properties of the natural waters.

The general optical properties of water can be divided into two categories: inherent optical properties (IOPs) and apparent optical properties (AOPs). IOPs are properties dependent only upon the propagation medium and therefore are invariant to the ambient light field present. Absorption coefficients, beam attenuation coefficients and volume scattering functions are examples of IOPs (Mobley, 1994). Scattering coefficients, such as forward and backward scattering coefficients, are drawn from the volume scattering functions that determine the natural water color. AOPs are properties that depend both on the water medium (IOPs) and also on the geometric structure of the ambient light field present (Mobley, 1994). Diffusive attenuation coefficients and observed radiance reflectance are common AOPs used to describe water bodies. Both IOPs and AOPs are wavelength dependent and can be used to describe a specific water body that displays spectral features and stability. The IOPs and AOPs are also tightly related to the water column properties and enable the derivation of many biophysical and ecological parameters, such as the chlorophyll and dissolved organic matter concentrations (Lee *et al.*, 1998; Brando and Dekker, 2003; Gitelson *et al.*, 2009). The goal of this chapter is to give the basic theoretical radiative transfer models used in the subsequent experimental analysis. Therefore, the definitions

of IOPs and AOPs are given here for the express purpose of developing the theoretical analysis of the radiative transfer models used in this dissertation, but the detailed description, physical definitions and experimental measurements can be found in the literature, for example, Mobley (1994).

2.2 Radiative Transfer Processes

Radiative transfer describes the physical propagation of electromagnetic energy in a medium. For radiative transfer in water bodies, both absorption and scattering affect the propagated energy by different physical processes. Consequently, the passive nature of hyperspectral imaging and the active nature of airborne bathymetric LiDAR show distinct differences in radiative transfer properties. This chapter introduces these two different remote sensing techniques and highlights the differences in the radiative transfer processes that physically govern the interaction between incident radiance and aquatic environments.

2.2.1 Semi Analytical Model of Water Leaving Reflectance

Passive multi/hyperspectral remote sensing of water measures the visible and near infrared reflected solar radiance that interacts with the water surface, column and benthic layer. Radiative transfer for passive remote sensing has been established primarily by oceanographers and remote sensing scientists (Mobley, 1994; Lee *et al.*, 1998). Various atmospheric and water column constituents transform the incident irradiance both spectrally and geometrically. A directional radiance is generally used to describe the underlying propagation in both atmospheric and water mediums. A portion of the downwelling irradiance is reflected by the water surface and the magnitude is described by the Fresnel equation. The remaining radiance propagates into the water column at a refraction angle described by Snell's law.

IOPs and AOPs are commonly used to describe the effect of the water on radiance

propagation. Light is attenuated exponentially with the distance traveled in the water at an attenuation rate and spectral shape determined as a function of various IOPs and AOPs present in solution (Legleiter *et al.*, 2004). The water constituent, such as chlorophyll, color dissolved organic matter and suspended sediments affect the IOPs; Lee *et al.* (1998) gives an analytical model that connect the physical environmental characteristics to subsurface remote sensing reflectance as

$$r(\lambda) = r_{\infty}(\lambda)(1 - \exp(-(k_d(\lambda) + k_u^c(\lambda))d)) + \frac{R_{0,B}(\lambda)}{\pi} \exp(-(k_d(\lambda) + k_u^b(\lambda))d), \quad (2.1)$$

where $r_{\infty}(\lambda)$ is the subsurface deep water remote sensing reflectance; $k_d(\lambda)$ is the water attenuation for the downwelling irradiance; $k_u^b(\lambda)$ is the water attenuation for the upwelling irradiance after interacting with the benthic layer and $k_u^c(\lambda)$ has no interaction with the benthic layer accordingly. Lee *et al.* (1998) assumes that $k_u^b(\lambda)$, $k_u^c(\lambda)$, $k_d(\lambda)$ are different due to different photon origination and path lengths. $R_{0,B}$ is the normalized benthic layer albedo, d is the physical water depth.

The attenuation coefficients $k_d(\lambda)$, $k_u^b(\lambda)$, $k_u^c(\lambda)$ and the deep water column reflectance $r_{\infty}(\lambda)$ are given by Lee *et al.* (1998) empirically as

$$k_d(\lambda) = \frac{a(\lambda) + b_b(\lambda)}{\cos(\theta_s)}, \quad (2.2)$$

$$k_u^b(\lambda) = \frac{1}{\cos(\theta_v)} (1.04(a(\lambda) + b_b(\lambda))) (1 + 5.4 \frac{b_b(\lambda)}{a(\lambda) + b_b(\lambda)})^{0.5}, \quad (2.3)$$

$$k_u^c(\lambda) = \frac{1}{\cos(\theta_v)} (1.03(a(\lambda) + b_b(\lambda))) (1 + 2.4 \frac{b_b(\lambda)}{a(\lambda) + b_b(\lambda)})^{0.5}, \text{ and} \quad (2.4)$$

$$r_{\infty}(\lambda) = (0.084 + 0.17 \frac{b_b(\lambda)}{a(\lambda) + b_b(\lambda)}) \frac{b_b(\lambda)}{a(\lambda) + b_b(\lambda)}, \quad (2.5)$$

where $a(\lambda)$ and $b_b(\lambda)$ are the absorption and backscattering coefficients and θ_s and θ_v are the solar zenith angle and the view angle. The inherent optical properties ($a(\lambda)$ and $b_b(\lambda)$) are also modeled to include water column constituents concentrations:

$$a(\lambda) = a_w(\lambda) + (a_0(\lambda) + a_1(\lambda) \ln(0.06 C_{CHL}^{0.65})) 0.06 C_{CHL}^{0.65} + C_{CDOM} \exp(-S_{CDOM}(\lambda - \lambda_0)) + C_{NAP} a_{NAP}^*(\lambda_0) \exp(-S_{NAP}(\lambda - \lambda_0)), \text{ and} \quad (2.6)$$

$$b_b(\lambda) = b_{b,w}(\lambda) + C_{CHL} b_{b,CHL}^*(\lambda_1) \left(\frac{\lambda_1}{\lambda}\right)^{Y_{CHL}} + C_{NAP} b_{b,NAP}^*(\lambda_1) \left(\frac{\lambda_1}{\lambda}\right)^{Y_{NAP}}, \quad (2.7)$$

where the subscript w is related to the pure sea water, $\lambda_0 = 440$ nm and $\lambda_1 = 542$ nm, C_{CHL} is the concentration of chlorophyll-a (CHL) ($\mu g \cdot L^{-1}$), C_{CDOM} is the a measure of the concentration of colored dissolved organic matter (CDOM) (m^{-1}), C_{NAP} is the concentration of non algal particles (NAP) ($mg \cdot L^{-1}$), $b_{b,CHL}^*(\lambda_1)$ is the backscattering coefficient at the reference wavelength of chlorophyll-a, S_{CDOM} and S_{NAP} are the spectral slope constants for CDOM and NAP respectively, a_{NAP}^* and b_{NAP}^* are the specific absorption and backscattering at the reference wavelength for NAP, Y_{CHL} and Y_{NAP} are the power law exponents for the CHL and NAP, $a_w(\lambda)$ and $b_{b,w}(\lambda)$ are the pure sea water absorption and backscattering spectra respectively, and are given by Richardson and LeDrew (2006), Pope and Fry (1997) and Morel (1974), $a_0(\lambda)$ and $a_1(\lambda)$ has been reported in Lee *et al.* (1999) and the rest of the parameters are taken from Brando *et al.* (2009) (see Table 2.1 and 2.2).

Due to the reflection of return radiance at the water-air interface, the above water

surface reflectance ($R(\lambda)$) is modeled from the subsurface reflectance as

$$R(\lambda) = \frac{0.5r(\lambda)}{1 - 1.5r(\lambda)}, \quad (2.8)$$

where $R(\lambda)$ is the above surface remote sensing reflectance.

The semi analytical model above describes the correlation of water column characteristics and observed remote sensing reflectance. The influence of atmospheric and water surface are not modeled and therefore a well-developed atmospheric correction and sun glint removal methods are essential to perform hyperspectral imagery inversion. This semi analytical model is established through the simulation results of HydroLight, which utilizes numerical methods and is not invertible. The significance of the semi analytical model is that it makes it possible to inversely derive water column characteristics and bathymetry simultaneously.

2.2.2 Simplified Radiative Transfer for Hyperspectral Imagery

The semi analytical model given in Equation 2.1 contains a significant number of empirical parameters making the tuning process for a specific dataset practically quite difficult. The requirement for accurate water leaving remote sensing reflectance spectra further limits its application. A priori known benthic type and spectra is also necessary to estimate the normalized benthic albedo. To introduce and generalize radiative transfer in the shallow water column, a simplified irradiance reflectance model described in (Lyzenga, 1978; Philpot, 1989) is summarized and given here as

$$\begin{aligned} R(0^-) &= R_\infty[1 - \exp(-gd)] + A_d \exp(-gd) \\ &= R_\infty + (A_d - R_\infty) \exp(-gd), \end{aligned} \quad (2.9)$$

Table 2.1 Wavelength dependent parameters in the bi-optical modeling (Richardson and LeDrew, 2006; Pope and Fry, 1997; Morel, 1974; Lee *et al.*, 1998, 1999, 2001).

wavelength (nm)	a_w	b_w	a_0	a_1
390	0.00851	0.0084	0.5813	0.0235
400	0.00663	0.0076	0.6843	0.0205
410	0.00473	0.0068	0.7782	0.0129
420	0.00454	0.0061	0.8637	0.0064
430	0.00495	0.0055	0.9603	0.0017
440	0.00635	0.0049	1.0000	0.0000
450	0.00922	0.0045	0.9634	0.0060
460	0.00979	0.0041	0.9311	0.0109
470	0.01060	0.0037	0.8697	0.0157
480	0.01270	0.0034	0.7890	0.0152
490	0.01500	0.0031	0.7558	0.0256
500	0.02040	0.0029	0.7333	0.0559
510	0.03250	0.0026	0.6911	0.0865
520	0.04090	0.0024	0.6327	0.0981
530	0.04340	0.0022	0.5681	0.0969
540	0.04740	0.0021	0.5046	0.0900
550	0.05650	0.0019	0.4262	0.0781
560	0.06190	0.0018	0.3433	0.0659
570	0.06950	0.0017	0.2950	0.0600
580	0.08960	0.0016	0.2784	0.0581
590	0.13510	0.0015	0.2595	0.0540
600	0.22240	0.0014	0.2389	0.0495
610	0.26440	0.0013	0.2745	0.0578
620	0.27550	0.0012	0.3197	0.0674
630	0.29160	0.0011	0.3421	0.0718
640	0.31080	0.0010	0.3331	0.0685
650	0.34000	0.0010	0.3502	0.0713
660	0.41000	0.0008	0.5610	0.1128
670	0.43900	0.0008	0.8435	0.1595
680	0.46500	0.0007	0.7485	0.1388
690	0.51600	0.0007	0.3890	0.0812
700	0.62400	0.0007	0.1360	0.0317
710	0.82700	0.0007	0.0545	0.0128
720	1.23100	0.0006	0.0250	0.0054

Table 2.2 Bi-optical parameterization (Brando *et al.*, 2009; Jay and Guillaume, 2014).

S_{CDOM}	0.0157
S_{NAP}	0.0107
λ_0	440
λ_1	542
$a_{NAP}(\lambda_0)$	0.0048
$b_{b,CHL}^*(\lambda_1)$	0.00038
$b_{b,NAP}^*(\lambda_1)$	0.0054
Y_{CHL}	0.681
Y_{NAP}	0.681

where $R(0^-)$ is the irradiance reflectance immediately below the water surface for optically shallow, vertically homogeneous water, R_∞ is the irradiance reflectance of an optically deep water column, g is an effective attenuation coefficient of the water ($g \approx 2K_d$), d is the water depth, $A_d = E_u(d)/E_d(d)$ is the irradiance reflectance of the bottom and $E_u(d)$ and $E_d(d)$ are the upwelling and downwelling irradiance at depth d .

By including factors to account for air-water transmittance, atmospheric effects and illumination, the above equation is transformed into an equation describing the radiance observed at the remote detector (Philpot, 1989; Legleiter *et al.*, 2009)

$$L_d = C_0 T_a (A_d - R_\infty) \exp(-gd) + T_a [C_0 R_\infty + \rho_a L_k] + L_p, \quad (2.10)$$

here, L_d is the radiance observed at the remote detector; C_0 is the downward spectral radiance, T_a accounts for the atmospheric transmission, ρ_a is the Fresnel reflectance of the air-water interface, L_k is the sky radiance, and L_p is the atmospheric path radiance.

The radiance received at the remote sensing platform from Equation 2.10 can be generally described as (Philpot, 1989; Legleiter *et al.*, 2004):

$$L_d = L_b \exp(-gz) + L_w \quad (2.11)$$

with

$$\begin{aligned} L_b &= C_0 T_a (A_d - R_\infty) \\ L_w &= T_a [C_0 R_\infty + \rho_a L_k] + L_p, \end{aligned} \quad (2.12)$$

where L_b is a radiance term which is sensitive to bottom reflectance and L_w is remotely observed radiance over optically deep water.

Equation 2.11 is the general formulation for the retrieval of bathymetry from passive imagery. By assuming constant water optical conditions, atmospheric and water reflectance, Philpot (1989) proposed a linear algorithm with deep water correction as

$$X = \ln(L_d - L_w) = \ln(L_b) - gz, \quad (2.13)$$

where, X is a variable linearly related to water depth, and L_w is estimated from optically deep water pixels (pixels containing only water column reflectance) (Lyzenga *et al.*, 2006; Kanno and Tanaka, 2012).

For uniform water conditions and substrate type, only one spectral band is required in Equation 2.13 to retrieve water depth from remotely sensed data with at least two known water depths. Generally, multi-band imagery is collected and thus a principal component analysis of the received multi/hyperspectral imagery has been proved to yield the optimal result as (Philpot, 1989)

$$Y = \mathbf{a} \cdot \mathbf{X} = \mathbf{a} \cdot \ln(L_b) - (\mathbf{a} \cdot \mathbf{g})z, \quad (2.14)$$

where, \mathbf{a} is the leading eigen vector corresponding to the largest eigenvalue. Philpot (1989) also mathematically shows that this method is insensitive to varying substrate types, but varying water optical conditions impose a non-linearity that degrades the analysis significantly.

Even though the linear formulation has been shown to be effective in various studies, the use of a deep water correction limits its application in shallow water. To accommodate passive bathymetry in shallow river studies, Stumpf *et al.* (2003) and Dierssen *et al.* (2003) employed a simpler band ratio method by selecting a band ratio of bottom reflectance that is approximately constant for all benthic cover types; thus the change of water depth has a more significant effect. The band ratio is described as

$$\ln\left[\frac{L_{d1} - L_{w1}}{L_{d2} - L_{w2}}\right] = \ln\left[\frac{L_{b1}}{L_{b2}}\right] - [g_1 - g_2]z. \quad (2.15)$$

The band ratio method here is a special case of the linear algorithm (see Equation 2.14) with $\mathbf{a} = (1, -1)$. Legleiter *et al.* (2009) neglected the water column reflectance term for shallow water (the first term in Equation 2.9 is negligible with small z) and then employed an optimized band ratio analysis to find an optimal band pair which yields the highest regression R^2 . This method has been applied to retrieve water depth from multi/hyperspectral imagery for shallow fluvial environments (Legleiter, 2015); however, there are still some limitations. First, only two bands are used to retrieve water depth while all other bands are neglected; this differs from the linear algorithm that utilizes all available bands. Second, the consideration of non-zero L_W has the potential to improve estimation, particularly for turbid water environments.

Maximum detectable depth

To derive the general expression for maximum detectable water depth for hyperspectral imagery, it is essential to understand the underlying spectral physics related to bathymetry retrieval. The maximum detectable water depth is defined as the depth at which the difference between the observed reflectance and deep water reflectance is at a minimum, which can also be described as the imaging spectral resolution. The derivation of maximum detectable water depth for hyperspectral imagery, and the subsequent accuracy analysis in

this dissertation are for the ideal situation, therefore the presence of noise is not considered in the simulation. Also note that the derivation presented is a summary of the work done by Philpot (1989) and Legleiter *et al.* (2004), and therefore more details are available in these studies. To acquire the estimation of the maximum detectable depth, Equation 2.9 is revised as

$$d_{max} = \frac{\ln(dR) - \ln(R)}{-g}, \quad (2.16)$$

where $dR = R(0^-) - R_\infty$ and $R = A_d - R_\infty$. Therefore, the maximum detectable depth is defined with respect to dR , the resolution of the imaging system in terms of reflectance; and R is the reflectance contrast between the benthic layer and deep water reflectance. The simulated maximum detectable depth is given in Figure 2.1 for different sensor sensitivity, benthic contrast and effective attenuation coefficient g .

The maximum detectable depth decreases significantly with an increase of water attenuation. In addition to the water attenuation coefficient, the decrease of sensor sensitivity and decrease of benthic contrast both impose extra degradation on maximum detectable water depth. The sensor sensitivity is dependent on the specific sensor used in the hyperspectral imaging system. Typically, a 12 bit sensor is more sensitive than an 8 bit sensor; however, the more sensitive sensor also theoretically includes more reflectance noise, which is not modeled in Equation 2.16 and Figure 2.1. A priori knowledge of the estimated water attenuation is thus helpful to determine the effectiveness of hyperspectral imagery for depth determination at a specific surveying site.

Water depth uncertainty

Hyperspectral imaging systems digitize the recorded radiance as a Digital Number (DN) and usually a fixed digitizing resolution is associated with a specific system. The

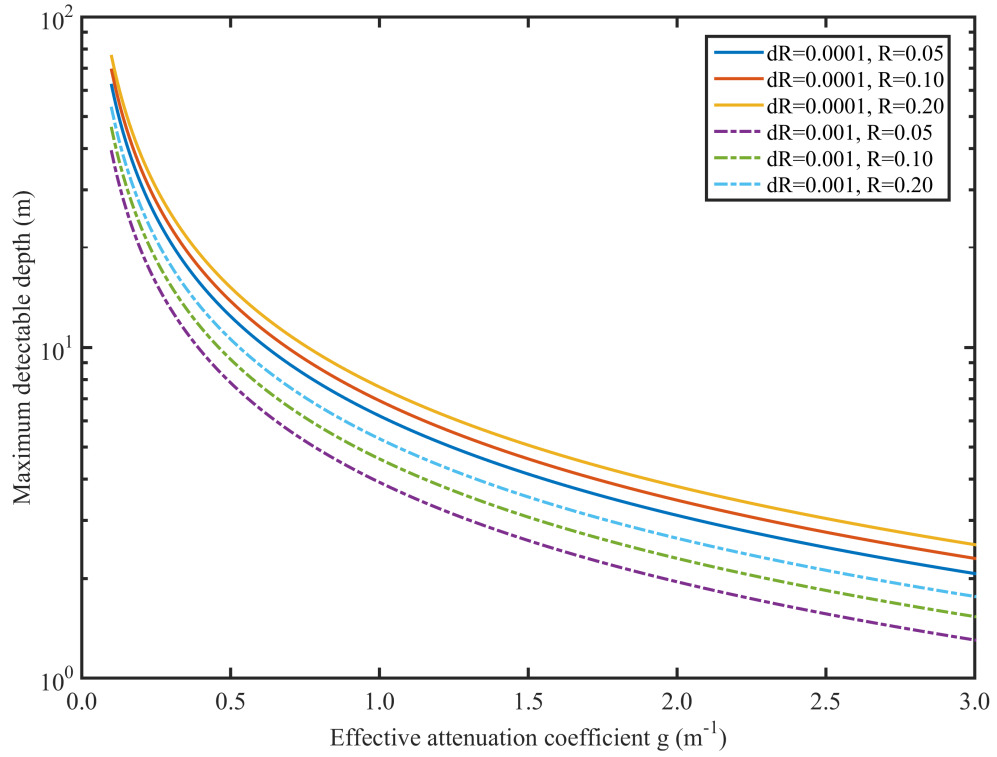


Figure 2.1 Theoretical prediction of the maximum detectable water depth for hyperspectral imagery with varying effective attenuation coefficients.

digital number recorded by the hyperspectral imaging system thus indicates that the derived water depth has a quantization interval that generally results in an uncertainty for the derived water depth. To quantify the depth uncertainty, the derivative of received water reflectance is used, and given as

$$\Delta d = \frac{dR}{-gR \exp(-gd)}. \quad (2.17)$$

Equation 2.17 shows that the uncertainty is directly proportional to sensor sensitivity (dR), therefore, the uncertainty analysis presented in this chapter only includes the influence of benthic contrast and water attenuation. Figure 2.2 shows the depth uncertainty in the observed reflectance with varying benthic contrast, water attenuation coefficients and

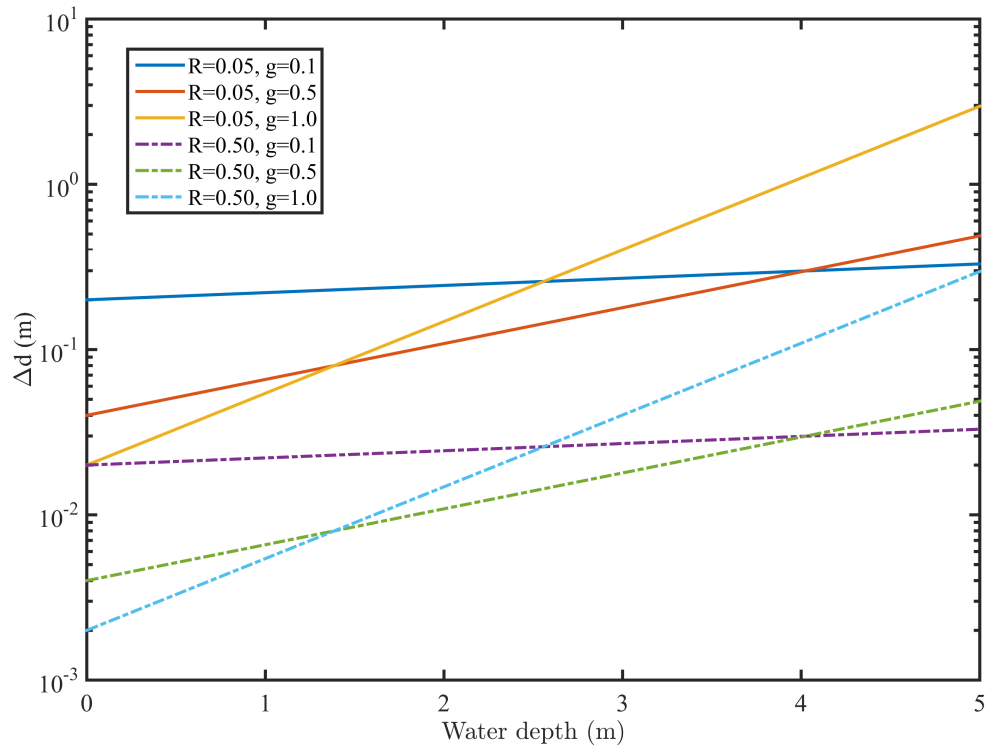


Figure 2.2 Theoretical prediction of water depth uncertainty for hyperspectral imagery depth retrieval, $dR=0.001$.

water depth. Depth uncertainty for clear water (for example, $g = 0.1$) increases slower with water depth than more turbid water, however, it is noted that in very shallow water, clear water has a larger depth uncertainty than more turbid water. The physical reason for this is that more depth change is needed to produce a significant enough drop in observed reflectance at the hyperspectral imaging detector. Also, an increase in benthic contrast improves the depth uncertainty significantly. Comparing depth uncertainty to the maximum detectable water depth, we conclude that turbid water significantly reduces the maximum detectable water depth but that depth uncertainty improves for shallow turbid water. The combination of maximum detectable depth and depth uncertainty illustrates the complexity of applying hyperspectral imagery to bathymetry retrieval.

Water depth accuracy

In addition to water depth uncertainty, it is also desirable to investigate water depth accuracy in terms of different benthic contrast, water attenuation and water depth. The water depth accuracy is given as the ratio of the depth uncertainty to the actual water depth and therefore Equation 2.2 is revised as

$$\frac{\Delta d}{d} = \frac{dR}{-gR \exp(-gd)d}. \quad (2.18)$$

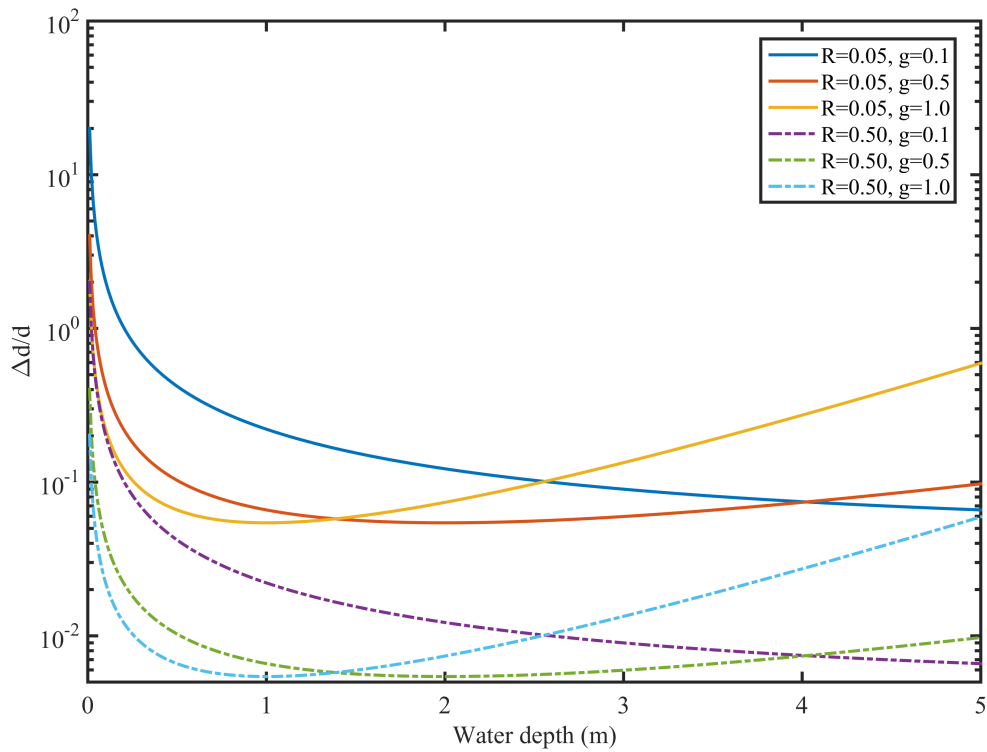


Figure 2.3 Theoretical prediction of water depth accuracy for hyperspectral imagery, $dR=0.001$.

Figure 2.3 shows the derived water depth accuracy, which improves as the water gets deeper for clear water ($g = 0.1$). However, for more turbid water, water depth accuracy

improves for shallow water (<1 m) and degrades significantly as the water gets deeper. Similar to water depth uncertainty, clear shallow water has a less accurate derived water depth than more turbid shallow water.

The complexity of derived water depth accuracy denotes a significant limitation of hyperspectral imagery for water bathymetry retrieval because the accuracy is dependent not only on the instrument but also on the specific survey site. A tool which provides a surveying accuracy solely based on the instrument specifications and invariant to the observational environment is thus desirable for more efficient bathymetry retrieval. Airborne bathymetric LiDAR turns out to fit these specific requirements.

2.2.3 Radiative Transfer for Airborne Bathymetric LiDAR

In contrast to passive water remote sensing, active airborne bathymetric LiDAR emits green laser pulses to penetrate the water surface and detect the benthic layer. Instead of measuring reflected radiance, the time difference between the emitted laser pulse and the reflected laser energy is used to determine the water depth. This section provides a simplified radiative transfer model for bathymetric LiDAR for the purpose of subsequent radiometric analysis. We begin with Wagner *et al.* (2006), who defines the returned pulse energy as a convolution of the target cross-section and the emitted LiDAR pulses. This formulation was modified in Cossio *et al.* (2009) to give the LiDAR pulse return energy in terms of photo-electrons, which is interchangeable with pulse energy, thus giving a more relevant formulation for investigating radiative transfer. For topographic targets, assuming an isotropic reflecting surface, the LiDAR link equation can be used to describe the return pulse energy as

$$E_r = \eta_r E_t \rho_\lambda \cos(\alpha) \frac{A_r}{\pi R^2} (\exp(-\beta_{e,\lambda} R))^2, \quad (2.19)$$

where E_r is the received laser energy at the remote detector; which is normally either an avalanche photodiode (APD) or photomultiplier tubes (PMT) (Guenther *et al.*, 1996; Guenther, 2006; Tuell *et al.*, 2010). η_r is the receiver net efficiency, that quantifies the energy received at the remote detector, which may also include the receiver optical and detector quantum efficiency depending on the specific LiDAR system. E_t is the transmitted laser pulse energy, ρ_λ is the target spectral reflectance, α is the laser incidence angle, A_r is the receiver aperture area, R is the range between the detector and target, and $\beta_{e,\lambda}$ is the atmospheric extinction coefficient describing laser transmittance. For multiple targets along the laser path, the incident laser pulse energy (E_t) varies with the portion received at each target without a priori knowledge, which results in difficulty calibrating the return intensity for physical reflectance when multiple targets are present (Wagner *et al.*, 2006).

For most high signal-to-noise ratio (SNR) LiDAR systems currently employed, background noise has a negligible effect on the final received laser signal. However, noise modeling is critical for more recent systems that employ low SNR single photon detection, e.g. (Cossio *et al.*, 2009). The bathymetric LiDAR used in this dissertation has a relatively high laser energy, thus the noise modeling is neglected to simplify the radiative transfer model. However, to adapt Equation 2.19 to bathymetric LiDAR, additional water surface, column and benthic return contributions must be considered.

Equation 2.19 describes the Lambertian propagation of laser pulses, which is applied in topographic LiDAR because the wavelength used is always much smaller than the size of the scattering targets. However for bathymetry, specular reflection from the water surface is a significant contribution to the laser pulse return. The wave structure of a surface can strengthen the specular glint if it aligns with the laser propagation direction. An effective Lambertian reflectance ($r_{\text{int}}(\alpha_s)$, α_s is the incidence angle) for the water surface is generally used to replace the reflectance term in Equation 2.19 to determine the water surface return (Cossio *et al.*, 2009; Degnan and Field, 2014). However, specular water surface returns

are in general not desired for bathymetric LiDAR returns, and thus some LiDAR systems employ a circular or elliptical scanning pattern, at a constant angle of incidence to the mean water surface to reduce water surface specular reflections (Rie; Tuell *et al.*, 2010).

In addition to the specular water surface return, echoes from the water column also disturb bathymetry determination. As the laser light propagates through the water column, absorption and scattering occur that cause energy loss observed at the detector. The laser beam attenuation is described by Beer's Law (Cossio *et al.*, 2009) as

$$E(R_W) = E_0 - \exp(-c_\lambda R_W), \quad (2.20)$$

where, $E(R_W)$ is the laser energy at distance R_W , E_0 is the amount of energy refracted into the water column, and c_λ is the beam attenuation coefficient which is dependent on water conditions and related to water absorption and backscattering characteristics. By considering both water surface reflection and laser propagation in the water column, the laser return energy arriving at the remote detector from the water column is described by the following equation

$$E_{column} = \eta_r E_i \beta_\lambda(\pi) \Omega_r \left(\frac{1 - \exp(-2c_\lambda R_w)}{2c_\lambda} \right) (1 - r_{int}(\alpha_s))^2 (\exp(-2\beta_{e,\lambda} R)), \quad (2.21)$$

where β_λ is the volume scattering function, $\beta_\lambda(\pi)$ accounts for the backscattered laser pulse energy which enters the remote detector, and Ω_r is the field of view of the detector.

The return laser pulse from the benthic layer is the foundation for determining water bathymetry. The benthic return energy is dependent upon the processes described by Equation 2.19 and 2.21 and the benthic targets characteristics. Based on the previous water

surface and column return derivations, the benthic return can be expressed as

$$E_{bottom} = \eta_r E_t \rho_\lambda \cos(\alpha) \frac{A_r}{\pi(R + R_w)^2} (1 - r_{int}(\alpha_s))^2 (\exp(-2\beta_{e,\lambda} R)) (\exp(-2c_\lambda R_w)), \quad (2.22)$$

The received laser pulse at the remote detector is the sum of water surface, column and benthic returns in terms of energy. In addition to the energy, the temporal shape of the returned laser pulse is also recorded; this is often referred to as full waveform digitization. The received full waveform is a time-series signal that records the backscatter of the laser pulse. Thus the full waveform theoretically contains both the geometric and spectral information describing the water surface, water column and benthic layer simultaneously. The received full waveform is a composite of water surface, water column and benthic returns which is mathematically given as

$$S_T(t) = S_S(t) + S_C(t) + S_B(t), \quad (2.23)$$

where, $S_T(t)$ is the total laser return recorded by the remote detector, $S_S(t)$ is the water surface return, $S_C(t)$ is the water column return, and $S_B(t)$ is the benthic return. Full waveform processing algorithms generally detect water surface and benthic returns to determine the corresponding water depths. The water surface and benthic returns are normally described using a convolution of the incident laser pulse with target impulse response functions by assuming an effective Lambertian water surface reflectance model (Cossio *et al.*, 2009; Wagner *et al.*, 2006).

Wagner *et al.* (2006) gives a detailed derivation of the LiDAR cross-section of return surfaces, and also shows the Gaussian characteristics of laser returns. Equation 2.22 indicates that the water bottom is assumed to be a Lambertian surface, while the water surface can also be treated as Lambertian if we apply an effective Lambertian reflectance (Cossio

et al., 2009). Therefore these two components can be modeled as the convolution of the system response with outgoing Gaussian laser pulses. The water column, however, is a convolution of both water column attenuation and incident laser pulse scattering, assuming a single scatter. The water column return energy is thus determined by Equation 2.20 and the temporal shape of this energy (full waveform) is modeled as

$$S_C(t) = S_{0-}(t) * \exp(-c_\lambda Ct), \quad (2.24)$$

where $S_{0-}(t)$ is the laser pulse time-series signal refracted into the water column, and C is the constant light speed in water.

Equation 2.23 and Equation 2.24 schematically describe the temporal components of the returned bathymetric full waveform and show that the received full waveform contains both location and radiometric information. Water depth is determined by the time difference between the water surface return and the benthic return. A measure of benthic reflectance is also provided by the returned benthic intensity. The intensity is not readily used due to the unknown water attenuation, however, the intensity as well as the full waveform are negligibly affected by the changing illumination conditions. The incidence angle, benthic layer type, and water column characteristics are more influential factors for the intensity.

Maximum detectable depth

In contrast to passive hyperspectral imagery, airborne bathymetric LiDAR retrieves water depth through the time difference between the water surface and benthic returns. Generally, the maximum detectable depth can be simply described by the minimum amount of energy required to trigger a successful pulse in the remote detector if we assume that a water surface return is always available. However, we must also note that bathymetric LiDAR generally detects the return time-series intensity, and thus the stretching effects of

sloped targets, off-nadir incidence angles and water scattering can all affect the derived water bathymetry. The maximum detectable depth of a bathymetric LiDAR system is complicated to predict as it is dependent on the pulse energy and the specific water surface, column and bottom geometric conditions (Abdallah *et al.*, 2012; Bouhdaoui *et al.*, 2014; Abady *et al.*, 2014). To simplify the analysis and nominally predict the maximum detectable depth for a specific bathymetric LiDAR system, we consider only the radiometric energy transfer in the water column. In this case, Equation 2.22 gives the amount of energy received at the remote detector and can be transformed as

$$\frac{E_{\text{bottom}}\pi}{\eta_r E_t A_r [1 - r_{\text{int}}]^2 \cos(\alpha)} = \frac{\rho_\lambda \exp(-2\beta_{e,\lambda} R - 2c_\lambda R_w)}{(R + R_w)^2}, \quad (2.25)$$

here, the water surface reflectance r_{int} is determined by the Fresnel equation and it varies slightly for a narrow scan angle system ($<25^\circ$) (Hecht, 2002), thus it is treated as constant. The incidence angle, α , is determined by both the incident laser pulse and the benthic topography which require prior knowledge, and thus it is not considered but set as zero to generalize the empirical model. The maximum detectable depth is defined as the benthic return laser pulse energy at the minimum detection threshold of the LiDAR detector, and thus the left side of equation is treated as a constant. As for the right side of the equation, due to the fact that $R \gg R_w$ and $c_\lambda R_w \gg \beta_{e,\lambda} R$, and to simplify the equation, all the negligible terms are canceled out, and the relationship can be approximated as

$$z = R_w = \frac{\ln\left(\frac{\kappa R^2}{\rho_\lambda}\right)}{-2c_\lambda}, \quad (2.26)$$

here, κ is the constant term for the left side of Equation 2.25. However, it is difficult to acquire the specific parameters to calculate κ . To generalize the relative determination of the maximum detectable water depth, we assume the maximum detectable water depth of a particular LiDAR is 10 m ($\rho_\lambda = 0.3, c_\lambda = 0.15$), which is based on commercial specifications

of current high-resolution bathymetric LiDAR systems from Riegl VQ820-G and Optech Aquarius bathymetric LiDAR system (Rie; Aqu). The constant term κ is then calculated and used to predict the maximum detectable depth with varying parameters.

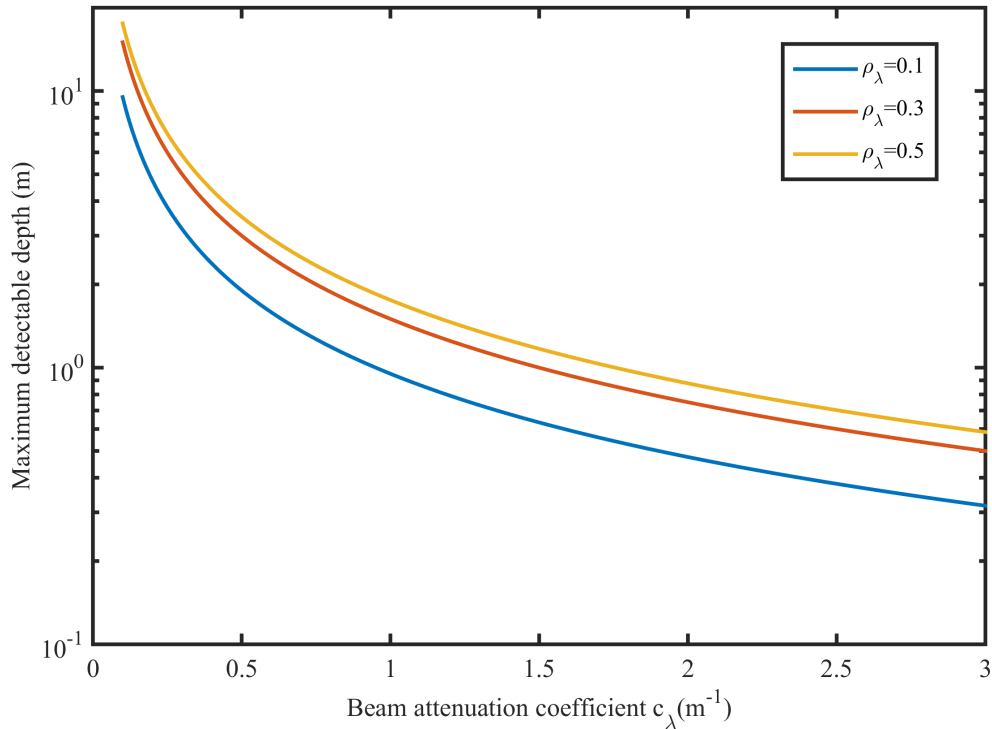


Figure 2.4 Theoretical prediction of the maximum detectable water depth for bathymetric LiDAR with varying water attenuation coefficients. Different curves represent differing benthic layer reflectance.

Figure 2.4 shows the maximum detectable water depth derived using the semi-analytic method presented. The maximum detectable water depth significantly decreases as the beam attenuation increases, which implies that water clarity characteristics are the dominant factors influencing bathymetric LiDAR performance. Even though the maximum detectable depth model (Equation 2.26) assumes a known maximum depth for a given water attenuation coefficient it can still be generalized to real LiDAR systems with a calibration of a measured water attenuation coefficient and an observed maximum water depth. However, as the approximation ignores lesser terms, such as the stretching effect of the water

column on the incident laser pulses and the field of view loss of energy, the maximum detectable depths is optimistically estimated in Figure 2.4.

Minimum detectable water depth and accuracy

As bathymetric LiDAR systems determine water depths through a time difference between the water surface and benthic returns, a specific pulse width LiDAR system has a minimum detectable water depth which is generally not determined by the radiative transfer of laser pulse in the water column, but by the resolution of the laser pulse. The range z calculated by a LiDAR system is given as

$$z = \frac{Ct}{2}, \quad (2.27)$$

where C is the light speed in the water column (nominally constant), and t is the measured time difference of returns. Therefore, the nominal minimum detectable depth is determined by the capability of the LiDAR system to discriminate different returns. As an example, the bathymetric LiDAR system, Aquarius, used in the subsequent analyses, has a pulse width of 8.3 ns, which generally yields a minimum detectable water depth of 0.47 m if we assume the system cannot discriminate two distinct returns within one full width at half maximum (FWHM) (Legleiter *et al.*, 2015). However, this estimated minimum detectable water depth does not include consideration of water column scattering and therefore it is also optimistically estimated.

The retrieved water depth accuracy is also dependent on the timing resolution of the specific system and the positional errors introduced by the GNSS/INS systems on board (Glennie, 2007). To estimate a nominal depth accuracy with respect to time, the derivative

of Equation 2.27 is used and given as

$$\Delta z = \frac{C}{2} \Delta t. \quad (2.28)$$

Considering a LiDAR system with a minimum of 1 ns timing resolution, which corresponds to current waveform sampling intervals; the corresponding depth accuracy is approximately 11 cm. A more comprehensive analysis of total propagated uncertainty (TPU) is necessary to determine the depth accuracy (Habib *et al.*, 2009), however, most GNSS/INS errors remain essentially constant for a small area, and thus the water depth error is dominated by the LiDAR system but invariant to the water column conditions. This is a strong advantage compared to passive imagery which exhibits varying depth accuracy for specific survey sites and for various instruments.

Chapter 3

Study Sites and Datasets

Several study areas were selected to examine the algorithms proposed in this dissertation, including two distinct fluvial rivers, the Snake River located in Wyoming and the Blue/Colorado River confluence located near Kremmling, Colorado, and East Pass located in Destin, Florida. All sites had airborne hyperspectral imagery and full waveform bathymetric LiDAR data collected. The two fluvial rivers were collected with an Optech Aquarius bathymetric LiDAR system and East Pass was collected with the newly developed three wavelength Optech Titan system. Airborne hyperspectral imagery data were collected with varying spatial and spectral resolutions using a CASI-1500 with details given within this chapter. Various *in situ* field observations were also collected for each site for the purpose of validating the airborne remote sensing datasets.

3.1 Study Area Description

3.1.1 Rusty Bend of the Snake River

The Snake River is a major river in the Pacific Northwest of the United States and originates in western Wyoming. A portion of the river in Wyoming's Grand Teton National Park was selected as the study site (see Figure 3.1(a)). Water flow in this section of the river is regulated by the Jackson Lake Dam. Coarse bed material and large woody debris delivered from the nearby tributaries produce a complex, wandering morphology that is prone to frequent channel change. Clear water is present for the Snake River after snowmelt runoff recedes, ideal conditions for remote sensing. The study site is focused on a sinuous, single trend channel which is referred to as Rusty Bend that consists of a gravel bar along the inner bank and a deep pool along the outer bank where the river has eroded into a terrace.

The river's bed material consists primarily of gravel and cobble, coated with varying degrees of periphyton and bright green filamentous algae. Field spectra from the Snake River and other gravel bed streams indicate that where these photosynthetic organisms occur, absorption by chlorophyll produces a pronounced decrease in reflectance at 675 nm. At the base of the high, nearly vertical outer bank, blocks of exposed clay bedrock create areas of higher bottom reflectance, visible as bright patches. Although these heterogeneous substrates might complicate remote mapping to some degree, the simple morphology of Rusty Bend, with shallow depths over the point bar gradually increasing to a maximum of 2.82 m along the outer bank, facilitates interpretation of the airborne hyperspectral imagery and bathymetric LiDAR capabilities.

3.1.2 Confluence of the Blue and Colorado River

The confluence of the Blue and Colorado Rivers represents a more complicated fluvial environment, optically as well as morphologically (see Figure 3.1(b)). The Colorado River originates in Rocky Mountain National Park and flows west past the town of Kremmling, where the Blue River enters from the south. The confluence occurs at the base of remnant Tertiary basin fill that stands above a low relief floodplain; dense riparian vegetation occurs along the banks. Gradients for both rivers are lower than for the Snake and bed material consists of sand and fine sediment; lesser amounts of gravel are exposed where the Blue curves to the west just upstream of the confluence. In addition to this inorganic material, portions of the streambed host abundant, dense aquatic vegetation. These plants are particularly thick along the outer bank of the sharp bend in the Blue, where the "canopy" extends through the water column to the surface. A major contributor to water variability is the mixing of waters with different optical characteristics. In addition to the Blue, another, smaller tributary aptly named Muddy Creek enters the Colorado River from the north. Surface erosion triggered by rainfall in the days preceding the data acquisition delivered fine-grained sediment to Muddy Creek and created a plume of more turbid water extending downstream

along the right bank of the Colorado River below the confluence. Water from the Blue River is also distinct in this representation, with darker Colorado River water visible between the inputs from the two tributaries. The convergence of three rivers with contrasting optical characteristics at this site thus provided a unique opportunity to assess how water clarity might influence bathymetric mapping performance of the two remote sensing systems.

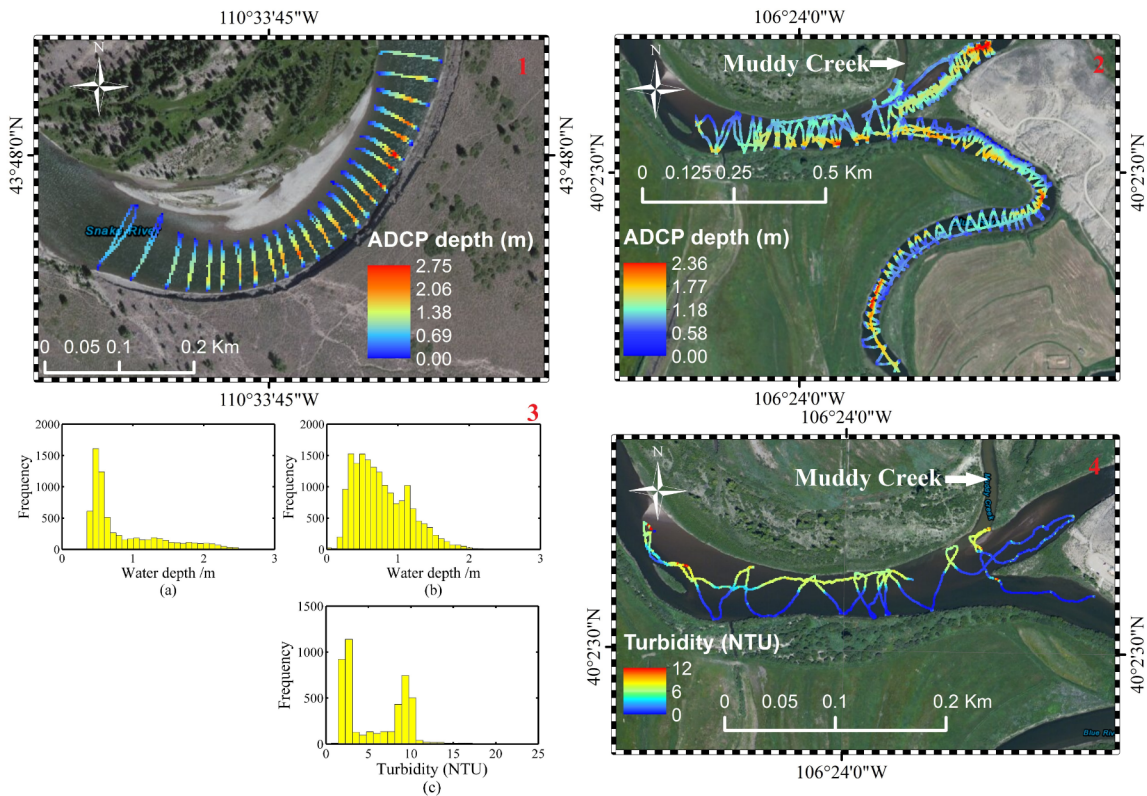


Figure 3.1 (1) ADCP measurements for the Snake River, (2) ADCP measurements for the Blue/Colorado River (3) (a) Snake River; (b) Blue/Colorado River; (c) Blue/Colorado River, (4) turbidity measurements for the Blue/Colorado River.

3.1.3 East Pass of Destin

One coastal area was also selected for study within the East Pass near Destin, Florida, USA (see Figure 3.2). The East Pass connects the Choctawhatchee bay with the Gulf of Mexico and it was a micro tidal inlet during the airborne data collection. The water depth for the East Pass varies from shallow to deep water (>10 m). Emerald green water and white beaches prevail near East Pass and the benthic sand dunes in the shallow water can be

clearly observed from both airborne and satellite imagery. The East Pass is protected from the sifting sands of the Gulf of Mexico by twin channel jetties, which were constructed by the U.S. Army Corps of Engineers. The East Pass channel is regularly dredged to maintain the mean channel depth. The benthic bathymetry and the presence of clear water make it an ideal place to investigate the performance of the airborne sensors.

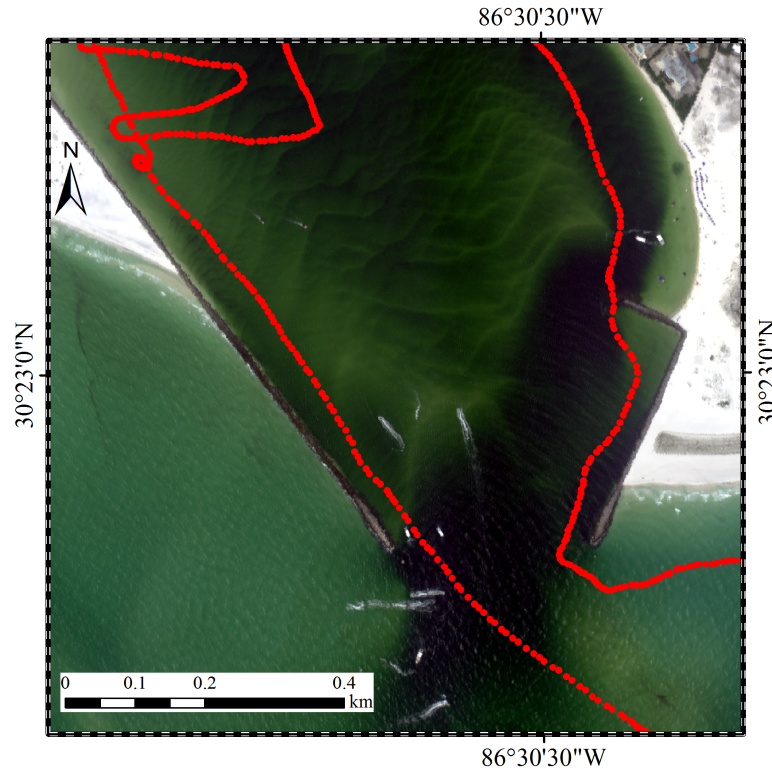


Figure 3.2 The East Pass of Destin, Red points show the locations of ADCP samples.

3.2 Airborne Hyperspectral Imagery Datasets

Hyperspectral imagery was collected with an ITRES Compact Airborne Spectrographic Imager (CASI)-1500 sensor (see Figure 3.3). CASI-1500 is a pushbroom camera with 1500 across-track pixels spanning a 40° field of view and has a programmable spectral range that extends from 380 to 1050 nm with a maximum of 288 bands. The spatial resolution is dependent on the flight altitude, camera frame rate and the aircraft speed and it can be as high as 25 cm. The CASI-1500 has been fully calibrated by the manufacturer and provides

data in spectral radiance. The recorded data is digitized with 14 bits with a noise floor of less than 2 digital numbers (DN). The CASI image data were directly georeferenced using trajectory information from the GPS and inertial navigation system (INS) on board the aircraft. A Digital Elevation Model created from airborne LiDAR is provided for the orthorectification. The principal parameters for the two fluvial rivers and the East Pass are reported in the Table 3.1.



CASI-1500 Sensor Head, 47 H x 47 W 54 D (cm) 25Kg

Figure 3.3 Itres hyperspectral imaging system - CASI-1500 (courtesy of Itres).

Table 3.1 Summary of principal airborne remote sensing datasets parameters for the study areas.

	Snake River		Blue/Colorado River		East Pass	
	LiDAR(532,1064nm)	Optical	LiDAR(532,1064nm)	Optical	LiDAR(532,1064,1550 nm)	Optical
Pulse width (ns)	8.3,12	N/A	8.3,12	N/A	2.5, 2.5, 2.5	N/A
Field of view (°)	40,46	40	40,46	40	30, 30, 30	N/A
Beam divergence (mrad)	1,0.8	N/A	1,0.8	N/A	0.70, 0.35, 0.35	N/A
Pulse rate (kHz)	33,100	N/A	33,100	N/A	100, 100, 100	N/A
Flight height (m)	510,580	580	580,2600	2600	300 to 500	2200
Point density (pts/m ²)	4.2,6.3	N/A	4.0,2.5	N/A	4.0 ,4.0 ,4.0	N/A
Number of bands	N/A	22	N/A	64	N/A	48
Pixel size (m)	N/A	0.6	N/A	1.2	N/A	1.0

* For the Snake River and the Blue/Colorado River, the NIR LiDAR was collected with a separate Optech Gemini sensor.

* The Optech Titan was used to collect both the green and two NIR wavelengths LiDAR returns for the East Pass.

* The nominal flight height was varying for the East Pass to test the bathymetric LiDAR penetration capability.

Atmospheric correction

CASI-1500 registers the recorded digital number to solar radiance ($\mu W/(cm^2 * sr * nm)$) with radiometric calibration provided in the manufacturer software. Even though radiance is physically meaningful, spectral reflectance is more practical for hyperspectral imagery to accommodate comparisons of imagery with different collection times and sensor types. To obtain spectral reflectance, we applied a Fast Line-of-Sight Atmospheric Analysis of Hypercubes (FLAASH) correction (Cooley *et al.*, 2002), implemented in the ENVI (Environment for Visualizing Images) software package to calibrate the hyperspectral imagery to spectral reflectance. The additional information required to apply FLAASH includes the scene geographical location, sensor type and altitude, ground elevation and pixel size, flight date and time, visibility estimation (40 km for this study), standard atmospheric and aerosol models from the Modtran 4 radiative transfer model (Cooley *et al.*, 2002), and a water vapor absorption feature wavelength. A more sophisticated approach, contained in the Atcor4 (ReS) software package can also correct for topographic effects with an input of a DEM, but FLAASH is adequate for the spatially small ($1 km^2$) scenes which contain a relatively flat water surface and negligible topographic variation. The two fluvial rivers were atmospherically corrected with Atcor4 software due to the significant topographic change present and the DEM was created from the near-infrared LiDAR point cloud. The East Pass was atmospherically corrected using the FLAASH software.

The other required pre-processing tasks for the hyperspectral imagery are to define a water mask and to apply a spatial filter (Legleiter *et al.*, 2015). The water mask was created based on the Normalized Difference Vegetation Index (NDVI). Water pixels generally have negative NDVI due to the excessive absorption of near-infrared radiance (Pan *et al.*, 2016a; Gao *et al.*, 2007). The resultant imagery was filtered with a 3 by 3 Wiener filter to reduce the random noise present (Legleiter *et al.*, 2015).

Sun glint removal

The two river systems were calm and no obvious specular reflection observed, however, for the hyperspectral imagery collected for the East Pass coastal water, specular reflection for waves was obvious and therefore a sun glint removal was performed. Specular reflection over the wavy water surface biased the benthic remote sensing reflectance observed at the detector. The specular reflection results in white pixels that confound the interpretation of passive hyperspectral imagery, especially for airborne high spatial resolution imagery. Generally, the observed hyperspectral spectrum is recovered with the assistance of reflectance observed in the near-infrared spectrum.

The method proposed by Hedley *et al.* (2005) was implemented in this study to reduce sun glint present in the East Pass hyperspectral imagery. This method adjusts the observed hyperspectral imagery with the observed near-infrared reflectance and establishes a correlation between reflectance at each wavelength and near-infrared reflectance. There are two physical reasons to apply this sun glint removal method. First, the amount of reflected solar radiance for the near-infrared band is mostly from sun glint, a spatially constant ambient light and a negligible contribution from the water column and benthic layer. This assumption holds with the fact that water absorbs most of the near-infrared (700 - 1000 nm) light (Mobley, 1994). Second, the near-infrared solar radiance is linearly related to the amount of sun glint in the visible bands. This assumption holds because the water index of refraction is nearly equal for visible and near-infrared bands (Mobley, 1994). According to these two assumptions, the remote sensing reflectance is corrected sun glint removal as

$$R_c = R_o - s(\lambda)(R_{NIR} - Min_{NIR}), \quad (3.1)$$

where R_c is the corrected remote sensing reflectance; R_o is the original observed remote sensing reflectance after atmospheric correction; $s(\lambda)$ is the slope coefficients estimated

from a linear regression of the near-infrared bands and each visible band; R_{NIR} is the observed near-infrared reflectance; Min_{NIR} is either the minimum observed near-infrared reflectance or the ambient near-infrared reflectance. The original and glint corrected RGB image for the East Pass is shown in Figure 3.4.

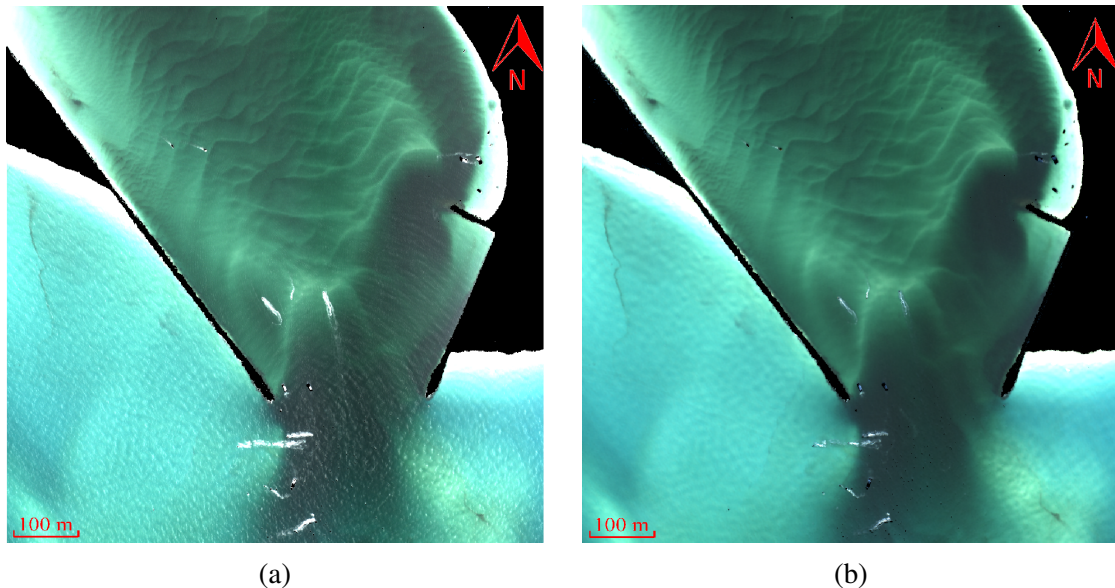


Figure 3.4 (a) RGB (R: 641.63nm, G: 556.14 nm, B: 456.34 nm) imagery before sun glint removal; (b) RGB (R: 641.63nm, G: 556.14 nm, B: 456.34 nm) imagery after the sun glint removal. The land area was masked out of the original imagery.

From a visual inspection, this algorithm removes most of the sun glint in this area and preserves a more consistent deep channel and coastal area. Unfortunately, a quantitative assessment of this sun glint removal algorithm was not implemented due to the absence of field measured water leaving spectra.

3.3 Airborne Bathymetric LiDAR Datasets

The airborne LiDAR datasets for the two fluvial rivers were collected by the National Center for Airborne Laser Mapping (NCALM) with Optech Aquarius and Gemini systems (see Figure 3.5). The Aquarius sensor is a single band LiDAR based on a Q-switched frequency doubled Nd:YAG laser with a resultant wavelength of 532 nm, programmable

pulse repetition frequencies (PRFs) of 33, 50, and 70 kHz, a pulse energy of 30 μJ (at 70 kHz), and a beam divergence of 1 mrad. The scanner is a conventional side-to-side oscillating mirror (saw-tooth pattern) with an adjustable field of view up to $\pm 25^\circ$ and a maximum mirror frequency of 70 Hz. The return signal is both analyzed in real time by a constant fraction discriminator (CFD) and stored using a waveform recorder (see Figure 3.6) with 12 bit amplitude quantization and a sampling speed of 1 GHz. The Gemini system is similar to the Aquarius system with an Nd:YAG laser at 1064 nm, smaller and adjustable divergence angle (0.25 *mrad* or 0.8 *mrad*) and PRF up to 167 kHz. Table 3.1 shows the principal data acquisition parameters for both fluvial project sites.



Figure 3.5 Optech Aquarius bathymetric LiDAR (courtesy of Optech Inc.).

It should be noted in Table 3.1 that there is no NIR data listed for the Blue/Colorado River. NIR was collected for this study, but unfortunately was acquired at a high flight elevation (2,600 m AGL); laser pulses on the water surface were mostly absorbed. Effectively no water surface returns were found and therefore the NIR data for the Blue/Colorado River



Figure 3.6 Optech full waveform digitizer (courtesy of Optech).

was not used. It should also be noted that flights with the Gemini system and Aquarius system cannot be performed at the same time. The NIR LiDAR and the hyperspectral imagery data were collected simultaneously on Aug 21st, 2012 for the Snake River and Sept 6th, 2012 for the Blue/Colorado River. The green LiDAR was collected separately on Aug 26th, 2012 for the Snake River and Sept 5th, 2012 for the Blue/Colorado River.

Both the airborne LiDAR bathymetry and hyperspectral imagery for the East Pass were taken on August 20th, 2015 with sunny skies present. The airborne LiDAR bathymetry was collected with the Optech Titan multiwavelength LiDAR system which utilizes three wavelengths lasers simultaneously (532 nm, 1064 nm and 1550 nm). Each laser beam has up to 300 *kHz* effective pulse repetition frequency (PRF) for a combined PRF of 900 *kHz*. The green laser light, 532 nm, physically has the capability to penetrate the water surface and detect shallow water bathymetry. The simultaneous collection of near-infrared laser pulses enables a more accurate water surface detection (Pan *et al.*, 2015b). Each laser beam has the capability to record full waveform returns with a separate waveform digitizer. The two near-infrared wavelength channels have 0.35 *mrad* beam divergence while

the green channel has a 0.70 *mrad* beam divergence. The high PRF of the Optech Titan multiwavelength LiDAR system enables dense point cloud collection up to 45 points/ m^2 . The point cloud for near-infrared and green channels were classified to define the benthic layer and water surface respectively using the method described in Axelsson (2000) and implemented in the Terrascan software package. A refraction correction was applied to the green channel benthic layer returns to account for refraction at the air water interface to improve the accuracy of the final bathymetry product.

3.4 Acoustic Doppler Current Profiler Data

To assess the ability of full waveform bathymetric LiDAR and hyperspectral imagery for measuring river morphology, in situ ground reference datasets were collected with a Sontek RiverSurveyor S5 Acoustic Doppler Current Profiler (ADCP) (see Figure 3.7) deployed from a kayak. SonTek reports a depth resolution of 0.001 m and an accuracy of 1% over the range of 0.2-15 m. ADCP data is our primary ground reference data, as the accuracy should be better than 3 cm for the two fluvial river sites as most water was shallower than 3 m. The ADCP depth observation locations for both projects are shown in Figure 3.1. The distribution of ADCP water depths for the Snake River (Figure 3.1.3(a)) and Blue/Colorado River (Figure 3.1.3(a)) show that most water depths for the Snake River are less than 2 m while most water depths for the Blue/Colorado River are less than 1.5 m. ADCP measurements were collected from Aug 14th to Aug 22nd, 2012 for the Snake River; all data (including both ADCP and water turbidity data) were collected on Sept 4th and Sept 5th, 2012 for the Blue/Colorado River. A real time kinematic (RTK) GPS base station was co-located with the ADCP and the measurements were cross-calibrated with a separate wading RTK GPS survey. An adjustment was made to account for the depth of the ADCP probe beneath the water surface, the position of the ADCP on the kayak and any datum offset for the ADCP measurements. To estimate the influence of temporal gaps

between the field and airborne data collections, water discharge rates provided by the U.S. Geological Survey (USGS) stream gauges for both rivers over the field collection campaign dates were used. The actual gauge water surface height data is only available for the most recent collection. However, the USGS gauging station at the downstream edge of the flight area shows that there was a roughly 100 cfs (cubic feet per second) change in flow rate between August 23rd and August 26th (see Figure 3.8), 2012, which results in approximately a 1.5 cm change in water surface elevation. There was a discharge change of 60 cfs (see Figure 3.9) between September 4th and 5th for the Blue/Colorado River, which is approximately a 3 cm water surface elevation change.

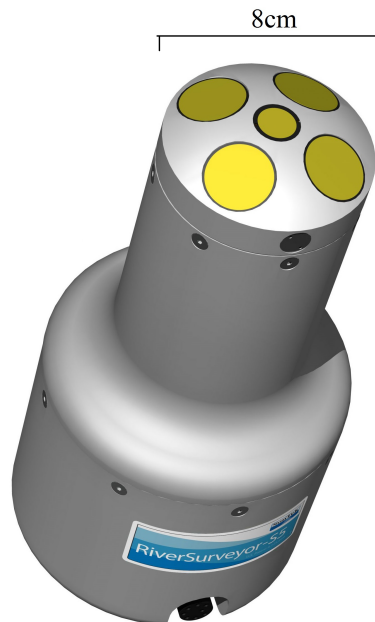


Figure 3.7 Sontek RiverSurveyor S5; 5 transducers measure the water depth at different angles. Only the measurements produced by the center transducer were used to derive water depth for each site.

For the East Pass survey site, a SonTek RiverCAT system with an Acoustic Doppler Profiler was also used to collect the field measured water depths deployed from a pontoon boat. The RiverCAT system has three transducers and measures water depth for every 5 seconds. A real-time GPS antenna was co-located with the RiverCAT system for registering water depths to a geographical coordinate frame. SonTek reports a depth resolution of

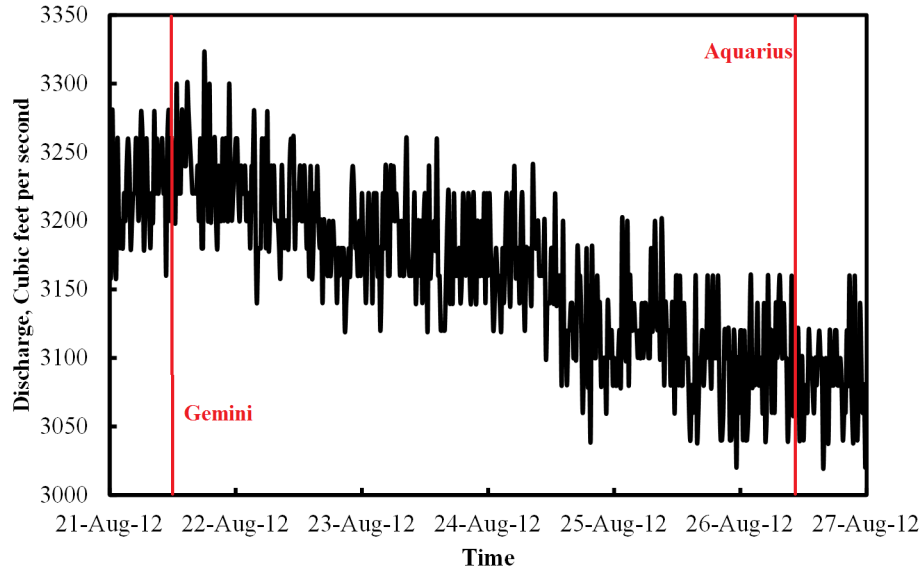


Figure 3.8 Discharge rate at USGS gauge station 13013650, on the Snake River at Moose, WY.

0.001 m and an optimistic accuracy of 1% over the range of 0.2 to 15 m. The ADP data was collected at the same time as the airborne missions and the tidal difference between the datasets is therefore negligible. The 423 ADP samples located in the study area are shown in Figure 3.2. Because white sand prevails in this area, field measured white sand spectra were also collected with an ASD FieldSpec4 spectroradiometer which is shown in Figure 3.11 for determination of the benthic normalized albedo.

3.5 Water Turbidity Data

Water attenuation is a sum of absorption (a) and scattering (b), and the backscattering (b_b) can be represented by the scattering that is composed of the scattered radiation redirected toward to the optical detector (Legleiter *et al.*, 2015). In this study, a WET Labs EcoTriplet (see Figure 3.12) was deployed from a kayak on the Blue/Colorado River to measure the portion of the total back-scattering ($b_b(700\text{nm})$) associated with particulates (i.e., suspended sediment and organic material) in the water column. Turbidity, a common metric of water clarity, is derived from the measured backscatter. Figure 3.1.4 shows the

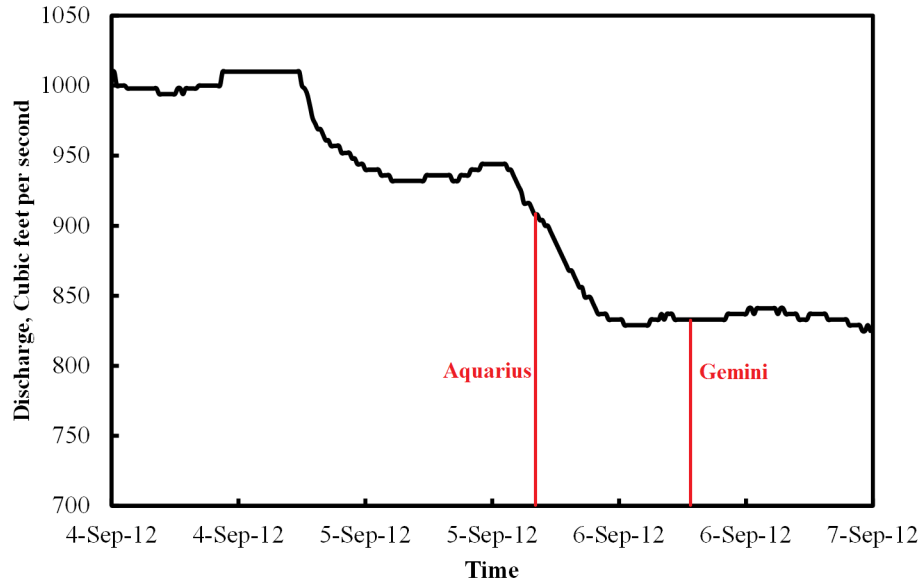


Figure 3.9 Discharge of USGS gauge station 09058000 on the Colorado River near Kremmling, CO.

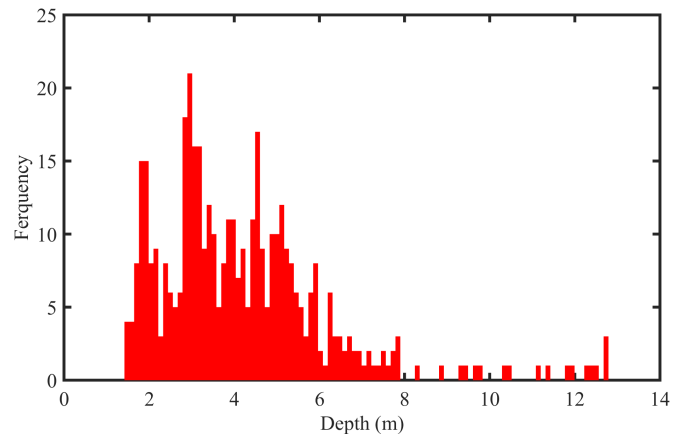


Figure 3.10 The histogram of ADCP measured water depths for the East Pass.

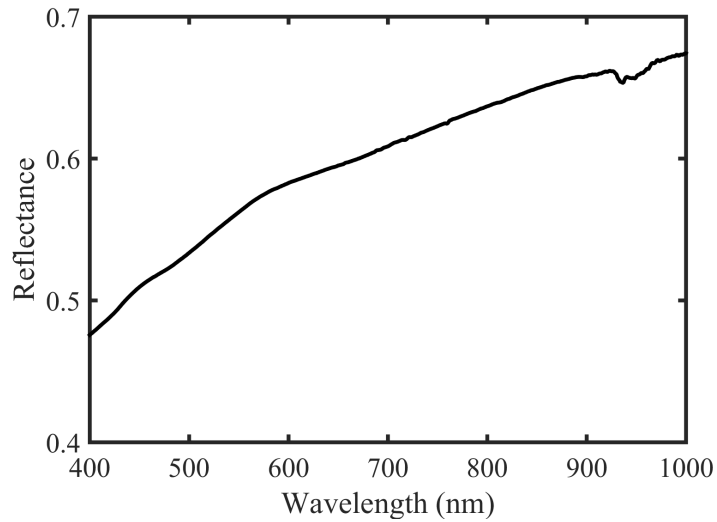


Figure 3.11 White sand field spectrum measured with ASD FieldSpectra4.

spatial distribution of turbidity measurements across the Blue/Colorado confluence with distinct levels of water clarity. The northern part of the river is distinctly more turbid than the southern portion of the river. Note that turbidity measurements and ADCP measurements were collected on separate deployments of the kayak. Figure 3.1.3(c) shows the bimodal distribution of the turbidity measurements.



Figure 3.12 WET Labs EcoTriplet.

Chapter 4

Performance Assessment of High Resolution Airborne Full Waveform LiDAR for Shallow River Bathymetry

4.1 Overview

Full waveform LiDAR (FWL) records the full backscatter for each laser pulse and therefore it contains both geometric and radiometric information (Allouis *et al.*, 2010). Full waveform LiDAR has received considerable attention for topographic applications. Recently, the analysis of FWL processing has focused on evaluating different waveform decomposition methods in parallel to find superior algorithms for specific applications. For example, Wu *et al.* (2011) compared three deconvolution methods: Richardson-Lucy, Wiener filtering, and nonnegative least squares to determine the best performance using simulated full waveforms from radiative transfer modeling; the Richardson-Lucy method was found to have superior performance for deconvolution of the simulated full waveforms. Parrish *et al.* (2011) presented an empirical technique to compare three different methods for full waveform processing: Gaussian decomposition, Expectation-Maximization (EM) deconvolution and a hybrid method (deconvolve-decompose). Using precisely located screen-targets in a laboratory, they arrived at the conclusion that there is no single best full waveform method for all applications.

Despite the recent focus on applications of FWL for topographic studies, it was first evaluated for the processing of LiDAR bathymetry (Guenther *et al.*, 2000). However, full waveform bathymetric LiDAR has not received much attention in the literature, especially compared to topographic FWL. This is likely due to the lack of available bathymetric LiDAR data-sets for the scientific community and the more complicated modeling required

for LiDAR bathymetry to compensate for factors such as water surface reflection and refraction, water volume scattering and turbidity that can complicate the propagation models and attenuate return strength resulting in a lower signal to noise ratio (SNR). Water volume scattering can be difficult to rigorously model, especially for shallow water environments where water surface backscatter, water volume scattering, and benthic layer backscattering are mixed in a single complex waveform that makes discrimination of individual responses from a single return difficult (Abady *et al.*, 2014). The complex waveform signals in a bathymetric environment demand a noise-resistant and adaptive signal processing methodology. In order to reduce the complexity of bathymetric LiDAR, multiple wavelength (usually a NIR LiDAR system for water surface detection, and a green LiDAR system for water penetration) systems are normally used to facilitate benthic layer retrieval (Irish *et al.*, 2000). For example, Allouis *et al.* (2010) compared two new processing methods for depth extraction by using near-infrared (NIR), green and Raman LiDAR signals. By combining NIR and green waveforms, significantly more points are extracted by full waveform processing and better accuracy is achieved. Even though multi-wavelength LiDAR systems are common for bathymetry, single band systems have emerged recently as well (Fernandez-Diaz *et al.*, 2014; McKean *et al.*, 2009; Pfennigbauer *et al.*, 2011; Shrestha *et al.*, 2012). Wang *et al.* (2015) has compared several full waveform processing algorithms for single band shallow water bathymetry using both simulated and actual full waveform data, and concluded that Richardson-Lucy deconvolution performed the best of the tested waveform processing techniques. However, the performance with the actual full waveform data was not verified with comparison to external high accuracy truth data. There have also been several studies which have examined the performance of single band full waveform bathymetry using simulated LiDAR datasets. Abady *et al.* (2014) proposed a mixture of

Gaussian and quadrilateral functions for bathymetric LiDAR waveform decomposition using nonlinear recursive least squares. Both satellite and airborne configurations were simulated and examined and the algorithm showed significant improvement for bathymetry retrieval, however, the simulation has not to date been validated with observations from real-world studies, especially for very shallow water bathymetry in turbid conditions. The performance of full waveform LiDAR in shallow water has received little attention in the literature beyond the study by McKean *et al.* (2009). Limited water depths and significant turbidity impose challenges for bathymetric LiDAR, especially for longer pulse width laser systems where water surface, water column and benthic layer return mix together. A bathymetric full waveform processing strategy to account for the longer pulse width and the excessive noise present in the bathymetric waveform would enable more accurate bathymetry determination.

In this chapter, we first propose a novel full waveform processing algorithm using a continuous wavelet transformation (CWT) to decompose single band bathymetric waveforms. The seed peak locations acquired from CWT are then used as input to both an empirical system response (ESR) algorithm and a Gaussian decomposition. As a benchmark for comparison, a common Gaussian decomposition algorithm is also used with candidate seed locations acquired from second derivative peaks, similar to that presented in (Wagner *et al.*, 2006; Chauve *et al.*, 2007). The waveform processing methods are applied to two distinct fluvial environments with varying degrees of water turbidity. Water depths extracted from both a discrete point cloud and full waveform processed point clouds are then compared to water depths measured in the field with Acoustic Doppler Current Profiler (ADCP). Finally, we analyze the accuracy of water surfaces extracted from the discrete point cloud and full waveform processed point clouds using both green wavelength and near-infrared detected water surfaces compared to GNSS RTK field measurements.

4.2 Method and Mathematical Model

FWL return profiles are normally a fixed length discrete time signal containing backscatter information along the laser cone diffraction. For return profiles where the echoes are clustered in a short range window, a significant portion of the full waveform does not carry useful information (i.e. the profile represents the noise threshold); an effective method to pre-process the full waveforms that removes this extraneous information from the original waveform will reduce the total amount of processing time required. A noise level can be defined as the minimum amplitude and can be estimated from the full waveform data itself; for example as the median absolute deviation for each waveform (Persson *et al.*, 2005). For our study, amplitudes within 10% of the return gate are considered to be within the noise level (Figure 4.1). The return gate is an instrument specific configuration parameter used to reduce the effect of sun glint and noise returns. Herein, all the bins below the noise level were removed, and only the remaining signal was examined. The removal of data below the noise threshold significantly speeds up the calculations due to the decreased data volume to be analyzed. It should be noted that bathymetric LiDAR waveforms can have quite complicated return energy profiles. To demonstrate this, representative samples of bathymetric waveforms are given in Figure 4.2.

4.2.1 Continuous wavelet transformation

The wavelet transformation can be used to project a continuous time signal into multiple subspaces consisting of wavelets (Vetterli and Herley, 1992). By examining this projection, objectives such as denoising, compression, filtering and other applications can be achieved. A continuous wavelet transformation (CWT) projects the signal into a continuous time and scale subspace (instead of discrete subspaces) whereby the signal can be reconstructed from the resulting continuous components (Vetterli and Herley, 1992; Heil and Walnut, 1989). CWT is a very effective method to detect the peak locations in an

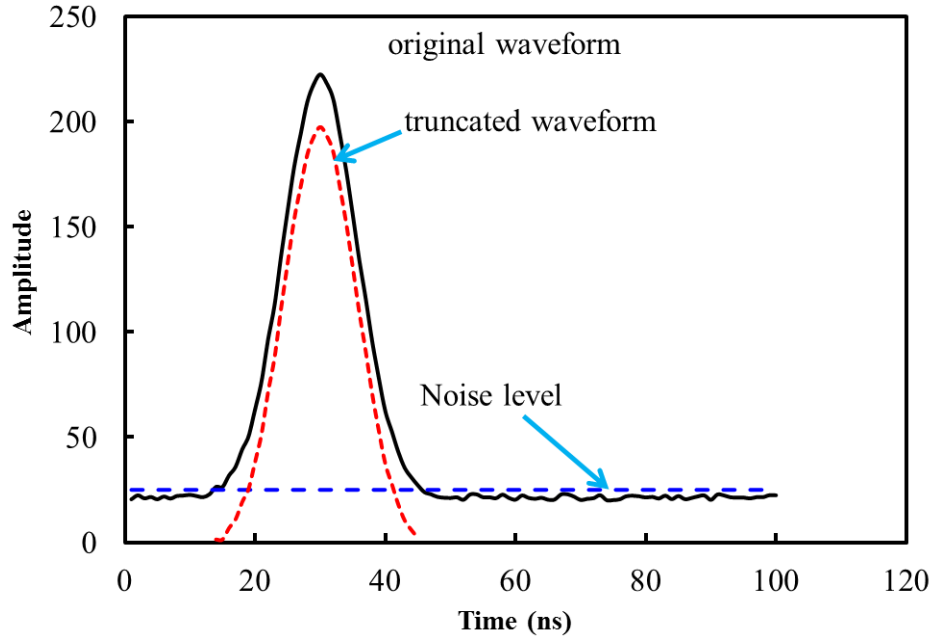


Figure 4.1 Pre-processing of the return waveform by removing data below the noise threshold of the original waveform. The noise level is defined as 10% above the return gate which is given by the manufacturer specifications.

overlapped waveform (Gregoire *et al.*, 2011). Extending the use of CWT to FWL thus is natural since the return waveforms can be highly mixed due to potentially closely spaced backscatters along the laser path.

CWT can construct a time frequency representation of a signal that offers very good time and frequency localization, making it suitable to localize peak locations as initial approximations for subsequent peak estimation algorithms. The mother wavelet template should be continuously differentiable and compactly support scaling and capture of a high vanishing moment. Because most FWL systems have Gaussian-like output signals, the Lorentzian of Gaussian mother wavelet has been used in this study (Gregoire *et al.*, 2011), and is given in Equation 4.1

$$\omega_{a,b}(t) = [1 - (\frac{t-b}{a})^2] \exp[-(\frac{t-b}{\sqrt{2}a})^2], \quad (4.1)$$

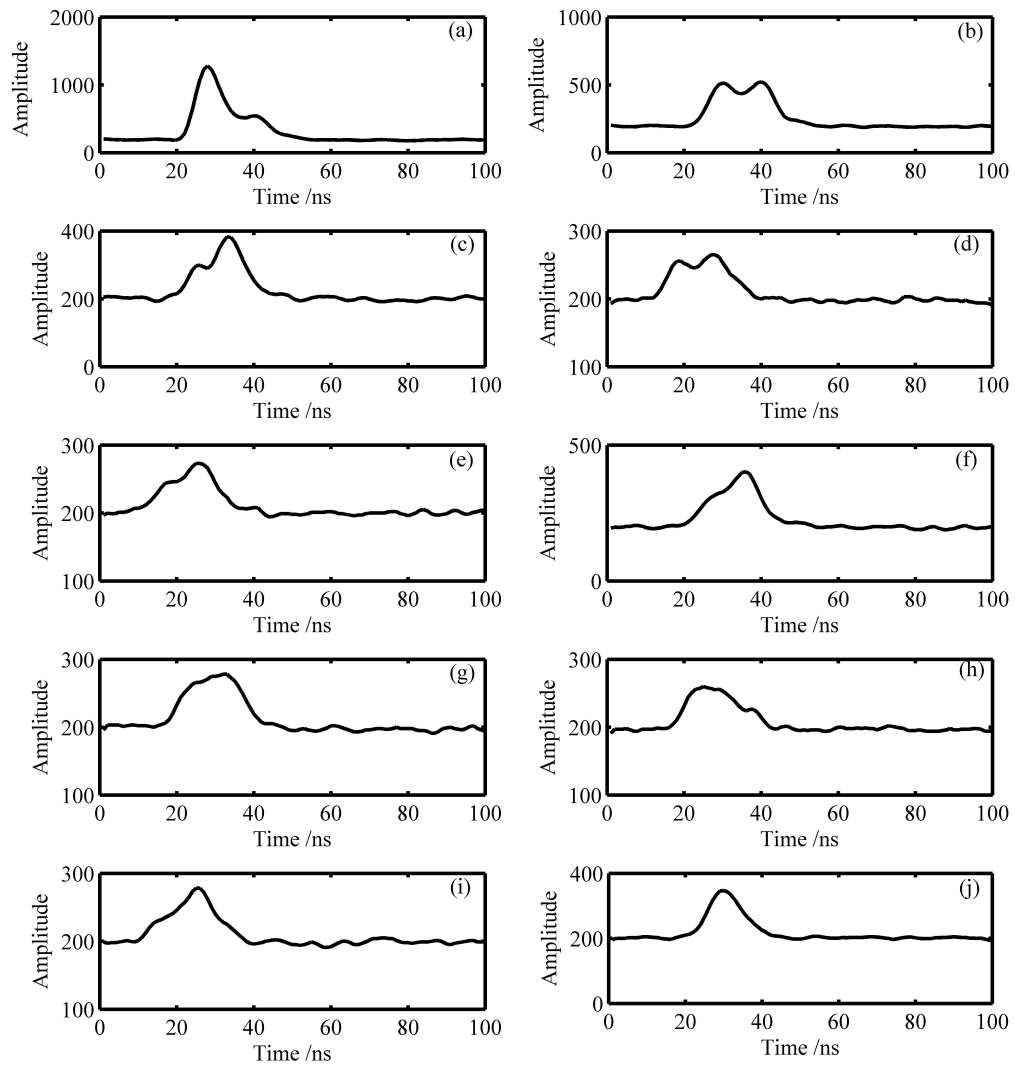


Figure 4.2 Typical bathymetric return waveforms. (a)-(d) clear water; (e), (f) contain more subtle evidence of multiple peaks; (g)-(i) overlapped returns; (j) single peak.

here, $\omega_{a,b}$ is the mother wavelet used in CWT, a dilates the mother wavelet and b translates the mother wavelet, and t is time. Special caution is needed for determination of a and b . A smaller a can assist in discriminating highly overlapped peaks, but a slight undulation of the waveform may result in a false peak. Larger values of a can resist disturbing undulations (i.e. noise) but could miss weak returns and result in single returns for multiple echoes; however, the smallest a cannot be less than the digitizing interval of signal. The ridge defined in Gregoire *et al.* (2011) is a good implementation for the detection of peaks (and a determination of a) but requires a significant amount of computation, so instead we directly chose a single value for a to detect potential peaks. In our studies, a is set to 1.0 ns because the interval of full waveform samples is 1.0 ns and b was set to 0.1 ns for both study sites. A value of 0.1 ns for b is equivalent to 1.5 cm in air. Parameters a and b can be adjusted to fit different applications and different FWL systems. The wavelet decomposition process is a good noise-resistant subspace representation of a signal, and therefore a simple local maximum filter can be used to find the peak locations after a wavelet transformation. In our study, a window with a size of 15 ns was used to detect the local maxima for the peak locations as the Full Width at Half Maximum (FWHM) is 8.3 ns for the Optech Aquarius LiDAR system used in this study (Fernandez-Diaz *et al.*, 2014).

4.2.2 Gaussian decomposition method

Gaussian decomposition is a popular approach for FWL processing as it can simultaneously provide estimates of peak location and width. Gaussian decomposition is implemented using Expectation-Maximization (EM) in this study. EM is an iterative method, normally used in signal and image processing, to estimate the maximum probability for a set of parameters in a statistical model. As the name indicates, there should be an expectation (E) step and a maximization (M) step, and EM iterates between the E step and the M step until a convergence criterion is satisfied (Persson *et al.*, 2005; Oliver *et al.*, 1996).

A LiDAR waveform return can be represented as the sum of multiple Gaussian distributions (Wagner *et al.*, 2006), and mathematically this can be expressed as

$$f(t) \sim \sum_{i=1}^n N(\mu_i, \sigma_i), \quad (4.2)$$

here, $f(t)$ is the full waveform that is the sum of multiple Gaussian components (n), t is time, and $N(\mu_i, \sigma_i)$ represents a Gaussian component with an individual mean (μ_i) and a standard deviation (σ_i). The number of peaks and the initial peak locations are needed as initial values for the EM algorithm described by the following equations:

$$Q_{ij} = \frac{p_j f_i(i)}{\sum_{j=1}^k p_j f_i(i)}, \quad (4.3)$$

$$p_j = \frac{\sum_{i=1}^S N_i Q_{ij}}{\sum_{i=1}^S N_i}, \quad (4.4)$$

$$\mu_i = \frac{\sum_{i=1}^S N_i Q_{ij} i}{p_j \sum_{i=1}^S N_i}, \text{ and} \quad (4.5)$$

$$\sigma_i = \sqrt{\frac{\sum_{i=1}^S N_i Q_{ij} (i - \mu_i)^2}{p_j \sum_{i=1}^S N_i}}, \quad (4.6)$$

here, p_j is the relative weight of the component distribution $f_i(x)$; Q_{ij} is the probability that sample i belongs to component j ; N_i is the amplitude for sample i ; S is the number of samples in the waveform; μ_i is the mean peak location; and σ_i is the standard deviation for that component, which is proportional to the pulse width or FWHM.

As EM is a local maximum searching method, peaks with spurious μ_i or σ_i are removed to ensure a reasonable result. Also, extremely weak returns, for example, peaks

with p_j less than 0.05 are removed to guarantee algorithm convergence. From Equation 4.3 to 4.6, it is evident that EM is actually a Gaussian decomposition because its underlying model is a Gaussian mixture model. For the purpose of assessing performance of Gaussian decomposition with different peak seeding locations, both CWT detected peak locations and peaks acquired from a second derivative analysis (Chauve *et al.*, 2007) are applied to initialize the EM estimation.

4.2.3 Empirical System Response Waveform Decomposition

An alternative to the Gaussian model for waveform decomposition is an empirical system response (ESR) model that represents the convolution of the emitted pulse shape and the sensor response. Decomposition with an ESR model has the potential to reduce residuals and improve ranging precision compared to Gaussian decomposition (Hartzell *et al.*, 2014). The method described in Hartzell *et al.* (2014) requires an ESR model spanning the dynamic range of a terrestrial LiDAR sensor to accommodate nonlinear response characteristics. However, for an FWL sensor with a predominantly linear response, which includes the airborne systems used in this study, a simplified ESR waveform decomposition method can be derived.

In lieu of an ESR model spanning the sensor dynamic range, a single empirical response model can be approximated by averaging waveforms from a single, diffuse, extended target illuminated at normal incidence. Using standard nonlinear least squares, the model is iteratively shifted (μ parameter), scaled in amplitude (A parameter), and scaled in width (w parameter) until the parameter corrections are negligible, i.e., the model is fit to the observed waveform in an optimal sense. An un-weighted Gauss-Newton least squares expression can be written in matrix form as (Ghilani, 2010):

$$JX = K + V \text{ and} \tag{4.7}$$

$$X = (J^T J)^{-1} J^T K, \quad (4.8)$$

where J is the $m \times 3$ matrix (m = number of waveform data points) of partial derivatives of the ESR model with respect to the μ , A , and w parameters evaluated at each waveform data point; K is the column vector of differences between the observed waveform amplitudes and the amplitudes computed from the ESR model; V is the column vector of residuals; and X is the column vector of ESR model parameter corrections. The partial derivatives required to populate the J matrix are numerically computed from the ESR model using the current parameter values at each iteration in the adjustment. Figure 4.3 illustrates the numeric partial derivatives. As with Gaussian decomposition, the least squares algorithm can be extended to accommodate a superposition of multiple ESR models when overlapping return echoes are detected in the observed waveform.

4.2.4 Water Depth Generation

Because the field measurements used in the study are water depth records collected with an acoustic doppler current profiler (ADCP), we need to infer water depths from the 3D LiDAR points as a basis of comparison. We also need to segment the raw point clouds from each of the target extraction techniques to separate water column and bottom returns and properly identify the benthic layer. The basic strategy for benthic classification is to first classify the last of multiple returns as initial candidate benthic returns, and then use a region growing method with the initial benthic points and regionally lowest elevation points to refine the total benthic surface points using the TerraScan software package. The classification algorithm is similar to that used to determine ground returns in topographic LiDAR surveys and is based on the methodology presented in (Axelsson, 2000). It should be noted that each of the green LiDAR returns from below the surface of the water has been corrected for both refraction of the pulse at the air/water interface, and for the change in the speed of light within water (Guenther *et al.*, 2000). To define the water boundary a

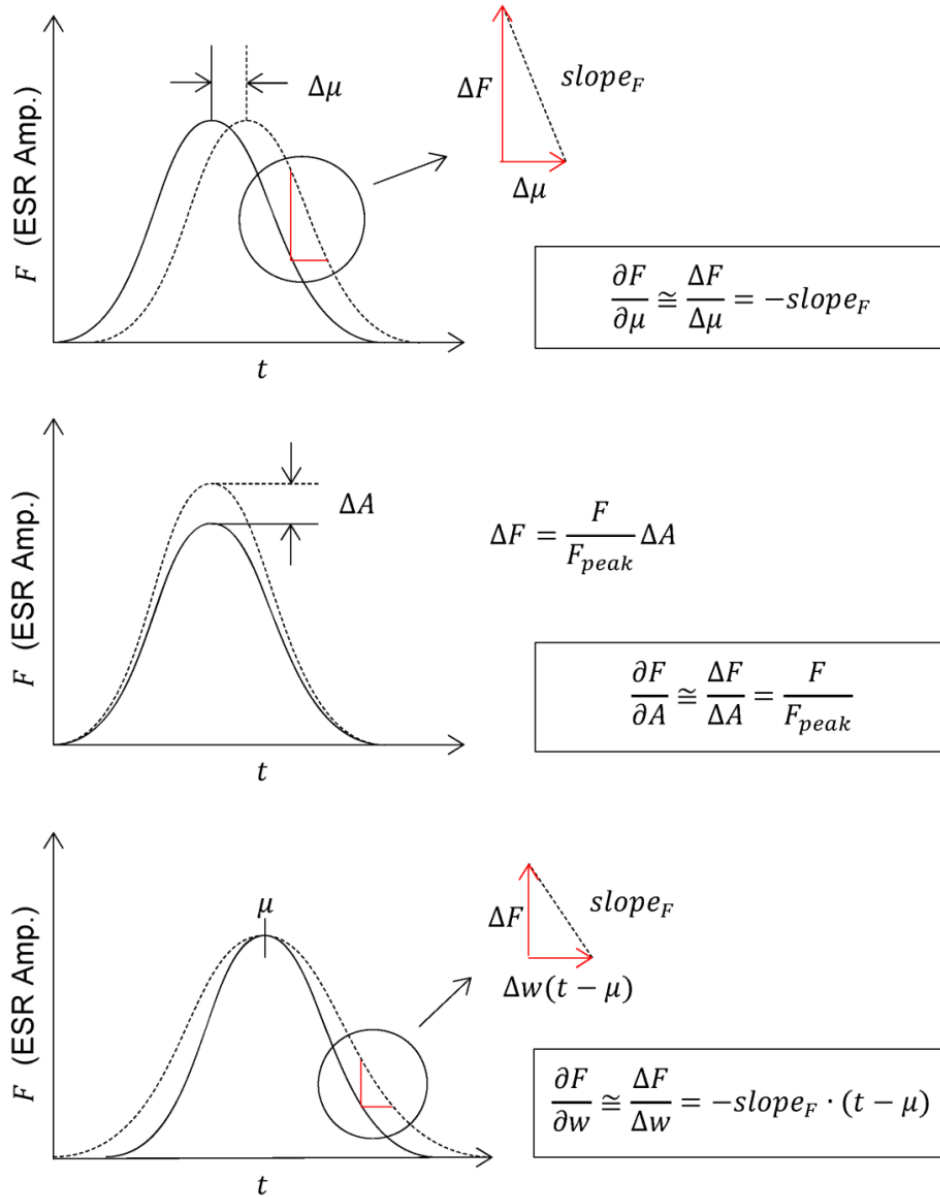
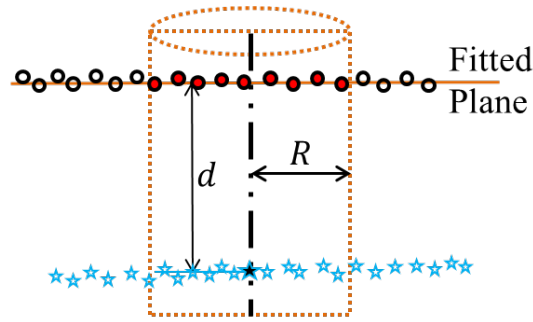


Figure 4.3 Graphical representation of numeric partial derivatives necessary for the empirical system response least squares waveform decomposition algorithm.

fluvial river-line is acquired from aerial orthoimages by visually identifying and digitizing the land/water border.

To convert the benthic layer points extracted from the point cloud to water depths, a water surface is required to subtract the benthic layer elevation from the water surface elevation for each benthic point. To highlight the differences in depth determination between single and multiple band bathymetric LiDAR sensors we examine two realizations of the water surface for each river: the first water surface is extracted from alternative sources (NIR water surface for the Snake River, RTK water surface for the Blue/Colorado River) and the second water surface is extracted from each green LiDAR point cloud alone. For green LiDAR point clouds, the water surface can be defined as the remaining LiDAR returns within the boundary of the water body after benthic classification. The NIR water surface was acquired by extracting all NIR returns within the water boundary, as NIR LiDAR can theoretically only be retro-reflected from the water surface (Irish *et al.*, 2000).

Point clouds created by airborne LiDAR are generally irregularly distributed, and therefore conventional image processing techniques which assume raster input are not suitable for posterior analysis. As an alternative, we utilized a point to plane distance to compute the distances between an individual LiDAR returns and its neighbor points (Hauser, 2013). Figure 4.4 shows the schematic steps to compute the point to plane distance. For each specific candidate point, neighbor points are selected within the cylinder with a specific search radius R , and thus a fitted plane is constructed by least squares estimation. The distance from the candidate point to the fitted plane is defined as the point to plane distance d . The point to plane distance is used in this study to calculate the water depth given a cloud of water surface (reference points) and benthic points (target points).



- Reference point ★ Target point
- Neighbor point ★ Candidate point

Figure 4.4 Definition of point to plane distance.

4.3 Results

4.3.1 Experiment I: Snake River Bathymetry Study

Distribution of Number of Full Waveform Returns

Four different full waveform processing algorithms have been applied in this study. The full waveform data for the Snake River was first preprocessed to reduce computational load by thresholding the raw waveform returns. To analyze the effect of the initial peak location estimates on nonlinear least square Gaussian decomposition, peak locations that were detected with a second derivative and peak locations that were detected with a CWT were both used as initial approximations for Gaussian decomposition. The resulting point clouds are referred to as s_G (Gaussian decomposition initiated with second derivatives) and c_G (Gaussian decomposition initiated with CWT) respectively. The peak locations detected by CWT are also used as initial seed values for the ESR pulse fitting. A point cloud was also generated by using just the peak locations derived from CWT without further Gaussian or ESR refinement. The four point clouds from these full waveform fittings are then used for further analysis.

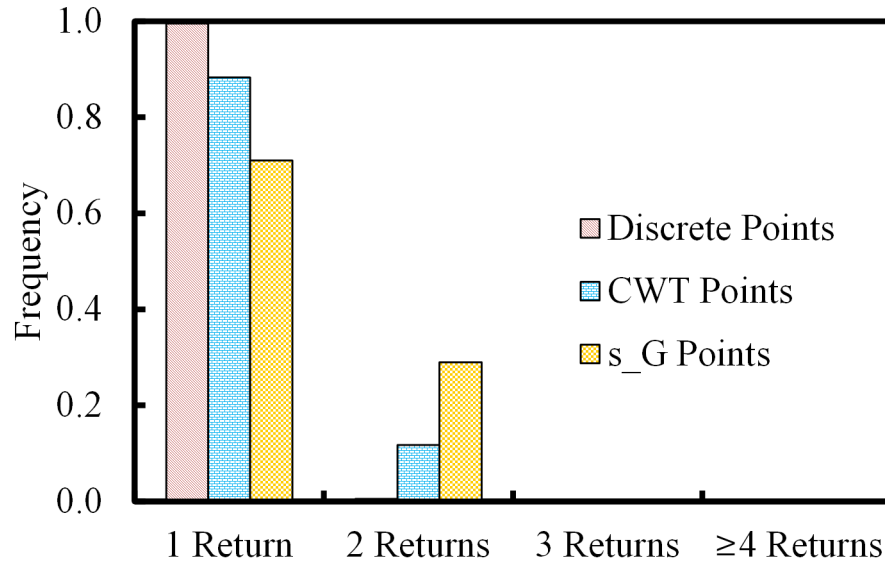


Figure 4.5 Distribution of the number of full waveform returns using different peak detection methods for the Snake River. CWT and s_G methods are better able to detect multiple returns while almost all discrete points are single return.

The CWT and s_G algorithms generated 24.32% and 43.35% more points respectively compared to the discrete points based on CFD provided by the manufacturer software, for the Snake River. The distribution of the number of returns for discrete points, CWT and s_G are shown in Figure 4.5. This suggests that s_G performs better than CWT for peak detection in the fluvial environment of the Snake River. More importantly, both CWT and s_G methods are markedly better at resolving multiple returns; almost all discrete points are composed of single return points. More return points have a direct benefit for bathymetric mapping as better coverage and higher density data is the result. In addition, multiple returns are also critical for shallow water bathymetric mapping as the surface returns and benthic returns are more likely both represented with multiple reflections. It should be noted that the ESR and c_G methods are not given in Figure 4.5 because they were both seeded by the CWT peak locations and therefore theoretically have the same statistics as the CWT results.

Water Depth Analysis

To avoid local anomalies (e.g., floating wood, submerged objects, facets of waves, etc.), for each benthic point, the point to plane distance is calculated as water depth with a search radius of 10 m for both the NIR and green water surfaces. To evaluate full waveform bathymetric LiDAR performance, the retrieved water depths have been compared to field measured ADCP depths. Figure 4.6 shows all the possible combinations of water depths compared to ADCP water depths and Table 4.1 shows the statistical comparison results for each water depth estimate.

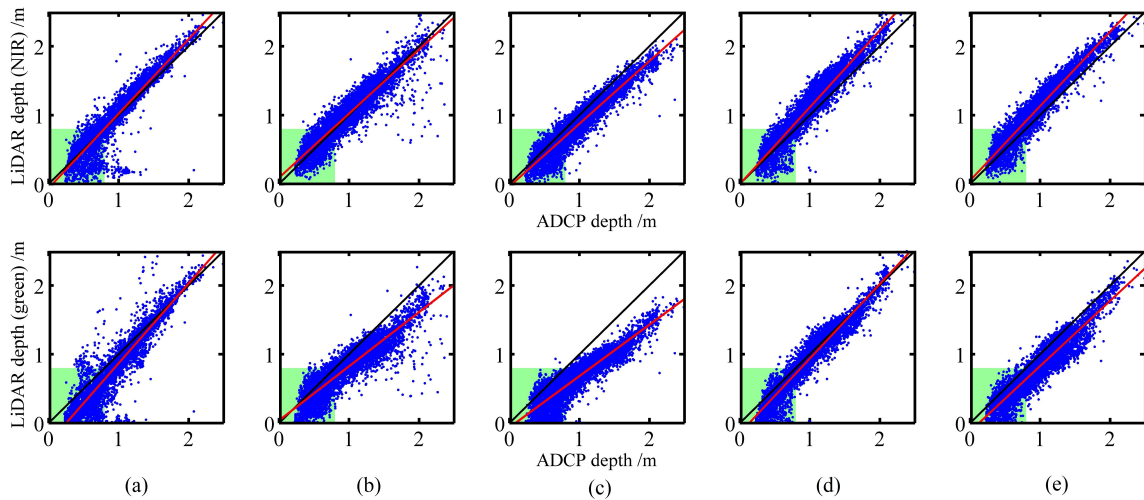


Figure 4.6 Comparison of LiDAR depths to ADCP depths for the Snake River. (a) discrete points, (b) s_G points (c) c_G points, (d) CWT points, (e) ESR points.

Table 4.1 Comparison of LiDAR retrieved water depths to field measured ADCP water depths for the Snake River. Results in meters.

Point Type:	discrete		s_G		c_G		CWT		ESR	
Water Surface:	NIR	Green								
Mean($Z_f - Z_r$)(m)	-0.02	0.13	-0.02	0.18	0.13	0.32	-0.11	0.06	-0.13	0.17
Std.($Z_f - Z_r$)(m)	0.17	0.20	0.16	0.18	0.14	0.17	0.15	0.14	0.13	0.14
Slope	1.08	1.16	0.93	0.79	0.91	0.75	1.12	1.08	1.08	0.95
Intercept (m)	-0.06	-0.29	0.09	0.04	-0.04	-0.06	0.00	-0.14	0.05	-0.12
R2	0.87	0.87	0.87	0.81	0.90	0.83	0.91	0.92	0.92	0.88

* Z_f is ADCP water depth and Z_r is LiDAR derived water depth

With the NIR water surface, ESR performs the best with the lowest standard deviation

(Std.) of 13 cm and the highest R^2 of 0.92; water depths retrieved from discrete points have slightly higher Std. of 17 cm and lower R^2 of 0.87. With a green water surface, CWT performs the best with a Std. of 14 cm and the highest R^2 of 0.92 while s_G water depths and c_G water depths have the worst performance with 18 cm and 17 cm for Std., 0.81 and 0.83 for R^2 respectively. The mean bias of water depth using a NIR water surface is lower than the mean bias with a green water surface except for CWT derived points; this is likely caused by water volume scattering and the overlap of benthic and surface returns for shallow water. In addition, the R^2 values for water depths retrieved with a NIR water surface are higher than those for water depths retrieved with a green water surface with the exception of the CWT points (0.87 vs. 0.87 for discrete points, 0.87 vs. 0.81 for s_G points, 0.90 vs. 0.83 for c_G points, 0.92 vs. 0.88 for ESR). These differences indicate that NIR returns give a more accurate water surface than green returns. The CWT methodology is the lone outlier, and shows the opposite performance as water depths retrieved with a green water surface are better than water depths retrieved with a NIR water surface (-11 cm vs. 6 cm for mean depth error, 15 cm vs. 14 cm for Std., 0.91 vs. 0.92 for R^2 respectively). This suggests that the CWT is more effective than the other methods for green LiDAR waveform processing as it provides a better estimate of the water surface.

The water depths retrieved from c_G points are slightly better than water depths retrieved from s_G points (with NIR water surface: 14 cm vs. 16 cm for Std., 0.90 vs. 0.87 for R^2 respectively; with green water surface: 17 cm vs. 18 cm for Std., 0.83 vs. 0.81 for R^2 respectively). This suggests that the initial peak location estimates have an effect on the final least square estimates, and that CWT provides marginally better seed locations. The green shaded areas (depths < 0.8 m) in Figure 10 indicate that all shallow water depths retrieved from LiDAR observations have been underestimated. Theoretically, LiDAR can underestimate water depth because of overlap between the surface return and benthic return for extremely shallow water. Also, any suspended particulate matter in the

water body, or a rough benthic layer can stretch the incident laser pulse. For very shallow water (green shaded area), the final laser return will be a superposition waveform of water surface backscatter, water volume backscatter and benthic layer backscatter.

Because Table 4.1 shows significant differences between water depths with either an NIR or green water surface definition, a further inspection of these water surface definitions is warranted. The NIR water surface shows the best overall internal consistency, with a Std. of 11.76 cm for planar fits of points within a 2 m search radius. Therefore the NIR water surface is used as a common basis for comparison for all the green water surfaces by calculating the point to plane distance with a 2 m search radius from the green LiDAR points to the NIR surface plane. As Table 4.2 shows, different green water surfaces have significantly different mean vertical errors with ESR having the largest at 45 cm and c_G the smallest at 17 cm. The discrete water surface has only a 10 cm of Std., indicating that the discrete point cloud estimates the water surface well (at least for the Snake River conditions). However, the overall performance (i.e. determining water depths) from discrete returns is not as good as CWT and has a Std. of 24 cm for the water surface; this implies that a CFD is unable to properly estimate benthic returns in the presence of water column backscatter. The c_G method performs better than s_G for water surface detection with 17 cm versus 34 cm for mean vertical error, and 28 cm and 31 cm for Std. respectively. Again, this is further evidence that an accurate initial peak estimate is necessary for nonlinear Gaussian decomposition.

Table 4.2 Statistical mean vertical error and Std. for different green water surfaces. NIR water surface has an 11.76cm Std..

Water Surface	discrete	s_G	c_G	CWT	ESR
Mean (m)	0.18	0.34	0.17	0.29	0.45
Std. (m)	0.10	0.31	0.28	0.24	0.33

4.3.2 Experiment II: Blue/Colorado River study

Distribution of Number of Full Waveform Returns

To further assess full waveform bathymetric LiDAR performance, we performed another study on the Blue/Colorado River, which has significantly more turbid water than the Snake River. Similar to the Snake River analysis, all four full waveform processing algorithms were applied to extract individual point clouds. Only 4.6% more points were detected with a CWT over discrete returns. The s_G method actually gave 2.07% fewer points than the discrete. The distribution of returns for this fluvial environment is shown in Figure 4.7. Note that, CWT extracted significantly more multiple returns while almost all discrete returns are single return. Again, more multiple returns in general mean better separation between water surface and benthic layer. The same region growing classification methodology described for the Snake River was also applied to the Blue/Colorado River point clouds.

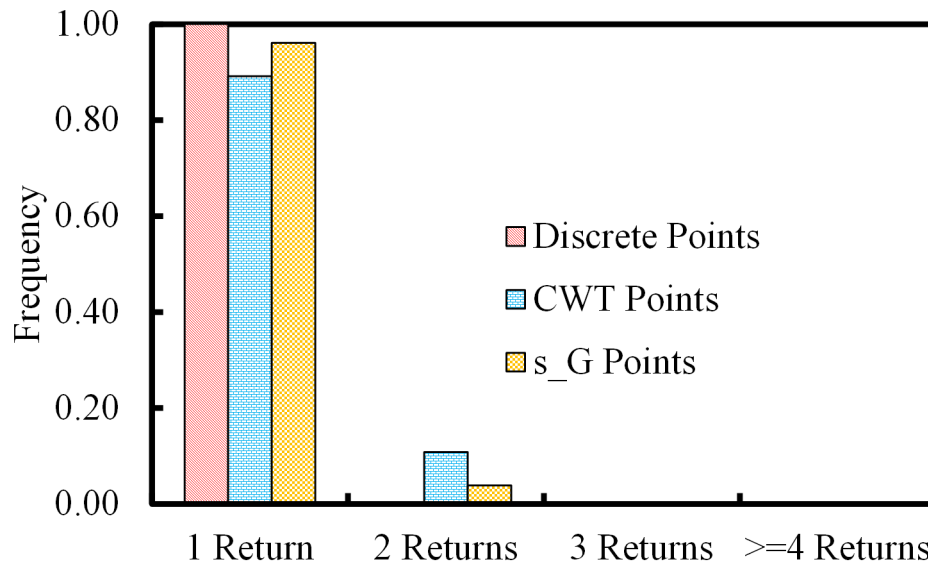


Figure 4.7 Distribution of the number of full waveform returns for different peak detection methods on the Blue/Colorado River. CWT and s_G methods are better able to detect multiple returns while almost all discrete points are single return.

Water Depth Analysis

After extracting benthic returns from the full waveform and discrete point clouds, a water surface was required to retrieve water depths for comparison with the ADCP measurements. In contrast to the Snake River, no effective NIR water surface was acquired during the airborne LiDAR data collection because of high flight altitude (2.6 km above ground) of the NIR collection (see Fig.3 (b) in Fernandez-Diaz *et al.* (2014)). Therefore, instead of using a NIR water surface we have used a field measured RTK water surface. The RTK water surface locations were recorded during the ADCP water depth collection as shown in Figure 3.1. In addition, the water surface returns from the discrete CFD derived bathymetric points proved to have extremely low density, and therefore no water surface was estimated from the discrete returns. Therefore, for the Blue/Colorado River only four sets of water depths were compared with the green water surface. For each benthic point, the point to plane distance is calculated with a search radius of 10 m for both RTK water surface and green water surface. The comparison between the LiDAR and ADCP depths are given in Figure 4.8 and Table 4.3.

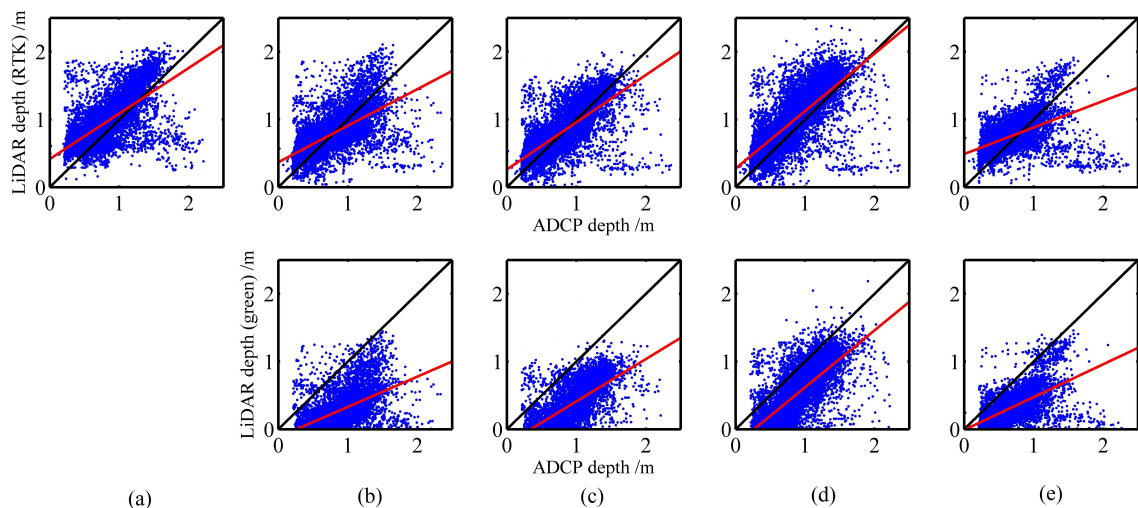


Figure 4.8 Comparison of LiDAR depth to ADCP depth for the Blue/Colorado River. (a) discrete points, (b) s_G points (c) c_G points, (d) CWT points, (e) ESR points.

All waveform algorithms performances have degraded in the turbid water of the Blue/Colorado

Table 4.3 Comparison of LiDAR retrieved water depths to field measured ADCP water depths for the Blue/Colorado River. Results in meters.

Point Type:	discrete		s_G		c_G		CWT		ESR	
Water Surface:	RTK	Green	RTK	Green	RTK	Green	RTK	Green	RTK	Green
Mean($Z_f - Z_r$)(m)	-0.17	N/A	-0.03	0.60	-0.04	0.55	-0.16	0.35	-0.10	0.35
Std.($Z_f - Z_r$)(m)	0.29	N/A	0.27	0.27	0.25	0.24	0.27	0.24	0.28	0.22
Slope	0.67	N/A	0.54	0.45	0.70	0.63	0.85	0.84	0.39	0.48
Intercept (m)	0.42	N/A	0.37	-0.12	0.26	-0.21	0.28	-0.22	0.49	-0.01
R2	0.44	N/A	0.41	0.29	0.53	0.43	0.57	0.58	0.25	0.39

* Z_f is ADCP water depth and Z_r is LiDAR derived water depth

River. The mean biases for s_G and c_G water depths with green water surface are significantly higher than that of the Snake River with values of 60 cm and 55 cm respectively. The Std. for all water depths retrieved with a green water surface is slightly lower than the Std. of water depths with RTK water surface, but with significantly higher mean biases. The highest R^2 of 0.58 was achieved by CWT water depths with a green water surface while CWT still gave the highest R^2 of 0.57 with the RTK surface. The more consistent results from the purely peak finding CWT algorithm suggests that the water turbidity substantially distorts the return waveform shape, which causes significant problems for algorithms such as Gaussian decomposition or ESR that make assumptions about the shape of the return energy profile. ESR performed relatively poorly in the Blue/Colorado River with only a R^2 of 0.25 for water depths with an RTK water surface and R^2 of 0.39 for water depths with green water surface.

The overall Std. for the c_G method is slightly better than the s_G method (with RTK water surface: 25 cm vs. 27 cm, with green water surface: 24 cm vs. 27 cm) and has a higher R^2 value (with RTK water surface: 0.53 vs. 0.41, with green water surface: 0.43 vs. 0.29). This difference reinforces that accurate initial peak estimates are critical for nonlinear least square Gaussian decomposition.

The differences in depth estimation between an RTK water surface and a green water laser surface necessitates a further assessment of the water surfaces used to infer water

depths. Given the water turbidity, we would expect the RTK water surface to have better performance. Therefore, we compare each green LiDAR water surface using the RTK surface as a common reference. For each green water surface point, the RTK points within 10 m are used to form a water surface plane and each green water surface point to plane distance to the RTK surface is defined as the planar uncertainty. Table 4.4 shows that all green water surfaces from the Blue/Colorado River have high mean error (s_G: 82 cm, c_G: 79 cm, CWT: 72 cm, ESR: 63 cm). The Std. (s_G: 16 cm, c_G: 13 cm, CWT: 17 cm, ESR: 18 cm) of all water surfaces are marginally better than those for the Snake River because the RTK water surface is less noisy than the NIR water surface used for comparison on the Snake River (NIR has 11.76 cm Std., RTK has 4.11 cm Std.). The significant mean vertical bias highlights the overall poorer performance of bathymetric LiDAR for the Blue/Colorado River. By comparing the results from Table 4.8, water depths calculated by using an RTK water surface has a smaller mean bias than green water surfaces. This suggests that the increasing amount of water volume scattering caused by the turbid water has skewed the mixture of water surface and volume scattering toward the bottom causing a larger mean error for green water surfaces. The relatively poor performance of green water surface extraction is troubling because it suggests that an independent accurate water surface, i.e. NIR water surface, is a necessity for turbid water depth determination.

Table 4.4 Statistical mean vertical error and Std. for different green water surfaces compared to a GPS RTK water surface. RTK water surface has a 4.11cm Std..

	s_G	c_G	CWT	ESR
Mean (m)	0.82	0.79	0.72	0.63
Std. (m)	0.16	0.13	0.17	0.18

Water Surface Detection Performance Analysis

In order to better study the impacts of water turbidity, we collected a few representative waveforms with CWT detected peaks and actual water surface locations calculated from RTK surveyed points. Figure 4.9 displays these individual bathymetric waveforms under

different water conditions, varying from shallower to deeper water and also varying from lower to higher turbidity. A single peak can be detected for shallow water with lower turbidity (Figure 4.9, (a) to (b)), shallow water with higher turbidity (Figure 4.9, (f) to (h)) and deeper water with higher turbidity (Figure 4.9, (i) to (j)). CWT detected peaks are closer to the actual water surface for more turbid water (Figure 4.9, (f) to (h)) and they move away from the actual water surface for lower turbidity water (Figure 4.9, (a) to (b)). The different behavior of full waveform detection in less turbid and more turbid water suggests that a significant amount of water volume scattering for more turbid water skewed the bathymetric returns toward the actual water surface.

However, a further analysis of Figure 4.9 shows the actual water surface (as measured by RTK) is located at the very beginning of the waveform. Therefore, it would appear that a simple leading edge detection method would be able to accurately estimate the actual water surface. We have set a leading edge detector with an amplitude threshold of 210 to define the water surface. Figure 4.10 shows the leading edge detected water surface as well as the CWT detected water surface. A significant vertical bias is present for the CWT detected water surface in profile A and profile B. This visual vertical bias confirms the significant increase of water surface error in Table 4.4. The leading edge detected water surface matches the RTK water surface very well, confirming that leading edge detection is effective for estimating the water surface in the Blue/Colorado River. In order to generalize the leading edge detection, the same method was also applied to the Snake River to independently assess performance. Figure 4.11 shows two profiles of the Snake River with leading edge water surface detection. A significant vertical bias is present in the Snake River leading edge water surface; the CWT detected water surface agrees much better with the NIR detected water surface. This result confirms that the biases in the waveform water surfaces for the Blue/Colorado River are caused by the increased water turbidity, and not by the waveform processing methodology. The different performance of leading edge

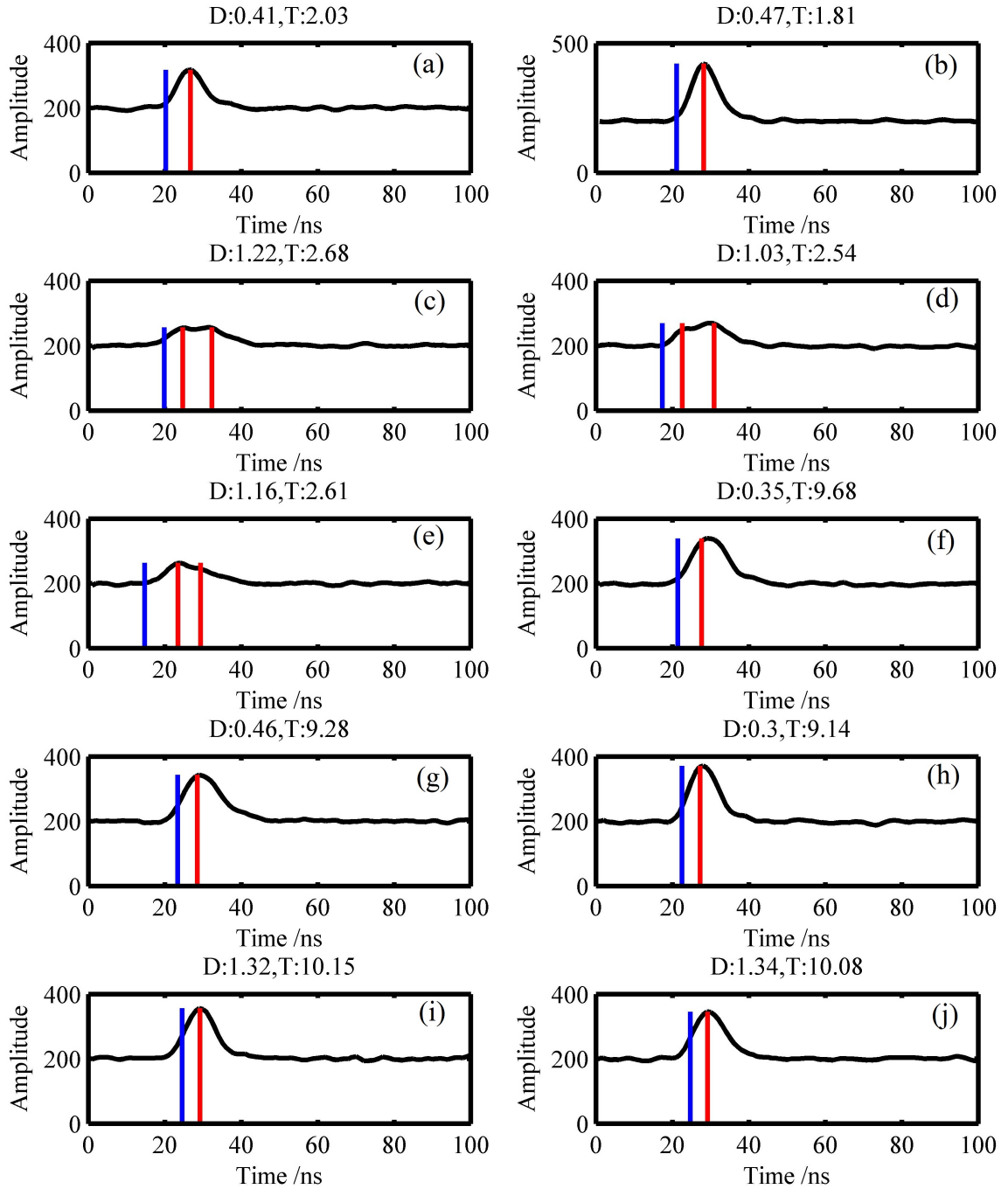


Figure 4.9 CWT peaks (red lines) and actual water surface location (blue lines). (a)~(b) shallow water with low turbidity; (c)~(e) deep water with low turbidity; (f)~(h) shallow water with high turbidity; (i)~(j) deep water with high turbidity.

water surface detection and the CWT water surface indicates that there may be no single solution that can be applied to all rivers to accurately estimate the water surface for single band LiDAR bathymetry.

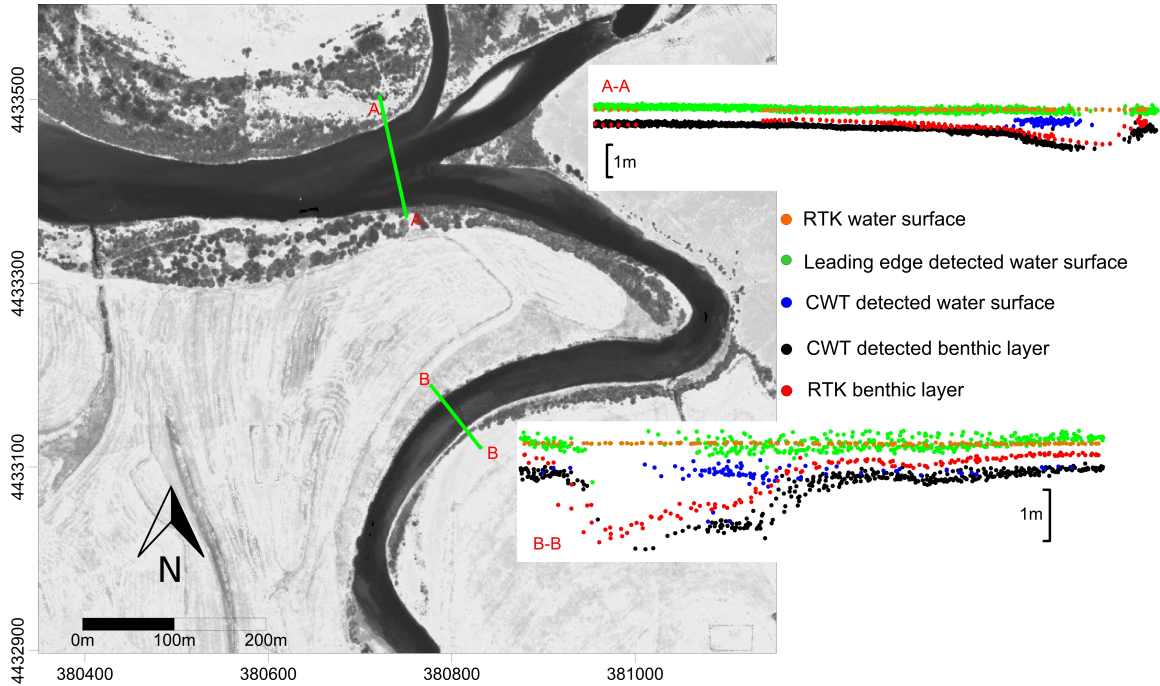


Figure 4.10 Profiles for leading edge detected water surface on the Blue/Colorado River. Coordinates are in UTM 13N (NAD83).

Table 4.5 Statistical mean vertical error and Std. for leading edge detected water surfaces. RTK water surface and NIR water surface are used as reference for the Blue/Colorado and Snake Rivers respectively.

	Blue/Colorado river	Snake river
Mean (m)	-0.01	-0.60
Std. (m)	0.19	0.27

Table 4.5 lists the statistical results for leading edge water surface detection for both the Blue/Colorado and the Snake River. For each leading edge detected point, the point to plane distances (RTK points are reference points for the Blue/Colorado River, NIR points are reference points for the Snake River) were used to form a plane by least squares estimation and the point to water surface plane distance is defined as the error. The leading

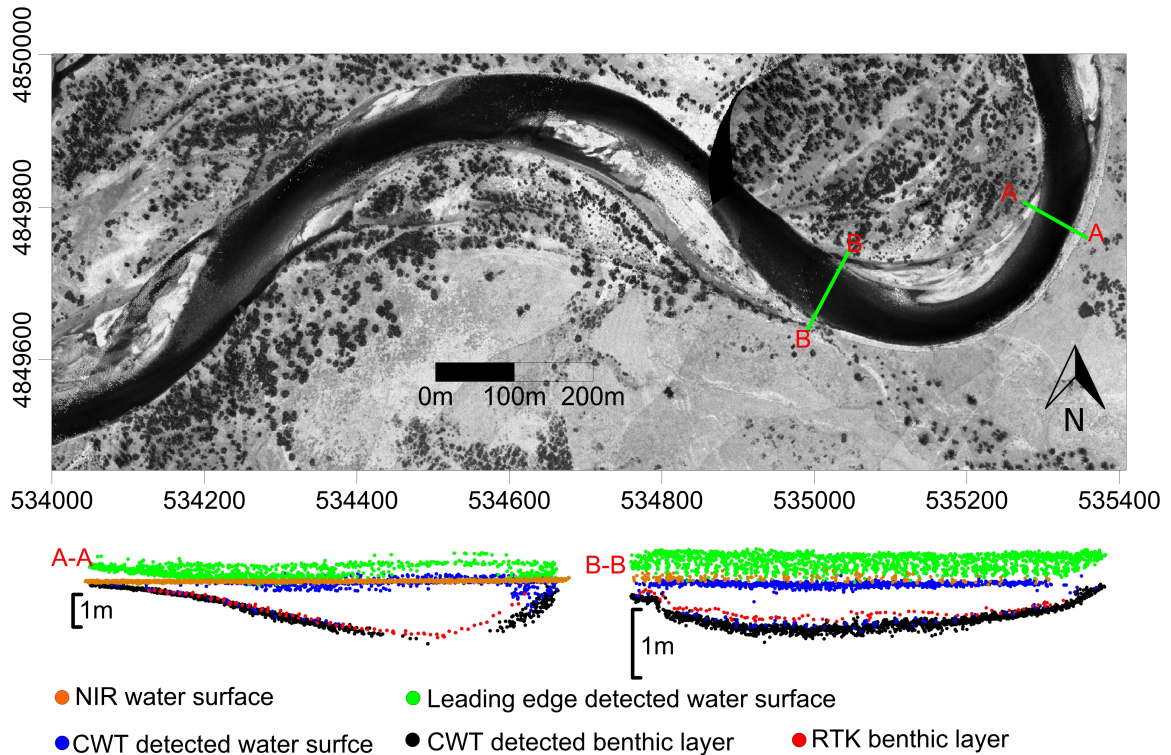


Figure 4.11 Profiles for leading edge detected water surface on the Rusty Bend of Snake River. The water surface detected with CWT matches the NIR water surface well. Coordinates are in UTM 12N(NAD83).

edge detection is poorer than the waveform derived surfaces for the Snake River as the water volume scattering with low turbidity is not significant. However, if the water becomes more turbid, then leading edge detection performs better than peak detection or waveform fitting methods.

4.3.3 Best Performance for Single Band Bathymetric LiDAR

If we specify only single band (green) LiDAR observations, then Table 4.2 shows that the most consistent water surface estimate for the Snake River is given by the discrete returns with an 18 cm mean bias and a 10 cm Std., and Table 4.5 indicates that leading edge detection yields the best representation of the water surface for the Blue/Colorado River with 1 cm of mean bias and 19 cm Std. Therefore, we can assess the best performance for single band green LiDAR in each study by combining the best estimate of water surface

with the best discriminator of benthic layer returns. For the Snake River, we combined a discrete water surface with CWT benthic layer returns to infer water depth. For the Blue/Colorado River we used leading edge detection for the water surface and combined it with CWT benthic layer returns. The optimal single band water depth maps are shown in Figure 4.12. Both optimized estimates of depth were compared to field measured ADCP water depth respectively, and the results are shown in Table 4.6.

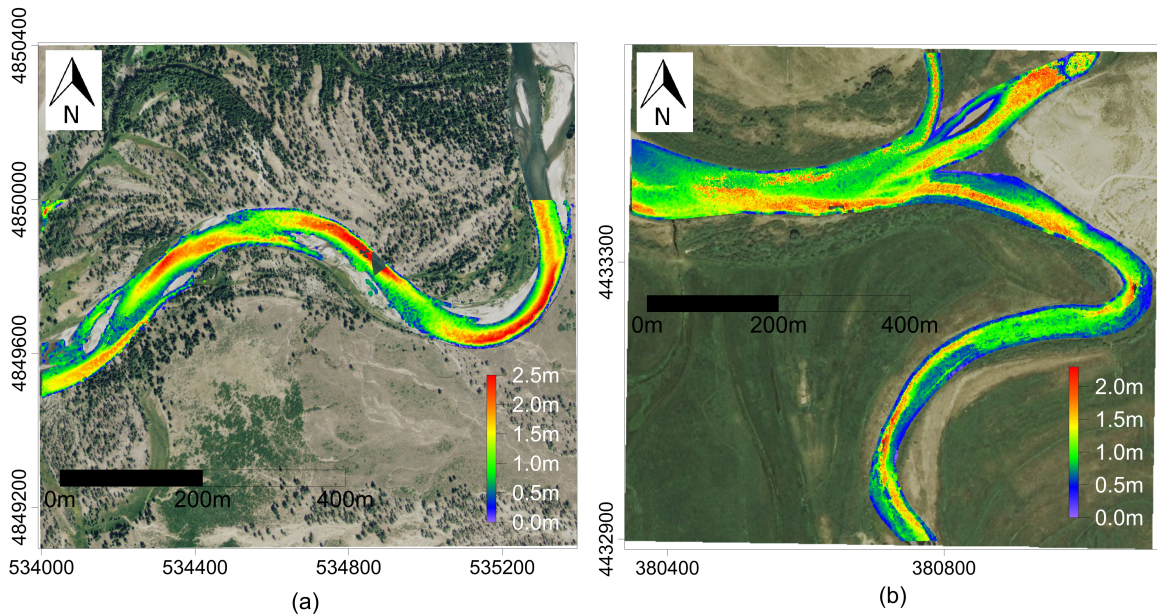


Figure 4.12 Optimal single band water depth map for the Snake River (a), Coordinates are in UTM 12N(NAD83) and the Blue/Colorado River (b), Coordinates are in UTM 13N(NAD83)).

Table 4.6 Best Performance for single band bathymetric LiDAR for both the Snake River and the Blue/Colorado River

	Snake River	Blue/Colorado River
Mean($Z_f - Z_r$) (m)	0.06	-0.16
Std.($Z_f - Z_r$) (m)	0.14	0.27
Slope	1.11	0.85
Intercept (m)	-0.06	0.27
R^2	0.93	0.58

The Snake River water depth inferred from a combination of discrete water surface and CWT benthic layer results in a 6 cm mean bias and 14 cm Std. with an R^2 of 0.93.

The results are comparable to the CWT water depth using a NIR water surface estimate in Table 4.1. The water depth inferred from a combination of leading edge detected water surface and CWT detected benthic returns for the Blue/Colorado River also shows similar performance to the CWT water depth with RTK water surface given in Table 4.3 (16 cm for mean bias and 27cm for Std. with R^2 of 0.58). This reinforces the fact that the leading edge detected water surface is close to the RTK water surface and the relatively significant errors present in the Blue/Colorado River results are heavily dependent on the accuracy of the benthic layer estimation.

4.4 Discussion

The objective of this study was to evaluate the performance of a single band full waveform bathymetric LiDAR with different processing algorithms and water surface definitions in two distinct fluvial environments. We proposed a novel full waveform processing algorithm based on a continuous waveform transformation; the detected peaks from CWT are used as candidate seed peaks for both Gaussian and ESR decomposition. The wavelet transformation was assessed in comparison with a more standard approach using Gaussian decomposition with initial peak estimates from a second derivative analysis. Water depths from each waveform method, along with discrete points produced by the real-time constant fraction discriminator were compared to field measured water depths. All the methods have been applied to two fluvial environments: the clear and shallow (mostly < 2 m) water of the Snake River and the turbid and shallow (mostly < 1.5 m) fluvial environment of the Blue/Colorado River.

Full waveform LiDAR processing is able to produce a significantly denser point cloud with more multiple return reflections than CFD for bathymetry. The ability to recover multiple returns by the waveform methods is especially significant, because the additional

returns are more probable benthic returns. Multiple returns can also benefit the classification of the benthic layer as the last return of multiple returns are assigned as seed benthic positions for region growing classification algorithms. This algorithm is different from the method proposed by Allouis *et al.* (2010) who used NIR returns to estimate the water surface; here the mixed LiDAR signal produced by water surface and water bottom reflections was directly processed through the CWT to extract both surface and benthic locations. One of the challenges for single band bathymetric LiDAR is to recover both the water surface and bottom position from the full waveform. The longer pulse width laser used in the Aquarius system exacerbated the mixture of water surface, water column and benthic returns. In the future we plan to examine our methodology on short pulse width bathymetric full waveform LiDAR systems such as the Riegl VQ 820-G, AHAB Hawkeye III, EAARL, and Optech Titan.

The results of the study also suggest that there is no superior full waveform processing algorithm for all bathymetric situations, which agrees with the conclusions of Parrish *et al.* (2011). ESR performed the best in the Snake River using a NIR water surface, with an R^2 of 0.92 and the lowest Std. of 13 cm. However, the c_G and CWT results for the Snake River with the NIR surface were statistically quite similar to the ESR results. With a green water surface the CWT performed marginally better than ESR with an R^2 of 0.92 versus 0.88, with an identical Std. of 14 cm. LiDAR for the Blue/Colorado River did not perform nearly as well as the Snake River study due to the significant water turbidity. CWT water depths with either an RTK or green water surface gave the best performance (R^2 of 0.57 and 0.58 respectively). In general the approaches that model expected signal shape (Gaussian and ESR) performed quite poorly for the Blue/Colorado River, suggesting that the water turbidity causes significant distortion in the return waveform shape. Based on this we can safely conclude that CWT is more stable than the other full waveform processing algorithms for shallow water fluvial environments. Both the ESR and CWT showed good

bathymetric performance for different cases, confirming that it is critical for commercial software to include a variety of full waveform processing strategies. However, unfortunately, the optimal processing strategy is not available a priori, and therefore a certain level of performance assessment is necessary for users to determine the best processing strategy for their study conditions. We have also compared water surfaces estimated by both NIR and Green LiDAR returns. There is a definite vertical bias between the two surface estimates. The comparison of the NIR and green water surfaces for the Snake River study showed a maximum mean vertical offset of 45 cm and 33 cm of Std. for ESR. The minimum average of 18 cm of vertical offset and 10 cm Std. are observed for the discrete green water surface. Overall, it appears that the NIR water surface gives slightly better results than using a green surface (for clear water). Turbid water greatly degraded the green water surface performance with large mean error (s_G: 82 cm, c_G: 79 cm, CWT: 72 cm, ESR: 63 cm). The deterioration of water surface performance compared with the clear Snake River indicates that turbidity can skew the return full waveform toward the benthic layer. McKean *et al.* (2009) suggested that suspended sediment and dissolved organic materials can scatter and absorb incident laser radiation. They also reported that turbid water exacerbates laser penetration for the EAARL system when turbidity reached 4.5 to 12 NTU. This agrees with our results, the Blue/Colorado River presented turbidity ranging from 2 to 12 NTU, which negatively impacted Aquarius performance due to substantial water column scattering. It also further confirms that a multiple wavelength LiDAR may be essential for bathymetric applications, especially for turbid water. A leading edge detection method was proposed and tested over these two river conditions; it was found that leading edge detection is effective if more water volume scattering is present (i.e., high turbidity), but waveform fitting methods are more effective for low turbidity due to the identification of more water surface returns.

In summary, full waveform processing can produce more points than discrete CFD

processing to provide better coverage and more multiple returns for better discrimination of benthic and water surface returns. However, with all approaches it is difficult to acquire good quality data for turbid water, especially when the water is shallow. The proposed CWT method shows better stability through varying water clarity conditions than the Gaussian or ESR decomposition methods also tested. A single band full waveform bathymetric LiDAR does not appear to be as accurate as a two wavelengths system that recovers the water surface using a NIR laser. However, with an appropriate full waveform processing algorithm, the error in determining the water surface from a single band green LiDAR can be mitigated; these results are encouraging because they seem to indicate that with improved detection of the water surface from the green LiDAR we can expect a single band LiDAR bathymetry system to perform similarly to a two band (NIR and green) bathymetric system. For this to be realized however, we must successfully extract the water surface from the relatively complex backscatter at the air/water interface, which we were unable to do with the waveform processing algorithms tested. In Abady *et al.* (2014), they proposed a quadrilateral signal to model the effect of water column scattering, and show it to be effective with simulated bathymetric LiDAR data. However, our initial analysis of this methodology has not shown a significant improvement in water surface estimation for the Aquarius data-sets examined. Future work will therefore focus on decoupling the water surface and water column scattering at the air/water interface.

Chapter 5

Estimation of Water Depths and Turbidity from Hyperspectral Imagery Using Support Vector Regression

5.1 Overview

The radiative transfer process described Chapter 2 showed that extracting water bathymetry from hyperspectral imagery is possible with both linear and band ratio methods (Legleiter *et al.*, 2009; Philpot, 1989; Stumpf *et al.*, 2003; Dierssen *et al.*, 2003). However, in the shallow fluvial systems present for the Snake and Blue/Colorado River, the linear solution including a deep water correction is difficult to implement (due to the absence of deep water), and therefore, only the band ratio method was implemented and evaluated herein. The band ratio method described by Legleiter *et al.* (2009) and Ma *et al.* (2014) has been shown in the literature to be simple to use and provide accurate bathymetric results from hyperspectral imagery, with a minimum number of tuning parameters. The main drawback of the band ratio method is that only a portion of the spectral information is utilized; however, all bands theoretically are attenuated by the water column with specific but wavelength dependent attenuation coefficients. Therefore all spectral bands should potentially contain water bathymetry information. A more generalized model, which takes advantage of a number of spectral channels, should improve bathymetric estimates. However, a specific model would be difficult to construct due to the complex and unknown relationship between spectral bands and water column response. A non-parametric method that utilizes all spectral information can be formulated, and could potentially improve bathymetry retrieval. It would also be preferable, if like the OBRA method the algorithm could be easily implemented without a requirement for extensive radiative transfer modeling.

Support vector machine (SVM) is a supervised machine learning algorithm used to analyze patterns within data, and support vector regression (SVR) is a realization of a support

vector machine for prediction (Smola and Vapnik, 1997). SVR is a non-parametric regression method and a data dependent learning scheme and thus no explicit model is required to fuse the observations with the physical measurement quantities. The regression model is generalized, and can be used to estimate any spectrally related parameters where no explicit physical model exists. A review of support vector machines and regression can be found in Mountrakis *et al.* (2011). Bruzzone and Melgani (2005) have estimated biophysical parameters from remotely sensed data using a multiple estimator system that incorporated SVM in combination with a multilayer perceptron (MLP) neural network. Camps-Valls *et al.* (2006) utilized the SVR method to estimate ocean chlorophyll concentration with satellite remote sensing data to provide a more accurate, less biased, and noise resistant model.

In this chapter, we propose and test SVR as an alternative method for bathymetric retrieval in order to more accurately account for the nonlinearity existing in the observed hyperspectral data. A conventional band ratio bathymetry retrieval method is used as a baseline for comparison with the proposed SVR method, and a comparison with *in-situ* water depth observations is presented. To demonstrate the generality of the SVR method, we also evaluate its ability to predict other water column parameters empirically by using it to estimate water turbidity from hyperspectral imagery. We again compare the results to *in-situ* measurements of turbidity.

5.2 Support Vector Regression

Support Vector Regression (SVR) is a non-parametric regression technique and therefore no assumptions regarding the underlying data model are required. SVR can transform a nonlinear regression problem into linear regression through the implementation of a kernel function, which projects the original feature space into a higher dimensional space. A hyperplane is then used to fit the projected space, and the estimated parameters can be used for subsequent prediction (Chang and Lin, 2011).

SVR is a supervised machine learning algorithm and therefore calibration samples are essential. First we define $(x_1, z_1), (x_2, z_2), \dots, (x_n, z_n)$ where $x_i \in \mathbb{R}^N$ is the feature vector and $z_i \in \mathbb{R}^1$ is the target output. Here, N is the dimension of the feature space and n denotes the number of samples. With ε -SV regression, the goal is to find a hyperplane $f(x)$ for the calibration data-set. The linear function $f(x)$ can be described as

$$y = f(x) = \langle \mathbf{w} \cdot \phi(\mathbf{x}) \rangle + b = \sum_{i=1}^n w_i \phi_i(x) + b, \quad (5.1)$$

where y is the predicted value, \mathbf{w} is the weight vector, ϕ is the nonlinear mapping function for re-projection, and b is the bias term. More details for SVR can be found in Smola and Schölkopf (2004). All bands are used as the feature vector in this study.

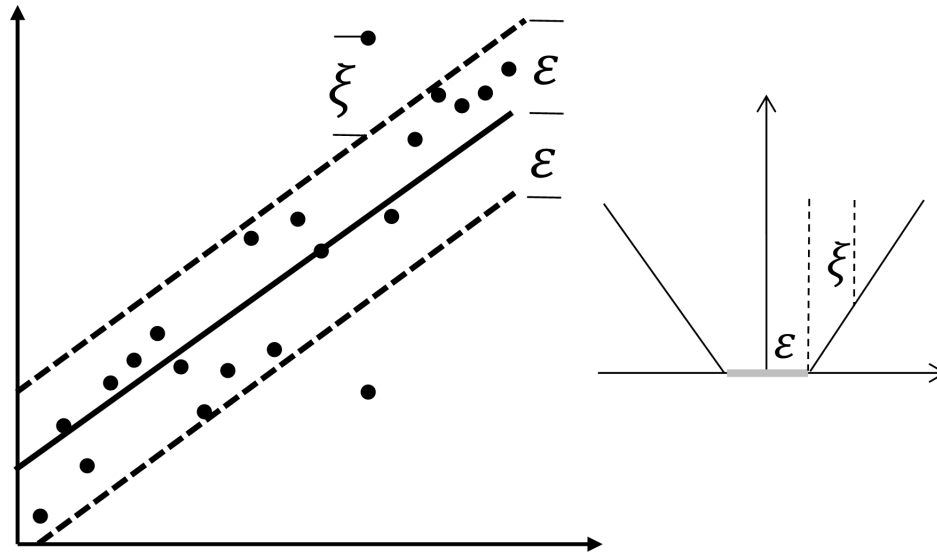


Figure 5.1 Slack variable ξ for soft-margin SVR; ε is the maximum allowed deviation.

Slack variables ξ_i and ξ_i^* are introduced to accommodate a soft-margin SVR (Smola and Schölkopf, 2004), see Figure 5.1. Under given parameters $C > 0$ and $\varepsilon > 0$, the standard

form of support vector regression is

$$\text{Min: } \frac{1}{2} \|\mathbf{w}\|^2 + C \sum_{i=1}^n (\xi_i + \xi_i^*) \text{ and} \quad (5.2)$$

$$\text{Subject to } \begin{cases} y_i - f(x_i) \leq \varepsilon + \xi_i^*; \\ f(x_i) - y_i \leq \varepsilon + \xi_i; \\ \xi_i, \xi_i^* \geq 0, i = 1, \dots, n, \end{cases} \quad (5.3)$$

here, C is the penalty parameter which tunes the tradeoff between the generalization of the functional relationship and the accuracy of the fitted hyperplane and ε is the maximum allowed deviation from the fitted hyperplane.

Kernel functions also introduced into SVR to accommodate nonlinear relationship in the linear formulation above. The kernel function projects the original feature space into a higher dimensional space that allows SVR to fit a hyperplane in a transformed feature space. There are many commonly used kernel functions including linear, polynomial, radial basis function (RBF) and hyperbolic tangent (Cui and Prasad, 2015). RBF is widely used and implemented here because of its good performance and smaller number of input parameters. The RBF kernel can be described as

$$K(x_i, x_j) = \exp(-\lambda \|x_i - x_j\|^2), \quad (5.4)$$

here, K denotes the kernel of two samples vectors x_i and x_j , and λ is related to the kernel width which requires tuning to achieve the best performance. The performance of SVR with the RBF kernel is highly correlated to the three input parameters: C , ε , and λ . To optimize the selection of these parameters, a general k-fold cross-validation method as well as a grid searching scheme are used (Ma *et al.*, 2010).

5.3 Results

We studied the accuracy of SVR for bathymetry retrieval using hyperspectral imagery, and compared its performance to the Optimal Band Ratio Analysis (OBRA) method (Legleiter *et al.*, 2009). To investigate the influence of calibration sample size, we increased the number of training samples from 100 to 500 in increments of 100, with the validation sample size fixed at 1000 to maintain the same comparison baseline. The calibration samples and validation samples were randomly selected from the *in-situ* measurements. The calibration samples were first used to estimate the OBRA parameters for water depth retrieval; the retrieved parameters were applied to estimate water depths at the validation sample locations. The same calibration samples were then fed into SVR for estimation of water depths; the retrieved water depths from both OBRA and SVR estimation were compared to the validation samples to calculate RMSE and R^2 .

In order to ensure consistent and stable results from both algorithms, the experiment was repeated 20 times. Also, to maintain a good model fit across all depths, the field measured water depths were first categorized into different depth bins with an interval of 0.1 m (see Figure 3.1.3(a) and Figure 3.1.3(b)). The random calibration samples were chosen to have the same relative percentage as the water depths distribution. The RMSE and R^2 between retrieved water depth and validation samples were calculated for each iteration and the average value was used for the result.

The RMSE for SVR decreases as the calibration sample size increases for the Snake River, while the R^2 also increases (see Figure 5.2). OBRA shows a fairly consistent performance with all training sample sizes. SVR outperforms OBRA with both lower RMSE and higher R^2 regardless of the training sample size. Both SVR and OBRA depth estimates degraded in the more turbid Blue/Colorado River as the overall RMSE is higher and R^2 for both algorithms are lower than the Snake River (see Figure 5.3). However, SVR still

significantly outperforms OBRA with a lower RMSE and higher R^2 value.

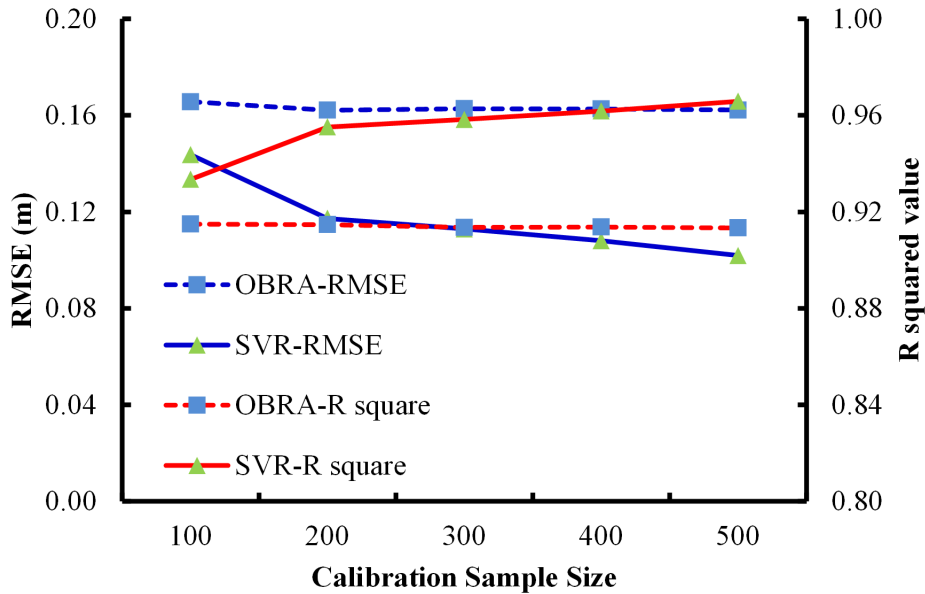


Figure 5.2 RMSE (m) and R^2 of OBRA and SVR for the Snake River water depths.

To further investigate the influence of water depth on the accuracy of depth determination for both OBRA and SVR, Figure 5.4 (Snake River) and Figure 5.5 (Blue/Colorado River) show the RMSE associated with varying water depths. The SVR results show significantly better RMSE for both shallower (<1.5 m) and deeper water (>2.5 m) for the Snake River, however, SVR results only show notable improvement in RMSE for deeper water (>1.5 m) in the Blue/Colorado River. RMSE increases for deeper water (>2 m for the Snake River, >1.5 m for the Blue/Colorado River) due to the saturation of the water column radiance over the bottom radiance signal in deeper water.

Finally, we briefly demonstrate the application of SVR for estimation of water turbidity from hyperspectral imagery. As the relationship between optical turbidity and observed spectrum remains unknown, a physical model to predict turbidity is difficult to establish. Therefore, we use the same k-fold cross validation and calibration-validation procedures to train a SVR model for extraction of water turbidity. From our *in-situ* turbidity observations we again varied the number of training samples from 100 to 500 in 100 sample increments,

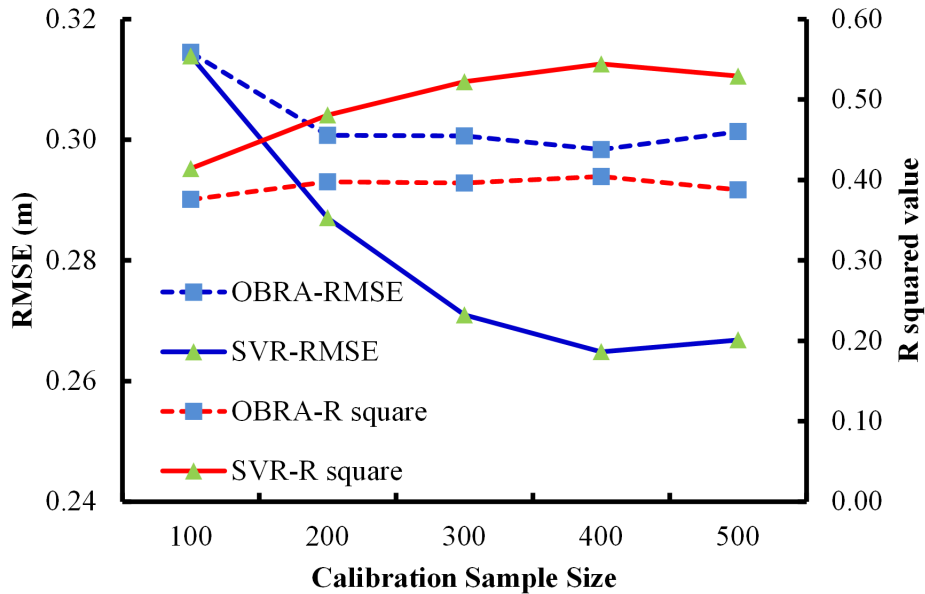


Figure 5.3 RMSE (m) and R^2 of OBRA and SVR for the Blue/Colorado River water depths.

and kept 1000 observed turbidity measurements as validation samples. Figure 5.6 shows that the RMSE between retrieved water turbidity decreases as the calibration sample size increases and is matched by a corresponding increase in R^2 .

5.4 Discussion

In this chapter, bathymetry extraction using SVR was proposed and applied to two hyperspectral imagery data-sets in two distinct fluvial environments. The retrieved water bathymetry was compared to a band ratio method. SVR incorporates all available spectral bands instead of only examining the ratio of a pair of bands. This is important, as all spectral bands were influenced by both benthic reflection and water attenuation. The band ratio method, OBRA, establishes a physical model and then uses an empirical method to find the optimal pair of spectral bands and neglects all other spectral channels. The physics-based water depth retrieval characteristic of OBRA makes it more generalized. The results also show that OBRA provides consistent results with relatively few training samples; however unfortunately its performance does not improve with an increase in the training sample

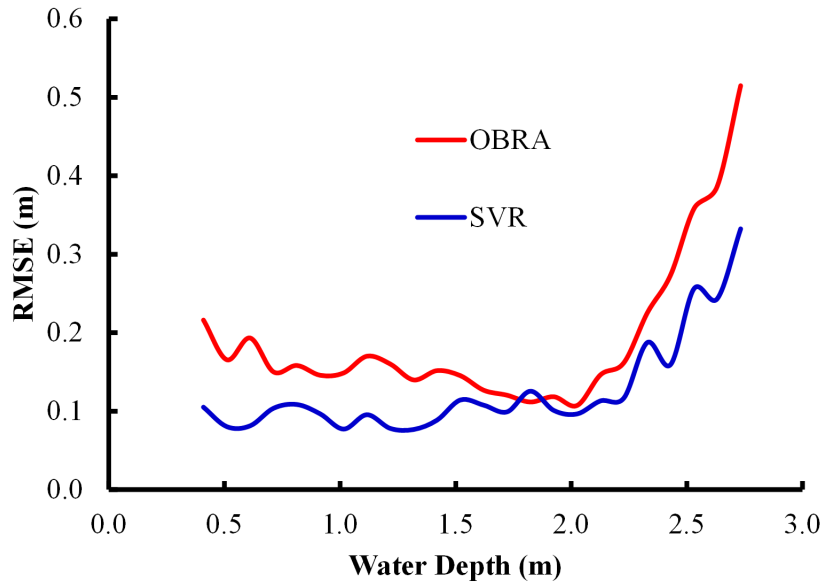


Figure 5.4 RMSE (m) with varying water depth of OBRA and SVR for the Snake River water depths.

size. As an empirical method, a band ratio method may not be optimal for the accurate estimation of bathymetry. In contrast SVR does not require a physical model to bridge the observed data with the desired product. The bathymetry retrieved from SVR outperforms OBRA with a lower RMSE and better R^2 for both the Snake and Blue/Colorado Rivers. The increase of training sample size was shown to improve SVR water depth estimation performance as well. Because no explicit relationship is required between the observations and the estimated physical parameters, SVR can be potentially extended to estimate other spectral based physical parameters. We also demonstrated how SVR can be used to estimate water turbidity, and the results show that hyperspectral imagery can be used to estimate turbidity with a low RMSE and high R^2 .

For depth determination, the RMSE for both SVR and OBRA degrade in deeper water (>2.0 m for the Snake River, >1.5 m for the Blue/Colorado River); this is caused by the nonlinear influence of the water column radiance in deeper water. However, for both rivers, SVR still outperforms OBRA, likely because it exploits all spectral radiance measurements.

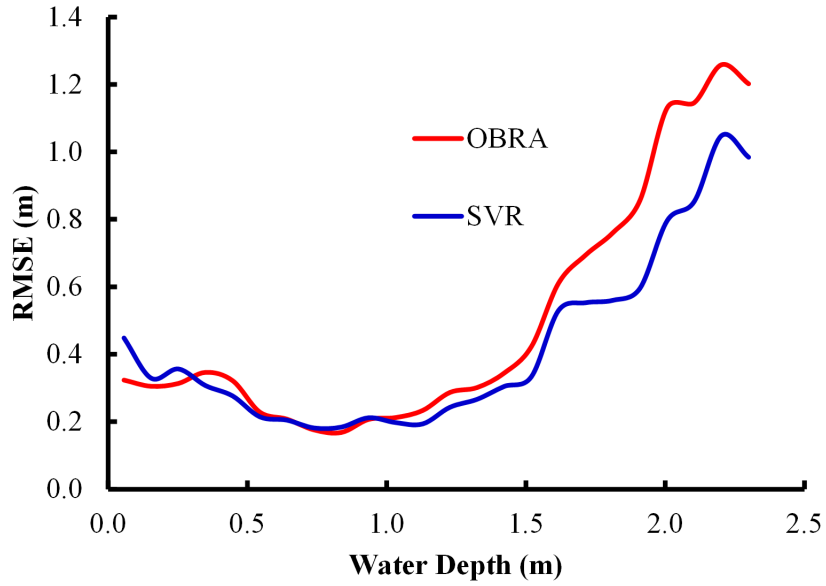


Figure 5.5 RMSE (m) with varying water depth of OBRA and SVR for the Blue/Colorado River water depths.

Both SVR and OBRA are less effective in the more turbid Blue/Colorado River (SVR has a R^2 of 0.5), however, the estimated water turbidity shows an obvious coherence with the observed radiance (SVR has a R^2 of 0.87 when estimating turbidity). This is due to the assumption that for spectral bathymetric retrieval the observed benthic radiance is the more dominant term compared to the water column radiance. However, the substantial turbidity of the Blue/Colorado River resulted in significant water column radiance that masked radiance from the benthic layer.

In summary, the proposed SVR method is effective at extracting water depths from hyperspectral imagery and outperforms the band ratio method. Due to its non-parametric formulation, SVR has also been successfully used to retrieve water turbidity from the observed hyperspectral imagery with high coherence with the physical measured water turbidity.

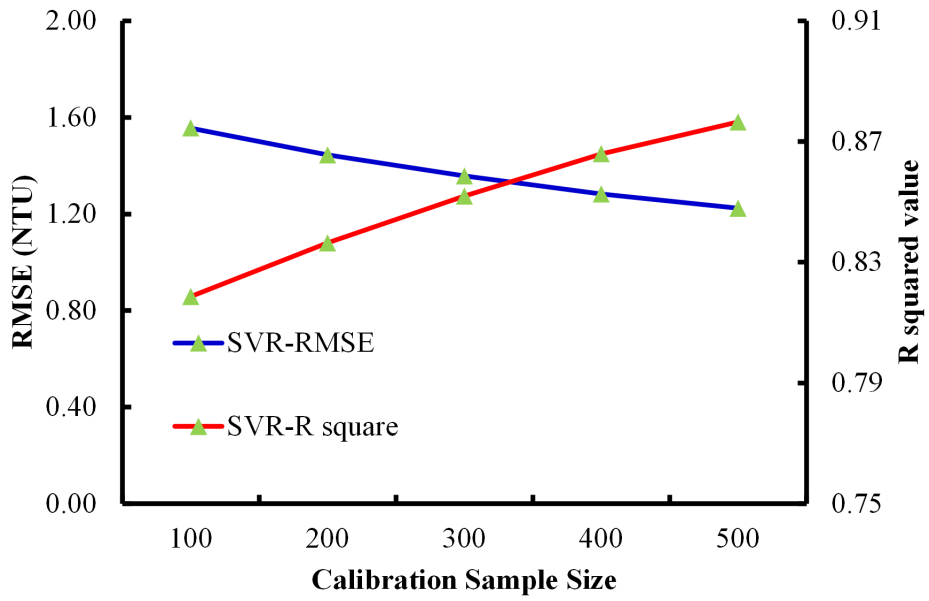


Figure 5.6 RMSE (NTU) and R^2 of OBRA and SVR for Blue/Colorado River water turbidity.

Chapter 6

Fusion of LiDAR Orthowaveforms and Hyperspectral Imagery for Shallow River Bathymetry and Turbidity Estimation

6.1 Overview

Chapter 2 introduced the background radiative transfer model for airborne bathymetric LiDAR in the water column, and Chapter 4 showed the comparison of several full waveform processing strategies. The conventional approach to utilizing full waveform LiDAR is to decompose the sampled waveform into multiple distinct returns to extract echo locations (Allouis *et al.*, 2010). Chapter 4 showed the benefits of using a representative single band full waveform LiDAR system for shallow river bathymetry. In addition to decomposing the full waveform for return locations, the shape of the return pulse energy can also be exploited because it contains information related to environmental parameters, e.g. (Parrish *et al.*, 2014). Rogers *et al.* (2015) also found good correlation between full waveform shape parameters and biophysical characteristics for a salt marsh area. However, the parameters derived from full waveform decomposition do not preserve all the information contained in the backscattered return profile because they are normally derived from a model based assumption of how the return energy should behave. Furthermore, the majority of recorded full waveforms have a varied and irregular sampling of look angles that make it difficult to apply conventional image processing algorithms for full waveform analysis. Hence, Park *et al.* (2014) proposed a voxelization of full waveform returns to transform them into an equivalent 3D image with subsequent detection of underwater environmental parameters using the generated 3D voxelized waveforms. The voxelized full waveform approximates a nadir laser pulse interaction with targets and facilitates the use of image processing strategies. A voxelized waveform was also shown to have potential for enhancement of land

cover classification (Wang *et al.*, 2015). However, the potential of voxelized full waveforms for shallow water bathymetry and estimation of water characteristics has not been explored.

In this chapter, we propose a new methodology to encapsulate the full waveform LiDAR return signal in a voxelized structure we refer to as an orthowaveform. To investigate the potential of orthowaveforms for bathymetry and turbidity estimation, we exploit the use of support vector regression (SVR), introduced in Chapter 5, as a supervised learning method to analyze the generated voxelized full waveforms. To validate the orthowaveform performance, we compare it against hyperspectral imagery (Chapter 5) and traditional full waveform LiDAR (Chapter 4). We also investigate the fusion of hyperspectral imagery and orthowaveforms for both bathymetry and water turbidity estimation.

6.2 Generation of Orthowaveforms

Because airborne LiDAR systems usually use both mirrors to direct laser pulses across the field of view of the scanner, and a forward tilt angle or a circular scan pattern to maintain a fixed incidence angle on the water surface, the return full waveform is generally along a slanted laser path. This variable slant direction makes the application of conventional image processing algorithms problematic. An orthorectified waveform (referred to here as an orthowaveform) would be preferable for extracting features using image processing techniques and for fusion with hyperspectral imagery. The concept of voxelizing an irregular point cloud has been used previously in topographic LiDAR studies to determine structural characteristics of forests to estimate biomass parameters (Jung and Crawford, 2012), and to fuse hyperspectral imagery and LiDAR for land cover classification (Wang and Glennie, 2015) To illustrate the voxelization process used in this study, Figure 6.1 conceptually shows the generation of orthowaveforms from slanted full waveforms. Each waveform amplitude in the full waveform is georeferenced in space and the ground and water surfaces

are used to convert all waveform samples to an equivalent above ground height (AGH). The ground layer (DTM) is extracted from the discrete point cloud using a classification algorithm in the Terrascan software package similar to the approach described in Axelsson (2000). The benthic portion of the waveform will reside under the 0 m (AGH) surface while features such as vegetation and buildings will be above it.

To produce a 3D image, a gridding method, referred to as voxelization, was applied to the irregularly distributed waveform samples (Park *et al.*, 2014). The pixel size and vertical resolution of the voxels are critical for generating orthowaveforms as larger pixel sizes and vertical resolution results in more samples belonging to the same voxel. For our purpose, to accommodate the subsequent comparison with hyperspectral imagery and fusion strategies, the generated orthowaveforms have the same spatial pixel size as the hyperspectral imagery (see Table 3.1). The vertical resolution was set as 0.2 m; this is slightly larger than the waveform sample resolution (1 GHz for full waveform digitization). The mean amplitude value of all points falling in one voxel is used as the approximate voxel amplitude due to the relatively low water depths (Figure 3.1.3 (a) and (b)) and small scan angles (see Table 3.1). The voxelization process averages nearby full waveforms and thus the generated orthowaveforms approximate the geometric and spectral information contained in the waveform assuming homogeneous characteristics of the water at the pixel scale.

Figure 6.2 shows the hyperspectral imagery and generated orthowaveform 3D cube for the Snake River. The spatial resolution of the orthowaveforms is 0.6 m and vertical resolution is 0.2 m; only the portion of AGH less than 0 m was used for subsequent analysis. The generated orthowaveform has texture similar to hyperspectral imagery and the river channel is clearly observable feature with the dark pixels denoting the deeper portion of the channel.

Figure 6.3 shows the average hyperspectral spectrum and orthowaveform for varying

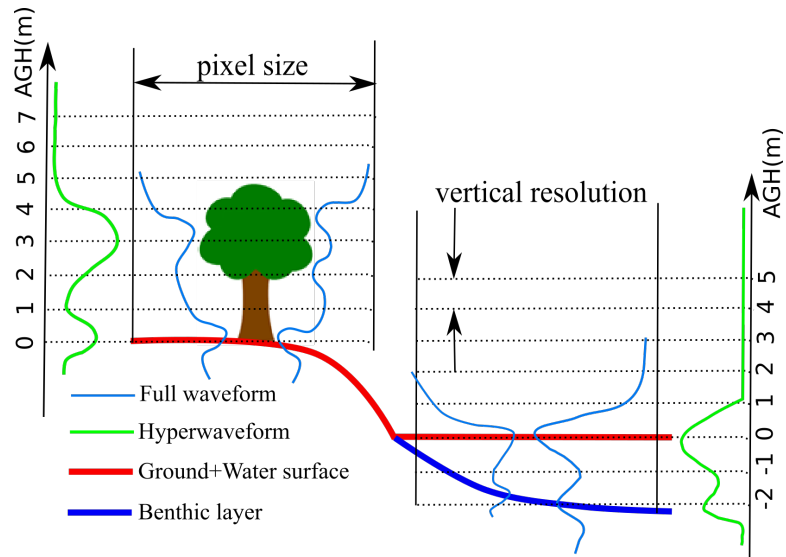


Figure 6.1 Schematic generation of orthowaveform (AGH: Above Ground Height).

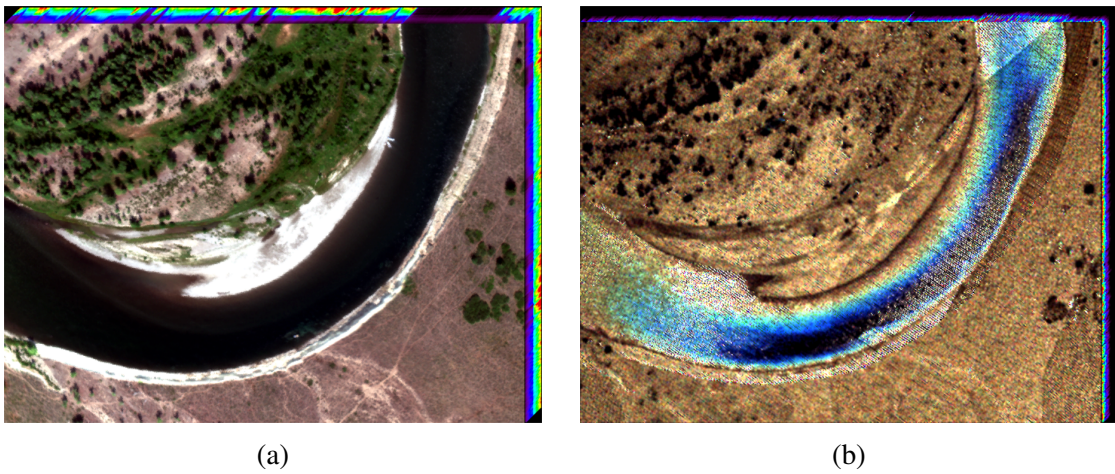


Figure 6.2 (a) Hyperspectral imagery 3D cube for the Snake River using true RGB; (b) generated orthowaveform 3D cube for the Snake River with three bands (R:-1.0 m, G: -1.4 m, B: -1.8 m).

water depth measurements. Both hyperspectral and orthowaveform features vary with water depth. The visible spectrum radiance (500 nm – 700 nm) decreases with an increase of water depth due to more attenuation in the water column (Figure 6.3(a)). The average LiDAR intensity at 2.0 m has more backscatter energy from the water column due to the presence of more specular reflection (see Figure 6.3(b)).

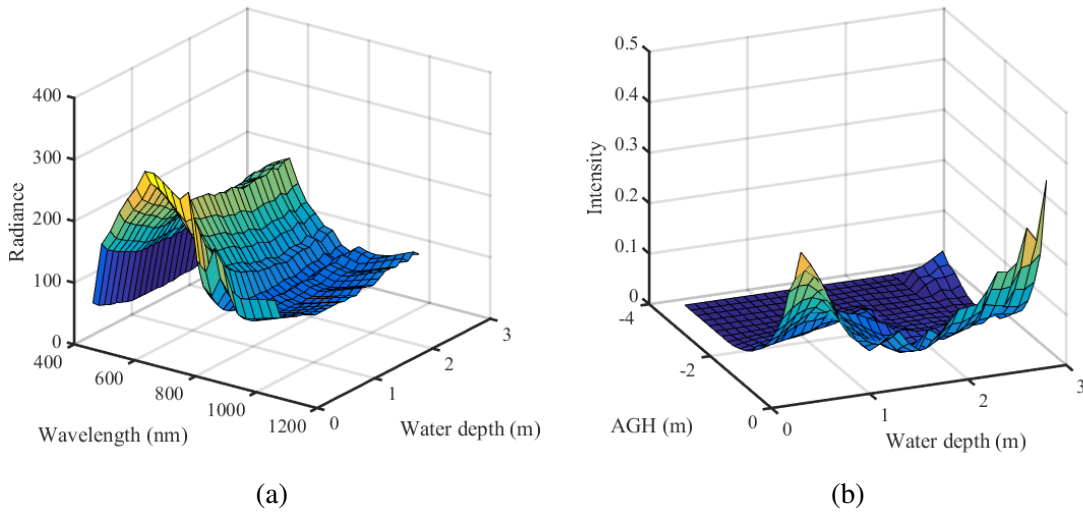
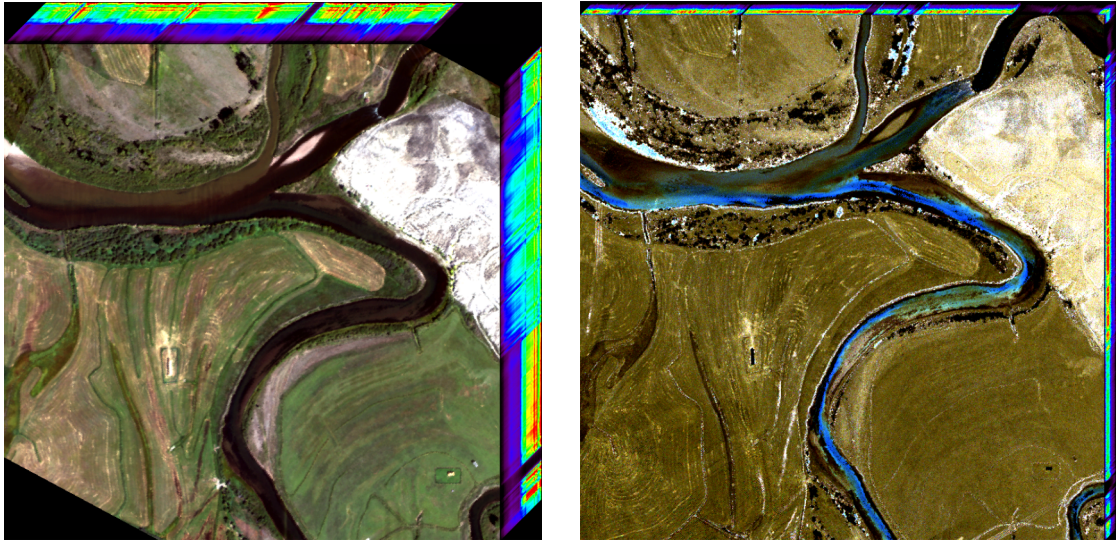


Figure 6.3 (a) Average hyperspectral spectrum with varying water depth for the Snake River; (b) average orthowaveform with varying water depth for the Snake River.

Figure 6.4 shows the hyperspectral imagery and generated orthowaveform 3D cube for the Blue/Colorado River. The spatial resolution of the orthowaveforms is 1.2 m and the vertical resolution is set as 0.2 m; only the portion of AGH less than 0 m is extracted for subsequent analysis. The channel is also clearly observable with dark blue pixels denoting the deeper channel.

Figure 6.5 shows the average hyperspectral spectrum and orthowaveform features for varying water depth measurements. The average features are more complicated due to the varying turbidity present in the Blue/Colorado River, but the features clearly vary with water depth. Also, Figure 6.6 shows the average hyperspectral spectrum and orthowaveform



(a)

(b)

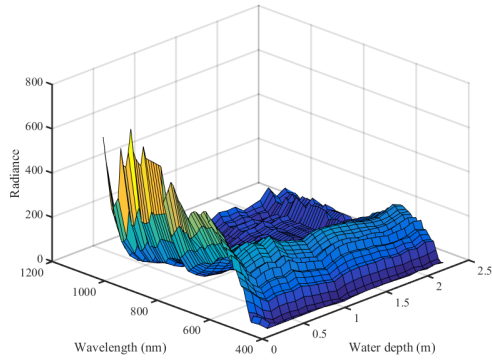
Figure 6.4 (a) Hyperspectral imagery 3D cube for the Blue/Colorado River with true RGB; (b) generated orthowaveform 3D cube for the Blue/Colorado River with three bands (R:-1.2 m, G:-1.6 m, B:-2.0 m).

features for varying water turbidity measurements. Hyperspectral spectrum shows increasing observed radiance and orthowaveform displays more energy near 0 m which indicates significant surface scattering.

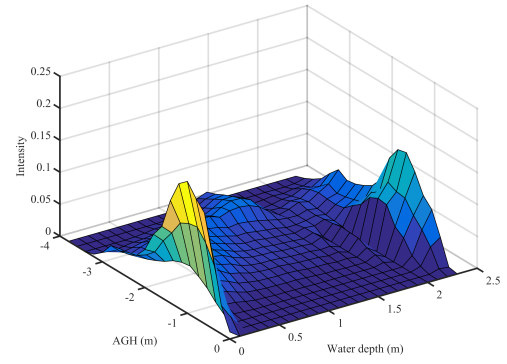
To evaluate the performance of both orthowaveform LiDAR and hyperspectral imagery for prediction of bathymetry and turbidity, root mean square error (RMSE) and R-squared (R^2) values are used to compare the predicted values with in-situ measured reference data. The field measured reference data-set was gridded using averaged values to ensure it was at the same spatial resolution as the hyperspectral imagery and generated orthowaveforms.

6.3 Experimental Setup and Results

To investigate the capability of orthowaveforms and their fusion with hyperspectral imagery, each individual data-set was first regressed using SVR and then the orthowaveforms were also concatenated to the hyperspectral imagery to form a fused feature set. The

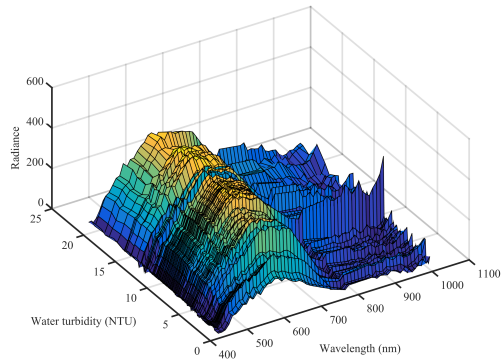


(a)

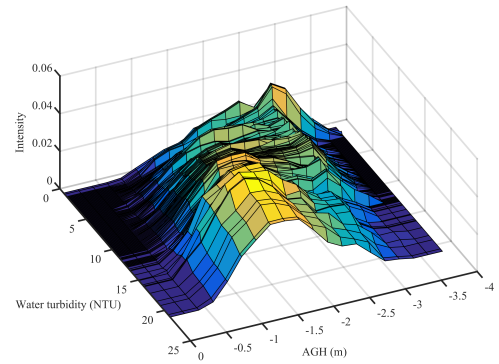


(b)

Figure 6.5 (a) Average hyperspectral spectrum with varying water depth for the Blue/Colorado River; (b) average orthowaveform with varying water depth for the Blue/Colorado River.



(a)



(b)

Figure 6.6 (a) Average hyperspectral spectrum with varying water turbidity for the Blue/Colorado River; (b) average orthowaveform with varying water turbidity for the Blue/Colorado River.

calibration sample size was incrementally increased from 100 to 500 with an interval of 100 while the validation sample size was fixed at 1000. Both the calibration and validation samples were selected through random sampling. A 5-fold cross validation scheme was implemented to search for the optimal SVR parameters through a grid search. The same calibration and validation data-sets were applied for each individual feature (hyperspectral imagery and orthowaveforms) and the fused feature set. Each experiment was repeated 20 times and the average RMSE and R^2 were calculated; the standard deviation calculated from the 20 iterations for each experiment are also reported.

6.3.1 Snake River Bathymetry Estimation

Table 6.1 shows the results for the Snake River bathymetry estimation and Figure 6.7 shows the generated water depth maps. Each individual data-set shows improved performance with increased calibration data-set size. The best average RMSE for hyperspectral imagery is 11 cm with 3 cm of standard deviation, and an R^2 of 0.96 with a standard deviation of 0.03; the best average RMSE for orthowaveforms is 17 cm with a 1 cm standard deviation, and an R^2 of 0.91 with standard deviation of 0.01. The orthowaveforms showed acceptable accuracy for water depth prediction but were outperformed by hyperspectral imagery. However, the standard deviation of the orthowaveforms is lower than that of the hyperspectral imagery, indicating that the orthowaveforms are a more consistent measurement of depth for the Snake River.

The fused feature set showed the best performance with an average RMSE of 10 cm, a standard deviation of 1 cm and an R^2 of 0.96 with a standard deviation of 0.01. Comparing the fusion results to hyperspectral and orthowaveforms respectively, the average RMSE and R^2 are similar to that of the hyperspectral imagery, which showed superior performance, but the standard deviation of both the RMSE and R^2 are smaller than the hyperspectral imagery alone which indicates that the fused feature set is more stable than hyperspectral

Table 6.1 Snake River SVR bathymetry results for hyperspectral imagery, orthowaveforms and the fused feature set. (standard deviation in brackets, κ : calibration sample size)

κ	Hyperspectral		Orthowaveforms		Fusion	
	RMSE(m)	R^2	RMSE(m)	R^2	RMSE(m)	R^2
100	0.16(0.07)	0.91(0.08)	0.21(0.02)	0.86(0.03)	0.13(0.01)	0.94(0.01)
200	0.16(0.07)	0.91(0.07)	0.18(0.01)	0.89(0.01)	0.12(0.01)	0.96(0.01)
300	0.12(0.03)	0.95(0.02)	0.18(0.01)	0.90(0.01)	0.11(0.01)	0.96(0.01)
400	0.12(0.02)	0.95(0.02)	0.17(0.01)	0.90(0.01)	0.11(0.01)	0.96(0.00)
500	0.11(0.03)	0.96(0.03)	0.17(0.01)	0.91(0.01)	0.10(0.01)	0.96(0.01)

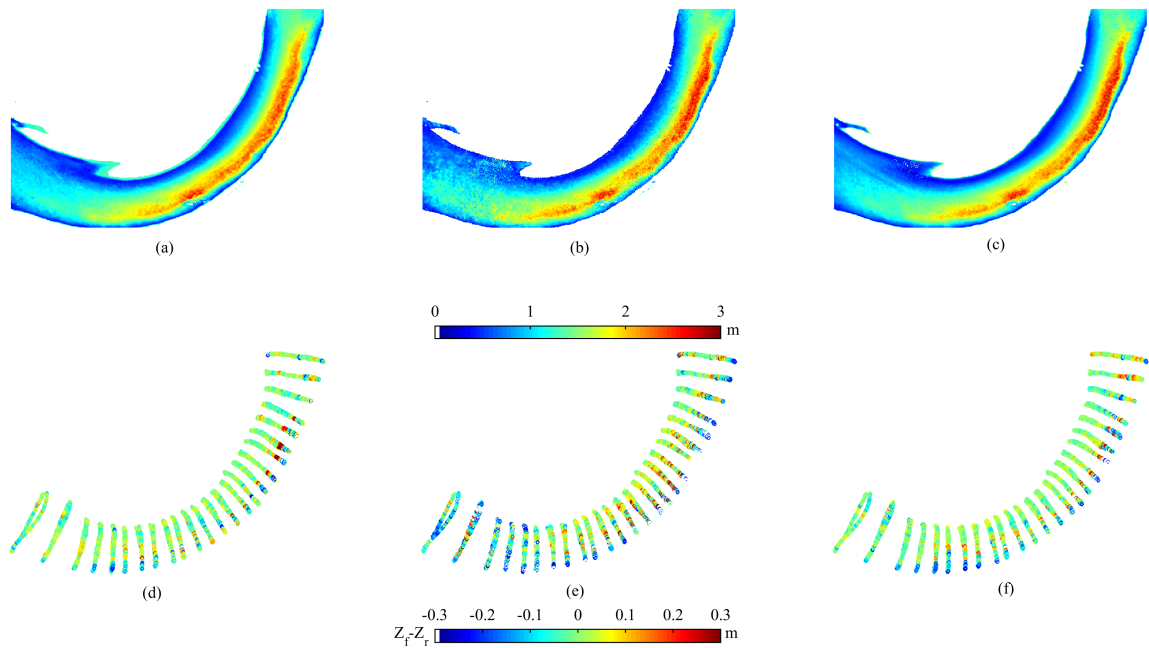


Figure 6.7 Water depth maps: (a) hyperspectral imagery; (b) orthowaveforms; (c) fusion. Water depth error: (d) hyperspectral imagery; (e) orthowaveforms; (f) fusion (Z_f : ADCP water depth, Z_r : remotely sensed water depth).

imagery for water depth estimation.

To further investigate bathymetric estimation for the Snake River, Figure 6.8 shows the distribution of RMSE for varying water depths. The RMSE increases dramatically after the water is deeper than 2 m, likely because of the saturation of the optical radiance signal in deeper water such that further increases in depth produce less significant changes (Legleiter *et al.*, 2015). Hyperspectral imagery performs better than the generated orthowaveforms for most depth ranges, and the fused feature performance is similar to hyperspectral imagery alone, but does improve the spike in hyperspectral imagery RMSE at 0.9 m water depth.

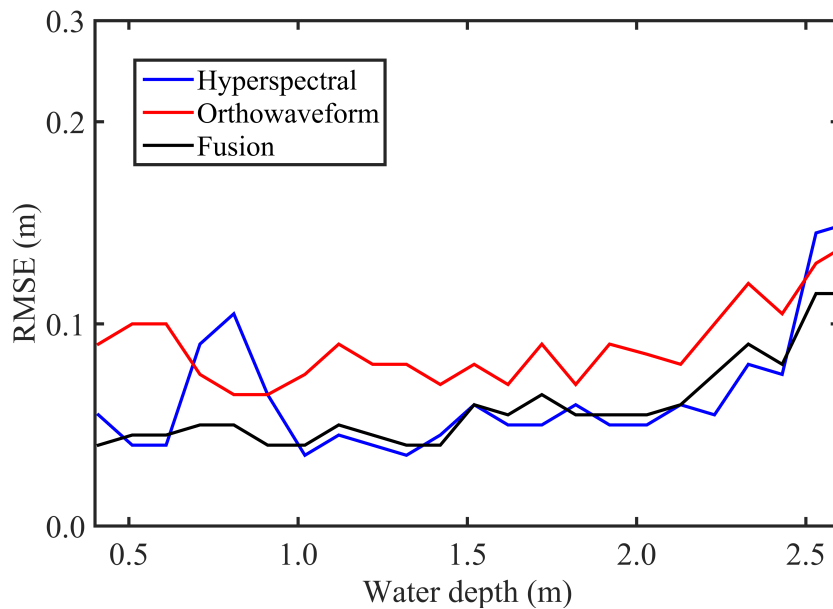


Figure 6.8 RMSE distribution of water depths with varying water depths for the Snake River.

6.3.2 Blue/Colorado River Bathymetry Estimation

The Blue/Colorado River is more turbid than the Snake River and the overall bathymetric performance degrades due to excessive water column radiance. Table 6.2 shows the results for the Blue/Colorado River bathymetry estimation and Figure 6.9 shows the

retrieval of water depths. Again each individual feature retrieval shows improved performance with an increase of calibration sample size. The best performance for hyperspectral imagery is an average RMSE of 26 cm with a standard deviation of 1 cm and an average R^2 of 0.55 with a standard deviation of 0.03. The best orthowaveforms performance is an average RMSE of 21 cm with a standard deviation of 2 cm and the best average R^2 is 0.70 with a standard deviation of 0.04. The orthowaveforms show superior depth retrieval in the more turbid water of the Blue/Colorado River because they are less affected by water turbidity. However, the higher standard deviation of the orthowaveforms indicates that water turbidity still has a significant influence on the accuracy of depth retrieval.

Table 6.2 Blue/Colorado River bathymetry results for hyperspectral imagery, orthowaveforms and fused feature sets using SVR. (standard deviation in brackets, κ : calibration sample size)

κ	Hyperspectral		Orthowaveforms		Fusion	
	RMSE(m)	R^2	RMSE(m)	R^2	RMSE(m)	R^2
100	0.33(0.03)	0.40(0.09)	0.25(0.03)	0.60(0.07)	0.25(0.02)	0.60(0.04)
200	0.28(0.02)	0.50(0.05)	0.23(0.03)	0.66(0.06)	0.23(0.02)	0.65(0.04)
300	0.27(0.02)	0.52(0.05)	0.21(0.01)	0.70(0.03)	0.22(0.01)	0.69(0.03)
400	0.26(0.01)	0.55(0.03)	0.21(0.01)	0.71(0.02)	0.21(0.01)	0.70(0.03)
500	0.26(0.01)	0.55(0.04)	0.21(0.02)	0.70(0.04)	0.21(0.01)	0.71(0.03)

The fusion of the imagery and orthowaveforms feature sets yields the best average RMSE of 21 cm with a standard deviation of 1 cm and the best average R^2 of 0.71 with a standard deviation of 0.03. A marginal improvement is found with fusion (compared to orthowaveforms alone), however, the lower standard deviation of the RMSE and R^2 for the fused feature set results indicate that the results are more consistent.

Figure 6.10 shows the RMSE distribution of depth retrieval error with varying water depths for the Blue/Colorado River. RMSE increases significantly for water depths larger than 1.5 m likely because the observations are approaching the maximum detectable depth (see Figure 6 in Legleiter *et al.* (2015)). Overall, the fused feature set shows similar performance to the orthowaveforms.

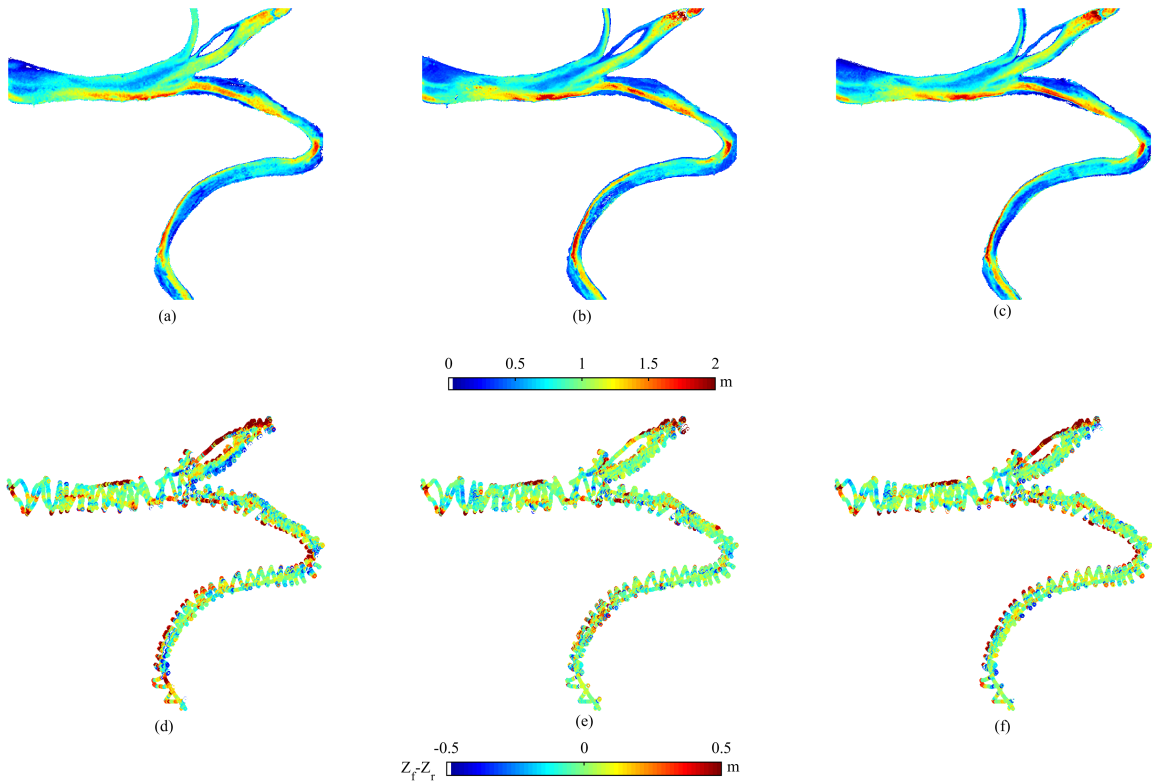


Figure 6.9 Water depth maps : (a) hyperspectral imagery; (b) orthowaveforms; (c) fusion. Water depth error: (d) hyperspectral imagery; (e) orthowaveforms; (f) fusion (Z_f : ADCP water depth, Z_r : remotely sensed water depth).

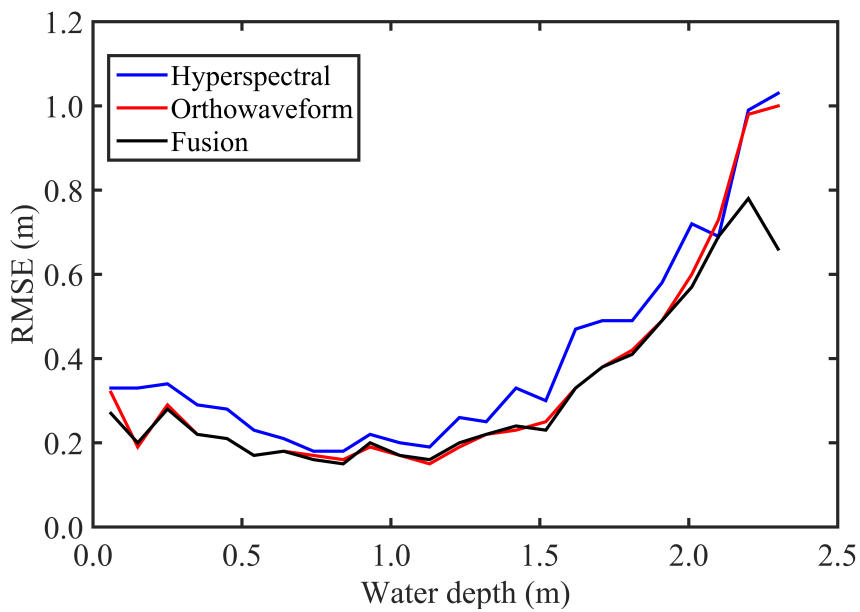


Figure 6.10 RMSE distribution of water depth errors with varying water depths for the Blue/Colorado River.

6.3.3 Comparison of full waveform and orthowaveform for bathymetry

According to chapter 4, full waveform bathymetric LiDAR processing significantly improves water depth estimation compared to depths estimated solely from discrete bathymetric LiDAR point clouds. Therefore, it is reasonable to compare the full waveform derived water depths to water depths retrieved from the orthowaveforms. Ideally, if the full waveform processing algorithms were correctly modeling the return pulse energy we would expect similar performance between the use of orthowaveforms and full waveform processing. The depth estimates produced with orthowaveforms are compared to the full waveform LiDAR processing results presented in Table 4.1 and Table 4.3, which presented a detailed analysis of full waveform LiDAR processing for the sample data-sets captured over the Snake and Blue/Colorado Rivers. The best full waveform LiDAR processing results (see Table 4.1 and Table 4.3 in chapter 4) are provided in Table 6.3 for comparison with the orthowaveform bathymetry estimates.

Table 6.3 Comparison of full waveform to orthowaveform derived water depths for both the Snake and Blue/Colorado River.

	Snake River		Blue/Colorado River	
	Full waveform	Orthowaveform	Full waveform	Orthowaveform
Mean ($Z_f - Z_r$, m)	-0.13	-0.04	-0.16	-0.01
Std ($Z_f - Z_r$, m)	0.13	0.16	0.27	0.20
Slope	1.08	0.93	0.85	0.84
Intercept	0.05	0.12	0.28	0.15
R ²	0.92	0.92	0.57	0.73

* Z_f is the field measurement, Z_r is LiDAR derived water depth, Std: standard deviation

For the clear water of the Snake River, the bathymetry estimates from full waveform LiDAR shows similar performance to the orthowaveforms, but with a slightly smaller standard deviation. Both bathymetry estimates show strong correlation to the field measured water depths. However, for the more turbid water of the Blue/Colorado River study site, the bathymetry estimates from the orthowaveforms show significantly better performance than the bathymetry estimates from full waveform processing. The standard deviation is

reduced to 20 cm from 27 cm while the R^2 increases to 0.73 from 0.57. This indicates that the physically based full waveform processing algorithm needs to more effectively remove the effect of water column on the full waveform shape to accurately estimate depths. The superior performance of the orthowaveforms indicates that the water column effect is indeed encapsulated in the LiDAR return pulse profiles, and that it can be used to more accurately estimate bathymetry.

6.3.4 Blue/Colorado River Turbidity Estimation

Theoretically, the observed hyperspectral imagery and orthowaveforms both contain information pertaining to water column characteristics. However, it is difficult to explicitly define a physical model to relate the remote sensing observations to field measured turbidity. The availability of field measured water turbidity for the Blue/Colorado River enables us to investigate the applicability of both the individual and fused features for prediction of turbidity using a nonparametric SVR approach. Table 6.4 shows the results for turbidity estimation for the Blue/Colorado River and Figure 6.11 shows the retrieval of water turbidity. Similar to the bathymetry estimation results, the average RMSE and R^2 of turbidity estimation are improved with an increase in the calibration sample size; hyperspectral imagery yields the best RMSE of 1.20 NTU with a R^2 of 0.88; orthowaveforms yields a best RMSE of 1.32 NTU with a R^2 of 0.86. Both hyperspectral and orthowaveforms show similar performance indicating that the hyperspectral and orthowaveforms observe similar water column characteristics for the Blue/Colorado River. Comparing Table 6.4 to Table 6.2, we can conclude that orthowaveforms are more applicable to water depth estimation than hyperspectral imagery for the turbid Blue/Colorado River, however, the hyperspectral imagery performs better for water turbidity estimation than orthowaveforms with a higher R^2 relating to turbidity. This again implies that bathymetric LiDAR is less affected by water turbidity, but also suggests that the additional observed spectral channels from

hyperspectral imagery are better able to estimate turbidity than the single spectral band reflectance of the bathymetric LiDAR. However, both hyperspectral imagery and orthowaveforms show stronger correlation to water turbidity than water depth (i.e., higher R^2 value) indicating that the excessive water column reflectance overwhelmed the benthic return for the Blue/Colorado River.

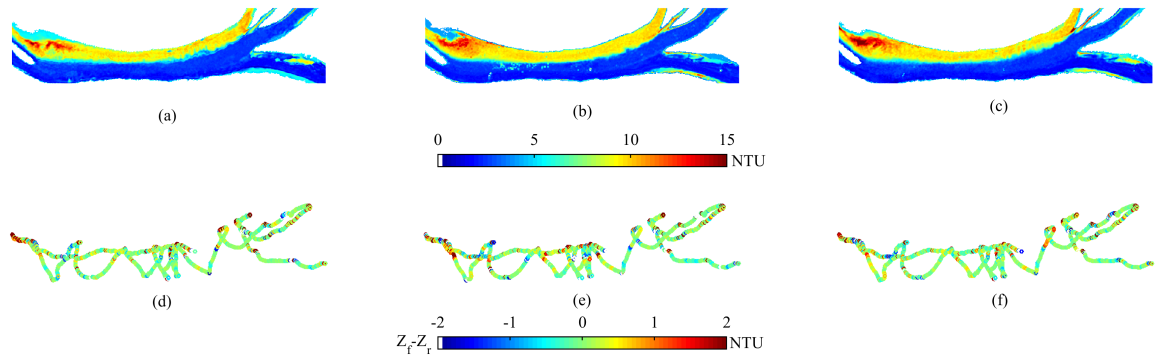


Figure 6.11 Water turbidity maps: (a) hyperspectral imagery; (b) orthowaveforms; (c) fusion. Water turbidity error: (d) hyperspectral imagery; (e) orthowaveforms; (f) fusion (Z_f : field measured water turbidity, Z_r : remotely sensed water turbidity).

Table 6.4 Blue/Colorado River turbidity results for hyperspectral imagery, orthowaveforms and a fused feature set using SVR.(standard deviation in brackets, κ : calibration sample size)

κ	Hyperspectral		Orthowaveforms		Fusion	
	RMSE(NTU)	R^2	RMSE(NTU)	R^2	RMSE(NTU)	R^2
100	1.59(0.22)	0.81(0.04)	1.52(0.12)	0.82(0.02)	1.45(0.13)	0.84(0.02)
200	1.42(0.13)	0.84(0.03)	1.50(0.10)	0.82(0.02)	1.37(0.11)	0.85(0.02)
300	1.31(0.07)	0.86(0.01)	1.41(0.09)	0.84(0.02)	1.23(0.05)	0.88(0.01)
400	1.25(0.08)	0.87(0.02)	1.38(0.06)	0.84(0.01)	1.21(0.05)	0.88(0.01)
500	1.20(0.08)	0.88(0.01)	1.32(0.08)	0.86(0.02)	1.16(0.08)	0.89(0.01)

The fused feature set shows an optimal performance of 1.16 NTU RMSE with a R^2 of 0.89. The fusion has marginally improved the performance compared to using either the hyperspectral imagery or orthowaveforms alone; the standard deviation of the RMSE and R^2 are better for the fused data-set and therefore give a more consistent turbidity prediction.

Figure 6.12 shows the RMSE distribution of turbidity estimation error with varying

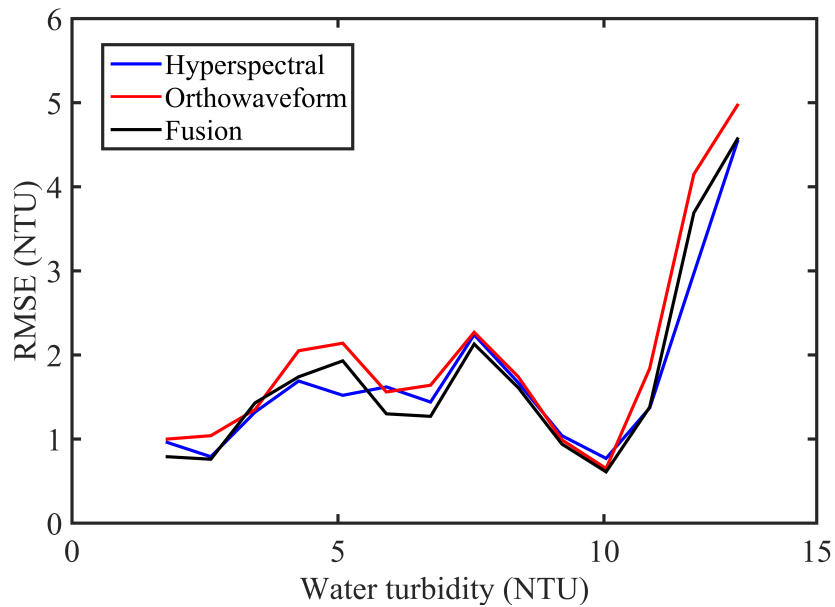


Figure 6.12 RMSE distribution of water turbidity errors with varying water turbidity for the Blue/Colorado River.

water turbidity for the Blue/Colorado River for each observation type. The RMSE of the retrieved water turbidity is lowest, in the areas where the training samples had sufficient observed turbidity (i.e., at approximately 2 and 10 NTU). The actual turbidity measurements showed a bimodal distribution (see Figure 3.1.3(c)), and therefore limited training samples were available outside the bands at ~ 2 and 10 NTU.

6.4 Discussion

Orthowaveforms generated from full waveform bathymetric LiDAR contain both the shape and amplitude information of the reflected energy within the laser cone of diffraction, and SVR is an effective method to bridge this observation to physical water depths and turbidity. Orthowaveforms did not perform as well as hyperspectral imagery for water depth retrieval in the clear water of the Snake River, but outperformed hyperspectral imagery in the more turbid water of the Blue/Colorado River study site. The water depths retrieved

from orthowaveforms were similar to water depths retrieved from full waveform bathymetric LiDAR processing for the Snake River, however, the water depths retrieved from orthowaveforms were significantly better than water depths retrieved from full waveform processing for the Blue/Colorado River. The comparison of the full waveform processing results and the orthowaveform depth determination clearly showed that for more turbid water, the encapsulation of the entire waveform shape better estimates depths than determination of return locations from full waveform processing. This suggests that for turbid water, full waveform LiDAR processing needs to be extended to properly model the non-Gaussian LiDAR energy returned from the water column. There has been some initial work on this using simulated data (Abady *et al.*, 2014), but detailed studies using actual bathymetric LiDAR data-sets are required in order to develop a physical model for the return energy from the water column. The regression between generated orthowaveforms with water turbidity shows its capability to derive additional environmental characteristics. The promising capability of machine learning coupled with orthowaveforms suggests that this approach could be extended to estimate other biophysical and ecological parameters, which currently can be estimated through full waveform analysis (Rogers *et al.*, 2015).

In contrast to conventional processing strategies for bathymetry from hyperspectral imagery, the SVR approach used in this study is purely data driven. As a supervised learning method, calibration samples are necessary to connect the observations with the results; the improvement of prediction with an increase of calibration sample size indicates that better regression can be found with more calibration samples if we can neglect the increased computational load. However, the optimal number of field measurements as training samples is still unknown, and is likely highly correlated to the variability in water depths, turbidity and bottom reflectivity found in the fluvial environment under study. The projection of features into a high-dimensional mathematical space and the fitting with a hyperplane gives remote sensing users a new tool for data analysis and interpretation. However, the

one obvious disadvantage of using SVR is that accurate field data is required to build the mathematical models, whereas the primary motivation for using remote sensing is to directly quantify physical and environmental characteristics remotely. Thus the collection of field measurements is not always feasible, especially for non-accessible areas, where temporal changes in observational parameters and difficult measurement environments are present. Even for accessible sites, the requirement of excessive field measurements can limit the applicability of using SVR, and therefore, it is also necessary to develop strategies with fewer field observations or which only require remotely sensed data. The success of combining hydraulic principles with a linear relationship between image and water depth to derive river bathymetry without field data demonstrates outstanding potential in fluvial remote sensing studies (Legleiter, 2015).

Both the orthowaveform and hyperspectral imagery showed better correlation to water turbidity than water depth for the Blue/Colorado River, a consequence of a major limitation of optical remote sensing: returned radiance from the benthic layer is required for accurate depth estimation. Pre-flight planning for data collection is critical to acquire the desired quality of data, and to ensure that the acquisition is done under ideal conditions (e.g. low water flow and low turbidity). However, overall the orthowaveforms show better correlation to water depth than hyperspectral imagery, while hyperspectral imagery shows better connection to water turbidity than the orthowaveforms. This indicates that active optical airborne bathymetric LiDAR is more tolerant to water turbidity.

Data fusion on the other hand is also currently a hot topic for the remote sensing community. As Hossain *et al.* (2014) concluded, there is no single remote sensing strategy that is suitable for all remote sensing tasks, and therefore an optimal combination of all available observations has the potential to improve the quantitative determination of physical parameters from remote observations. Although the fused feature sets in this study only marginally improved estimates for both clear and turbid water, it did stabilize the overall

solution by yielding smaller standard deviation (i.e., more consistent results). This would suggest that additional analysis of fused feature sets, including consideration of the physical radiative transfer models, may allow additional improvement to the fused observations.

Chapter 7

Radiative Transfer Modeling of Remote Sensing Observations to Determine Shallow Water Characteristics

7.1 Overview

Deriving shallow water bathymetry from hyperspectral imagery has been shown to be effective using the statistical methods presented in chapter 5 and 6 with known field measured water depths used as training samples. The correlation of water depths and observed spectrum is statistically established and applied to predict shallow water bathymetry. The implementation of statistical methods is straightforward and the accuracy is significant with invariant water constituents and substrate types. However, empirical or statistical methods also have substantial limitations. First, field measured water depths are not always available, especially for non-accessible areas, which make it impossible to establish the underlying statistical relationships. Second, the calibrated model is specific to each study case and is not applicable to other study areas or sensor types. Furthermore, varying water column characteristics and substrate types within a study area can affect the efficiency and accuracy of empirical methods, as previously demonstrated in (Philpot, 1989; Legleiter *et al.*, 2015).

A spectral model that considers all parameters simultaneously and analytically is a promising approach to determine shallow water column constituents and estimate bathymetry. Water column constituents contribute to observed remote sensing reflectance and have been extracted using different empirical band ratio or analytical methods (Gitelson *et al.*, 2009; Cannizzaro and Carder, 2006; O'Reilly *et al.*, 1998; Brando and Dekker, 2003; Jay and Guillaume, 2014). The contributions of water column characteristics and benthic layer bathymetry to remote sensing reflectance are correlated. The water column contributes negligible reflectance in shallow water and the benthic layer contributes an insignificant

amount in optically deep water (Cannizzaro and Carder, 2006). Because of this interdependence the optical radiative transfer process for shallow water environments is complicated.

HydroLight is a numerical radiative transfer model that solves for a water radiance distribution and derives a variety of water column related quantities. With numerically developed bi-optical models and input baseline absorbing and scattering properties, it is used to synthesize modeled spectra to validate remote sensing observations of the ocean (Mobley, 1994). Mobley *et al.* (2005) constructed a database of remote sensing reflectance spectra corresponding to various water column constituent concentrations and bottom reflectance spectra. This forward model compares the observed spectra with the database and solves for the water column characteristics and bathymetry simultaneously. However, a relatively large amount of simulated spectra are required to fully cover varying water column and benthic conditions to retrieve constituent concentrations with acceptable accuracy. As an alternative, Lee *et al.* (1998) developed a semi-analytical model that has been widely used to estimate bathymetry and water column constituents in shallow water. The semi-analytical model generally uses three water constituent concentration parameters (chlorophyll (CHL), colored dissolved organic matter (CDOM) and non-algal particles (NAP)) along with the water depth to calculate the water-leaving reflectance. Since each parameter has a unique effect on the water leaving reflectance a retrieval of these parameters is possible. The efficiency and accuracy of this method has been previously reported in many studies, e.g., (Dekker *et al.*, 2011; Brando and Dekker, 2003; Brando *et al.*, 2009; Lee *et al.*, 1999; Torres-Madronero *et al.*, 2009; Jay and Guillaume, 2014, 2016). The model uses an inversion technique to solve for both water column characteristics and bathymetry simultaneously by minimizing the difference between modeled and observed spectra. The method has also been shown to outperform empirical algorithms for some applications (Dekker *et al.*, 2011).

In chapter 5 and 6, support vector regression (SVR) was shown to be effective for water bathymetry and turbidity retrieval. SVR is a supervised method that requires calibration samples to learn the pattern in the observed spectra. The forward model proposed by Lee *et al.* (1998) and the HydroLight software; however, enable us to artificially create calibration samples. By assuming that we can generate accurate artificial spectra as training samples we can then investigate SVR performance in deriving water column constituents and bathymetry from hyperspectral imagery. Therefore, we evaluate the semi-analytical model and propose a forward model based SVR approach to extract water column constituent concentrations and shallow water bathymetry. The comparison of these two methods and the conventional SVR method with LiDAR bathymetry samples are given in this chapter. Fusion is also performed for both inversion and model based SVR method to investigate its effect on the estimates.

7.2 Methods

7.2.1 LiDAR Bathymetry

The study area for this chapter is located in the East Pass, Destin, FL, and the principal characteristics of the datasets were introduced in Chapter 3. Airborne LiDAR bathymetry was retrieved from the Optech Titan multi-wavelength LiDAR point cloud. The point cloud acquired from channel 3 (532 nm) was first classified using the ground filtering algorithm described in (Axelsson, 2000). The water surface returns were retrieved from the simultaneously collected channel 1 and 2 (1550 nm and 1064 nm respectively) observations. Details regarding bathymetry retrieval from LiDAR can be found in chapter 4. A model for water refraction was applied to the benthic layer point cloud to correct for the true water depth. Land points were removed after classification using a simple elevation threshold. Figure 7.1(a) shows the resultant LiDAR derived water bathymetry map.

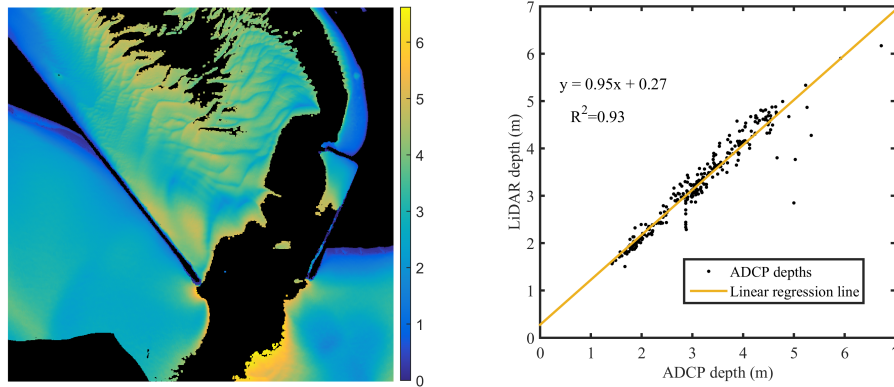


Figure 7.1 (a) Acquired airborne LiDAR bathymetry and the maximum detected water depth is about 6 m; (b) comparison of LiDAR derived water depths and field measured water depths.

Because LiDAR bathymetry is used as a comparison baseline and also for investigation of water bathymetry derived from bathymetric LiDAR only, we performed a comparison of LiDAR depths and field ADCP water depths, and the results are shown in Figure 7.1(b). LiDAR depths agree with field measurements well with a R^2 of 0.93 and a RMSE of 16 cm.

7.2.2 Nonlinear Least Square Optimization (nLSQ)

The water leaving remote sensing reflectance model is given in chapter 2 by Equations 2.1 to 2.8. Except for the water constituent concentrations, all the other empirical parameters were given in Tables 2.1 and 2.2. The water leaving remote sensing reflectance is therefore summarized as a function of four unknown parameters

$$R(\lambda) = f(C_{CHL}, C_{CDOM}, C_{NAP}, d), \quad (7.1)$$

where C_{CHL} , C_{CDOM} , C_{NAP} are concentrations for CHL, CDOM, and NAP respectively and d is the optical water depth.

Generally, at least 4 spectral bands are required, however, the extra spectrum in hyperspectral imagery allow for an optimization when solving for the unknown parameters. The optimization is formulated to derive all four parameters in Equation 7.1 using the objective function:

$$\arg \min \sum_{i=1}^n \frac{\sqrt{(\mathbf{R} - \mathbf{r})^2}}{\mathbf{R}}, \quad (7.2)$$

where n is the number of spectral bands in the hyperspectral imagery ($n > 4$). This inversion optimization method is attributed to Lee *et al.* (1999), Brando *et al.* (2009) and Dekker *et al.* (2011) and solved with nonlinear least squares using the MATLAB optimization toolbox. An example of modeled spectra with estimated parameters and the original spectra is shown in Figure 7.2.

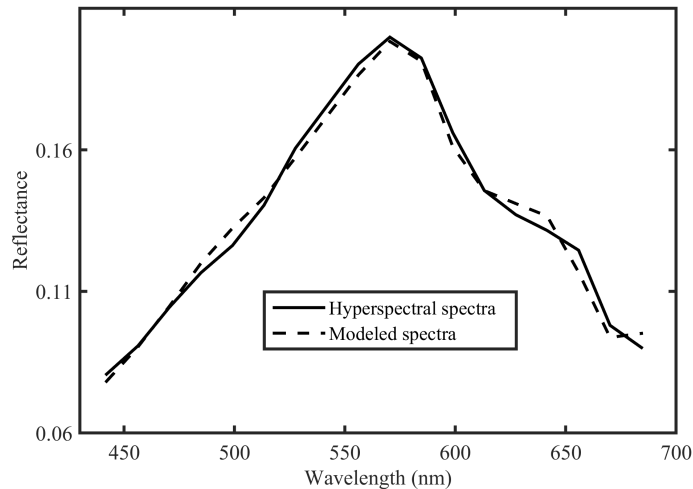


Figure 7.2 A sample hyperspectral spectrum and modeled spectrum with nLSQ estimated parameters.

The nLSQ approximates the observed spectrum by altering the four parameters, and then the parameter set that fits the spectrum best are extracted to represent the water column constituents and bathymetry. nLSQ is a pixel-wise method and therefore parameters for each pixel are determined independently.

7.2.3 Model based Support Vector Regression (mSVR)

SVR is a supervised learning scheme that requires known training samples to establish the correlation between observations and physical parameters. Equation 2.1 to Equation 2.8 describe a possible methodology to create artificial truth data using known empirical parameters. A database of remote sensing reflectance is constructed corresponding to various parameters combinations. Figure 7.3 shows a sample of generated spectra with varying water depth and fixed water column characteristics. Because this method utilizes a forward model without inversion of hyperspectral spectra, it is referred to as model based support vector regression (mSVR) to separate it from conventional SVR calibrated with field measured samples.

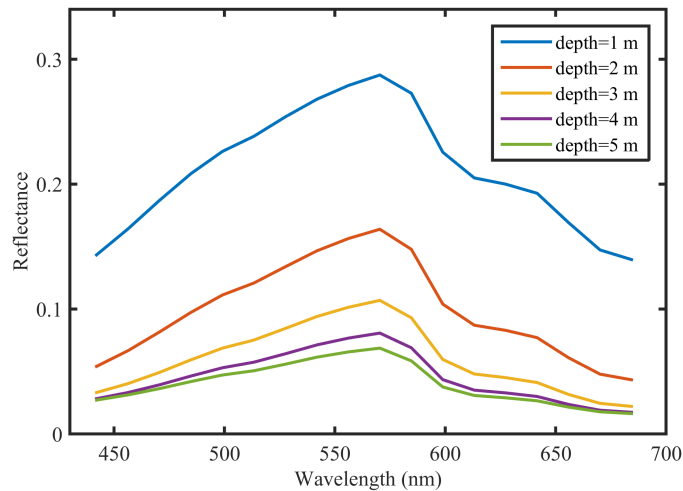


Figure 7.3 Modeled hyperspectral spectra with varying water depth but fixed water column characteristics.

Instead of an extensive database, we constructed a database with randomly chosen combinations of these four parameters to create a realistic range of spectra samples. The calibration sample size was first determined through a sensitivity analysis. By increasing the randomly chosen calibration samples from 100 to 1000 and fixing the validation sample

size at 1000 within a specified range (will be explained in the result section), we investigated the sensitivity of estimating these four parameters. Each experiment was repeated 10 times and the root-mean-square-error (RMSE) was reported. Figure 7.4 shows the RMSE with each calibration sample size. The results show that RMSE decreases with increasing calibration sample size, however, the reduction slows down significantly after 700 samples. Therefore, we conservatively chose to use 1000 random calibration samples as a reasonable trade-off between accuracy and computation speed. The machine learning process is performed on the calibration data and applied to the 1000 randomly generated validation samples to seek the optimal parameters. The derived optimal model is then applied to the hyperspectral imagery to estimate the physical parameters. Because there are four unknown parameters for each spectrum, independent SVR estimation was run to solve for each parameter individually.

7.3 Results

7.3.1 nLSQ

According to Brando *et al.* (2009), the initial values and estimation range are critical for optimization because nLSQ only provides a local minima solution. Unfortunately, no field data was available to provide the initial estimates for water column characteristics and bathymetry. Therefore, the initial values and the constraints given in Table 7.1 were used; they were determined from an unbounded least square solution, and therefore should be representative ranges to ensure that the nLSQ solutions converges.

Table 7.1 Parameter constraints and initial values for the nLSQ solution.

Parameters	Range	Initial value
$C_{CHL} (\mu g \cdot L^{-1})$	0.0-2.2	0.07
$C_{CDOM}(m^{-1})$	0.0-1.0	0.5
$C_{NAP}(mg \cdot L^{-1})$	0-15	10
$d(m)$	0-7	2

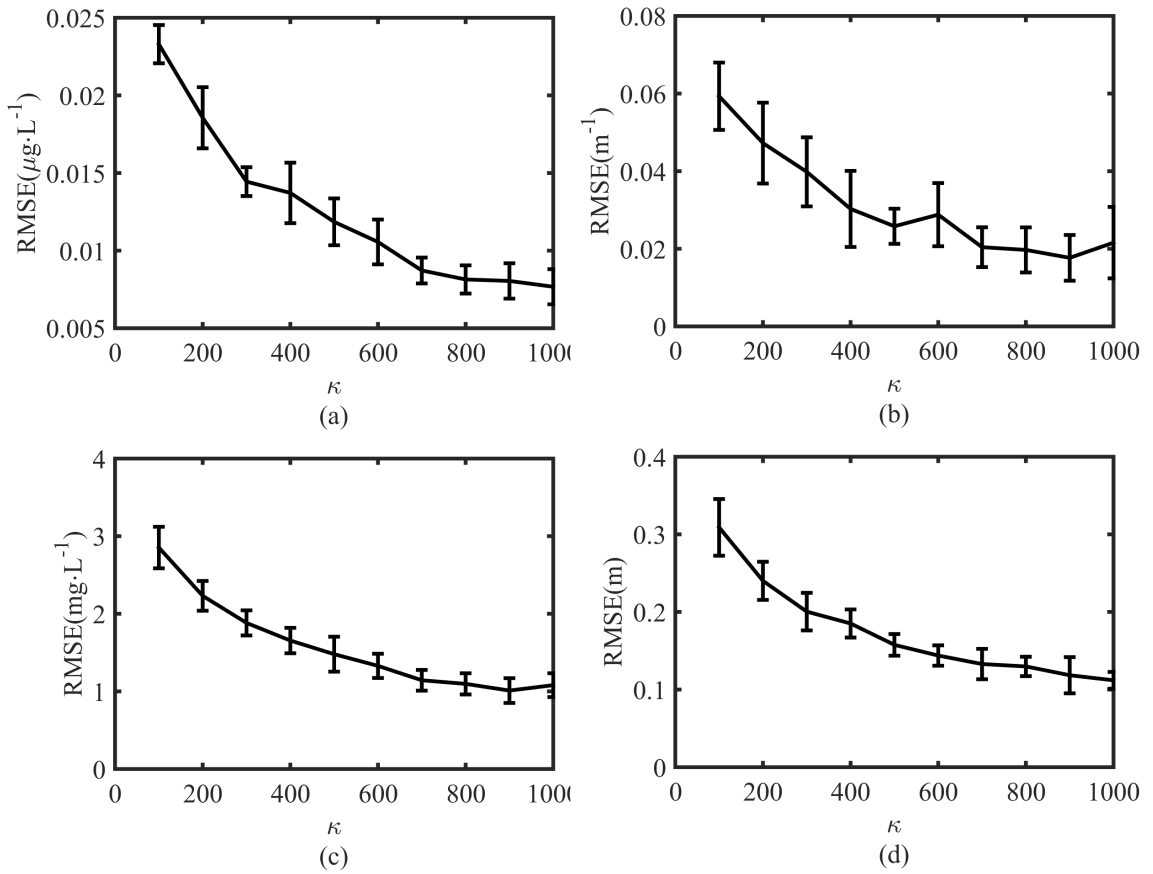


Figure 7.4 Error bar plots of RMSE variation with increasing calibration sample size: (a) RMSE of CHL; (b) RMSE of CDOM; (c) RMSE of NAP; (d) RMSE of water bathymetry. κ is the calibration sample size.

The nLSQ method is a pixel-wise method and therefore four parameters were derived for each pixel. Figure 7.5 shows spatial plots of all four parameters estimated for the study area.

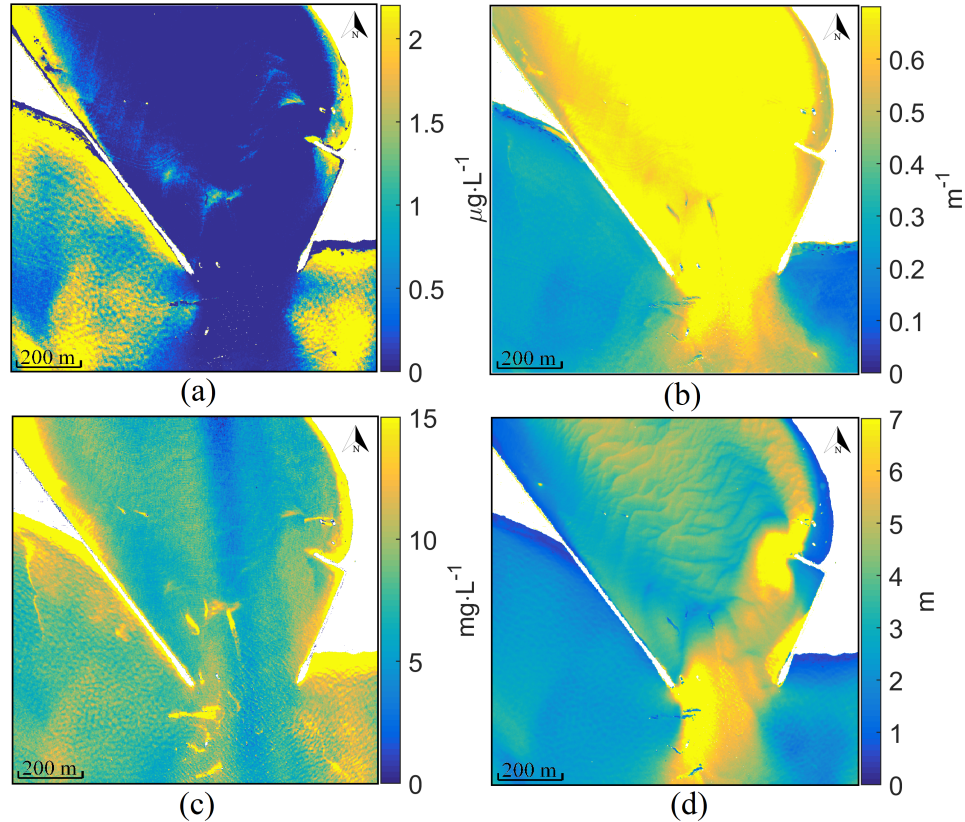


Figure 7.5 Water column characteristics estimated with hyperspectral imagery inversion with nLSQ: (a) concentration of CHL ($\mu\text{g} \cdot \text{L}^{-1}$); (b) measure of the CDOM (m^{-1}); (c) concentration of NAP ($\text{mg} \cdot \text{L}^{-1}$); (d) water bathymetry (m).

Comparing Figure 7.5(a) and (d), the concentration of chlorophyll-a is higher for shallower coastal water and decreases in deeper water. NAP concentration (Figure 7.5(c)) is more or less consistent. The concentration of CDOM (Figure 7.5(b)), however, shows that the East Pass channel water has higher concentration than the coastal water, which is regulated by the twin jetties. The plume of CDOM also clearly shows that inlet water affects the coastal water at the jetty opening. The water column characteristics agree with intuition because the East Pass is a coastal area with many recreational boats on the inlet water that may produce more dissolved organic matters in the inlet water. The water bathymetry

retrieved from nLSQ also shows a clear bottom structure.

From Equation 7.1 and Table 7.1, the bathymetry derived from LiDAR can be used to constrain the nLSQ by fixing the water depth d . nLSQ was therefore implemented, with LiDAR depths constrained using the same water constituent parameters. The solution for the water column characteristics are shown in Figure 7.6. Note that areas where there was no LiDAR bathymetry observations were masked out of the computation.

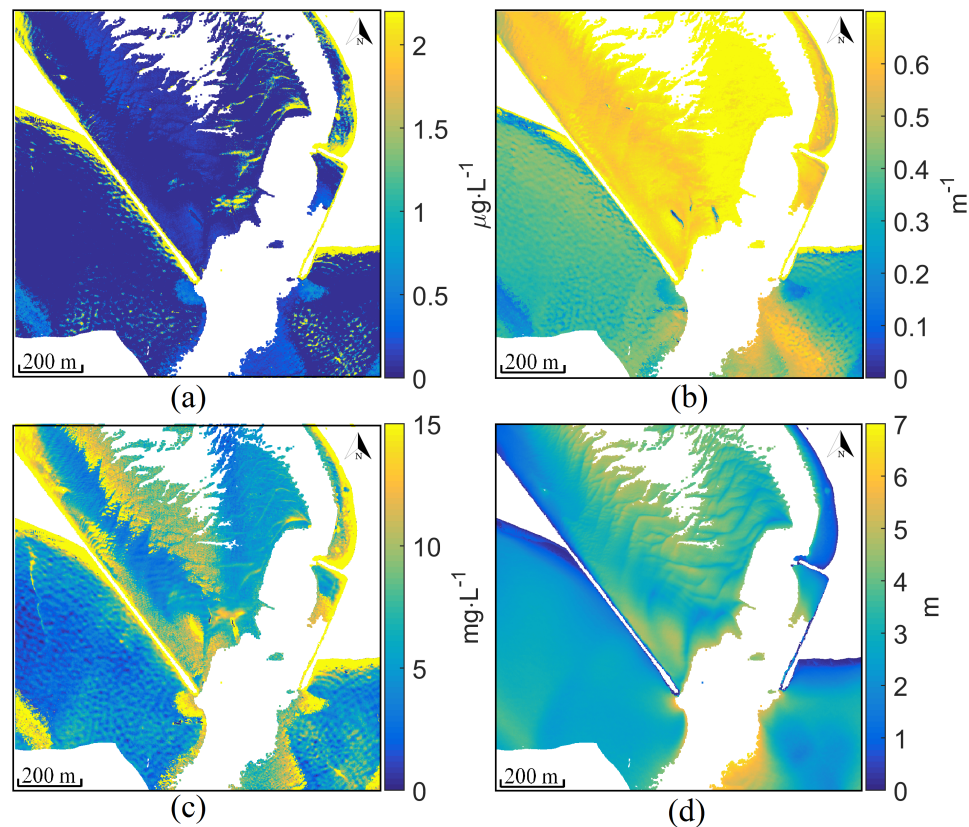


Figure 7.6 Water column characteristics estimated with nLSQ and LiDAR depths constraint: (a) concentration of CHL ($\mu\text{g}\cdot\text{L}^{-1}$); (b) measure of the CDOM (m^{-1}); (c) concentration of NAP ($\text{mg}\cdot\text{L}^{-1}$); (d) water bathymetry (m).

The water depth map given in Figure 7.6(d) is identical to the LiDAR bathymetry map (see Figure 7.1(a)) because it was constrained. An examination of Figure 7.6 (a), (c) and (d), shows that the concentrations of CHL and NAP were changed by the LiDAR bathymetry constraint, while the estimated chlorophyll is close to 0 for the entire image,

which may be reasonable because the chlorophyll is not expected to be significant in this area. The concentration of colored dissolved organic matter shows a consistent pattern compared to Figure 7.5(b).

7.3.2 mSVR

The mSVR method requires calibration samples to estimate parameters from the observed hyperspectral spectra. For comparison with nLSQ, the parameters ranges listed in Table 7.1 were also applied to mSVR. The calibration samples were randomly generated with random concentrations and depths within the specified ranges. Because mSVR is a statistical method, the experiment for each parameter estimation was run 40 times. 1000 calibration samples and 1000 validation samples were created for each iteration to search for the optimal parameters using a grid search (see chapter 5). The trained model was then applied to derive parameters from the observed hyperspectral imagery and the average estimates for each parameter are shown in Figure 7.7.

Figure 7.7(a) show that the concentrations of chlorophyll-a is higher for the shallow water area and Figure 7.7(c) shows the NAP is nearly consistent for the entire area, which is similar to the results obtained using nLSQ (see Figure 7.5). The concentration of CDOM is consistent with the nLSQ estimate showing the East Pass water with higher concentration than the coastal water. The bathymetry results from the mSVR method (Figure 7.7(d)) show similar structure to the nLSQ result.

For nLSQ the significance of fusing LiDAR bathymetry and hyperspectral imagery was investigated by adding LiDAR depths as a constraint to the optimization. However, a similar approach is not applicable for mSVR because a constraint cannot be added to the statistical estimation. Therefore, to investigate the significance of LiDAR bathymetry for hyperspectral inversion in mSVR, the hyperspectral feature set was expanded by adding bathymetry acquired by LiDAR as an additional feature. The calibration and validation

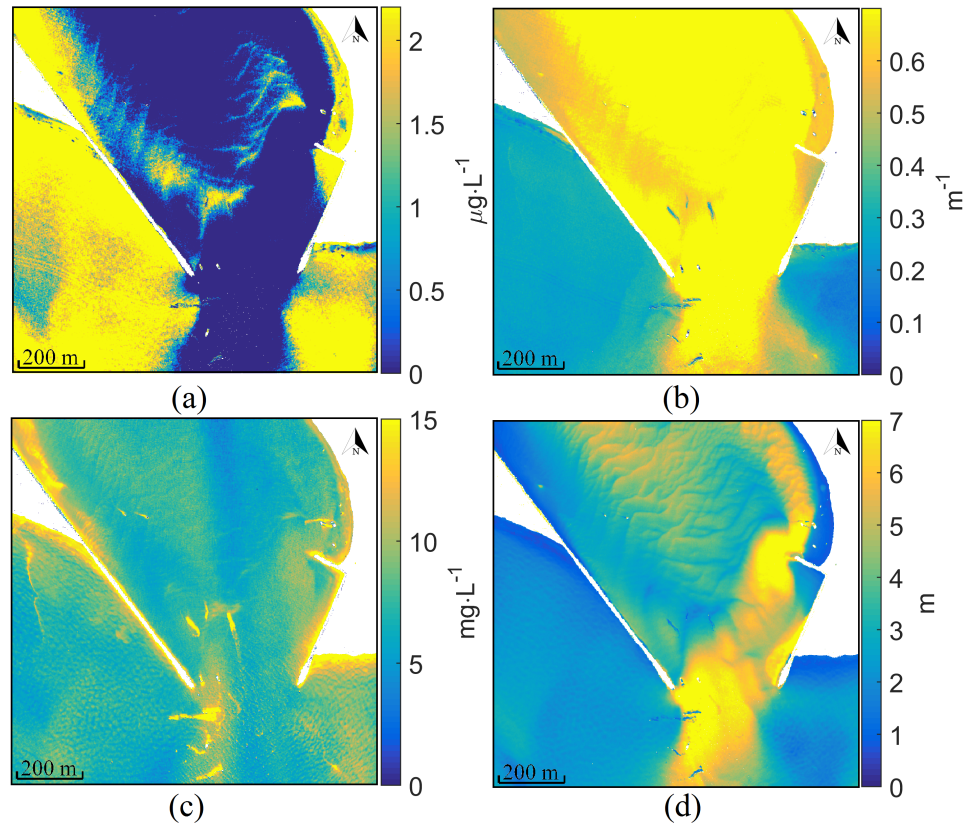


Figure 7.7 Water column characteristics estimated from hyperspectral imagery with mSVR: (a) concentration of CHL ($\mu\text{g}\cdot\text{L}^{-1}$); (b) measure of the CDOM (m^{-1}); (c) concentration of NAP ($\text{mg}\cdot\text{L}^{-1}$); (d) water bathymetry (m).

samples were generated using the same strategy as above to estimate the water column parameters for the fused feature dataset and the results are shown in Figure 7.8.

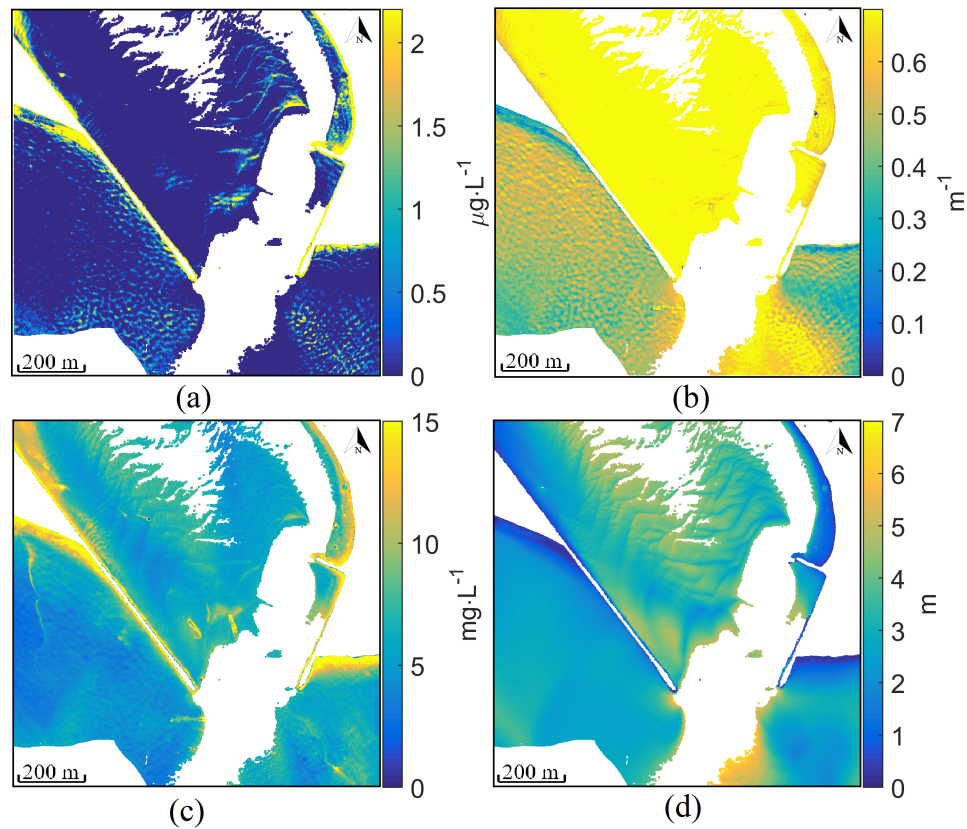


Figure 7.8 Water column characteristics estimated with mSVR and LiDAR depths constraint: (a) concentration of CHL ($\mu\text{g}\cdot\text{L}^{-1}$); (b) measure of the CDOM (m^{-1}); (c) concentration of NAP ($\text{mg}\cdot\text{L}^{-1}$); (d) water bathymetry (m).

In Figure 7.8 the concentration estimated for chlorophyll is close to 0 for the entire image while NAP is almost constant for the entire area. The map of CDOM shows higher concentration for the East Pass water and also clearly indicates the influence of the twin jetties. The bathymetry product is highly close to the LiDAR bathymetry with slight variations because it is estimated from the combined feature data-sets.

7.3.3 Comparison of nLSQ, mSVR and Conventional SVR

Even though we lack in-situ field observations of water column constituent to fully assess the accuracy of both nLSQ and mSVR for water column characteristics estimation, the water depths collected with ADCP and LiDAR give us an opportunity to assess the performance of these approaches for bathymetry retrieval. To compare different bathymetry products, we also derived water bathymetry estimates from hyperspectral imagery with calibration samples from both ADCP and LiDAR bathymetry respectively using a conventional SVR approach. All 423 ADCP samples were used in the derivation of bathymetry, and the result is referred to as ASVR. 1000 calibration samples and validation samples were extracted from the LiDAR only bathymetry map. These results are therefore referred to as LSVR because of the use of LiDAR bathymetry (see procedure in Chapter 5). Four different water bathymetry products are then available: ASVR bathymetry, LSVR bathymetry, nLSQ bathymetry (no constraint) and mSVR bathymetry (no constraint). These four bathymetry products are shown in Figure 7.9. Figure 7.9(a), (c) and (d) show that ASVR, nLSQ and mSVR both show detailed structure in the deeper water area. LSVR failed in the deeper water area due to the lack of deeper water observations from LiDAR.

Because only a handful of ADCP samples are available and because the LiDAR bathymetry was shown to be reliable in Figure 7.1(b), the four bathymetry maps derived from hyperspectral imagery were compared to LiDAR bathymetry to investigate their error distribution (see Figure 7.10). Statistics including median and the interquartile range (IQR) are reported in Table 7.2 for all error estimates.

Figure 7.10 and Table 7.2 show that the small number of calibration samples from ADCP yielded a poor estimate of bathymetry compared to the other methods. LSVR yielded the best bathymetry with 0 median and 14 cm IQR. nLSQ and mSVR have similar

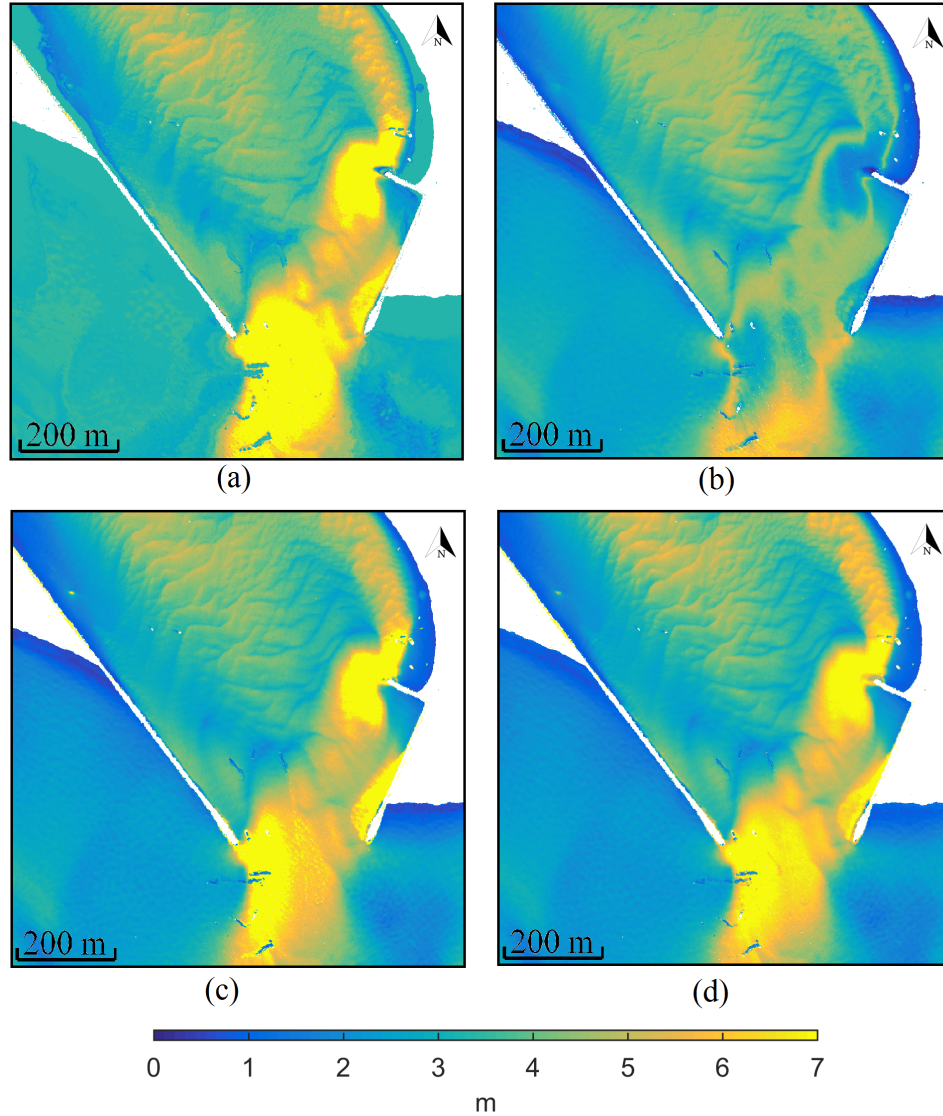


Figure 7.9 (a) Depth map derived from ASVR estimation; (b) depth map derived from LSVR estimation; (c) depth map derived from nLSQ optimization; (d) depth map derived from mSVR estimation.

Table 7.2 Statistical comparison of hyperspectral imagery derived bathymetry products to LiDAR bathymetry ($d_h - d_L$, d_h is the hyperspectral bathymetry, d_L is the LiDAR bathymetry).

	ASVR	LSVR	nLSQ	mSVR
Mean (m)	0.25	0.01	-0.28	-0.40
Standard deviation (m)	0.51	0.13	0.19	0.20
RMSE (m)	0.57	0.13	0.34	0.44
Median (m)	0.15	0.00	-0.29	-0.41
IQR (m)	0.75	0.14	0.22	0.23

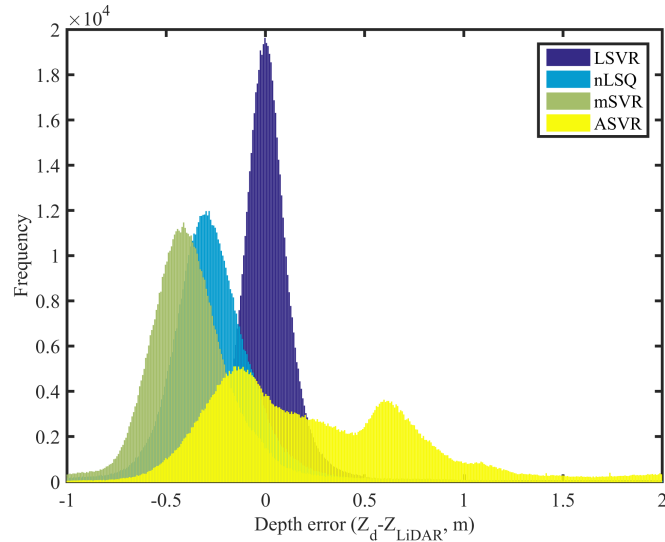


Figure 7.10 Histograms of different water bathymetry products compared to LiDAR bathymetry. Z_d is the derived water depths and Z_{LiDAR} is the LiDAR bathymetry

IQR but mSVR has a lower median error. The differences between mSVR and LSVR also indicates that discrepancies exist between the bi-optical model and the actual hyperspectral data. To further evaluate bathymetry retrieval performance for the three hyperspectral imagery derived water bathymetry products (ASVR is excluded due to poor results), they were also compared against ADCP depth samples to examine performance in deeper water because LiDAR only contained depth measurements for water up to 6 m deep in this study. The comparisons are shown in Figure 7.11.

Although Table 7.2 shows that LSVR performs excellently for shallow water bathymetry retrieval, its performance degrades after 5 m because there are less available LiDAR samples for deeper water. The performance of ASVR and LSVR suggest a significant limitation for field data based bathymetry retrieval; a representative distribution of training samples including deep water observations are essential to retrieve accurate bathymetry from hyperspectral imagery. The model based methods nLSQ and mSVR do not have this limitation because artificial calibration samples are generated that can cover all desired water depths. However, both nLSQ and mSVR show that the model based water depths derived from

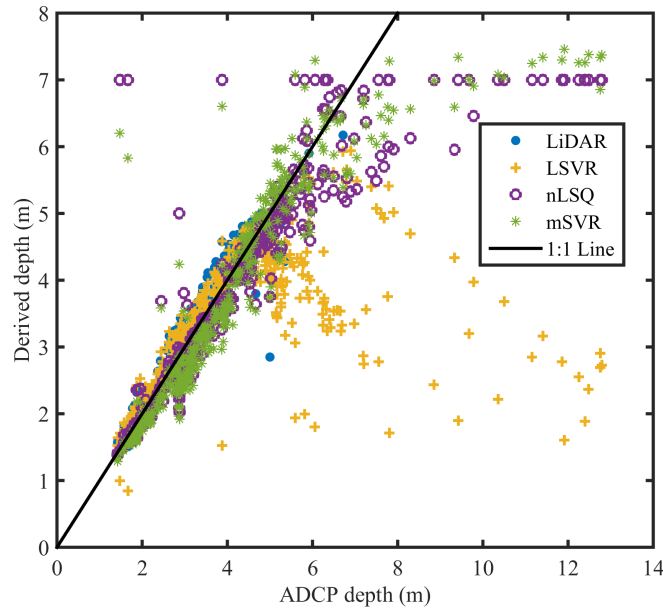


Figure 7.11 Comparison of derived bathymetry products with ADCP water depth samples.

hyperspectral imagery saturate if the water is deeper than 7 m because of the significant decrease of benthic contribution. This also suggests a significant limitation for inversion because a well-defined parameter range is essential if we hope to maintain an accurate hyperspectral inversion using either nLSQ and mSVR. According to Chapter 2, depth uncertainty increases with increasing water depth (see Figure 2.17), which suggests that an improperly defined parameter range, especially an overestimated range, can result in significant errors for the estimated parameters.

7.3.4 Fusion of LiDAR and Hyperspectral Imagery

An examination of Figures 7.5 to 7.8, shows that both nLSQ and mSVR have the capability to predict water column characteristics and bathymetry simultaneously. However, the fundamental concepts underlying these two methods are different: nLSQ is an inversion method where the parameters are estimated through the fitting of hyperspectral spectrum with an established model; whereas mSVR learns the pattern in derived artificial spectra and predicts each parameter from the hyperspectral imagery independently. To further

compare these two methods, the parameters estimated are used to compute fitting spectra and then an R squared value map is calculated by comparing the generated and observed spectra from each method.

Figure 7.12(a) and (b) show the R squared value maps for nLSQ and mSVR respectively using hyperspectral imagery only. nLSQ shows good agreement between the modeled and observed spectra with relatively high R^2 , however, the deep water areas show relatively lower R^2 due to the low signal to noise ratio (SNR). mSVR has slightly lower R^2 compared to nLSQ because it estimates each parameter independently. Figures 7.12(c) and (d) show the R^2 value maps for nLSQ and mSVR using a fused input dataset. nLSQ still shows better agreement between the modeled and observed spectra compared to mSVR. However, the performance of both nLSQ and mSVR degrade with the fused dataset. The reason for this phenomena is that water depth is the dominant factor in the observed hyperspectral spectra, and any random or systematic discrepancies between the hyperspectral imagery derived bathymetry and LiDAR bathymetry (see Figure 7.11) resulted in less optimal nLSQ and mSVR performance.

Because both nLSQ and mSVR can use LiDAR bathymetry as either a constraint or an extra feature respectively, the significance of the contribution of LiDAR for parameter estimation from hyperspectral imagery is critical to investigate. Unfortunately, a conventional accuracy assessment is not feasible for this study because of the lack of field measurements of the other three water column constituent. However mSVR, which is a statistical method, enables us to investigate the distributions of standard deviations for all iterations to partially assess the significance of data fusion; the results are displayed in Figure 7.13.

The addition of LiDAR bathymetry to the feature space actually makes the water constituent estimation standard deviation higher than with hyperspectral imagery only. However, the bathymetry estimates standard deviation decreases with the fused dataset. This is consistent with the results in Figure 7.12 because of the discrepancies between LiDAR

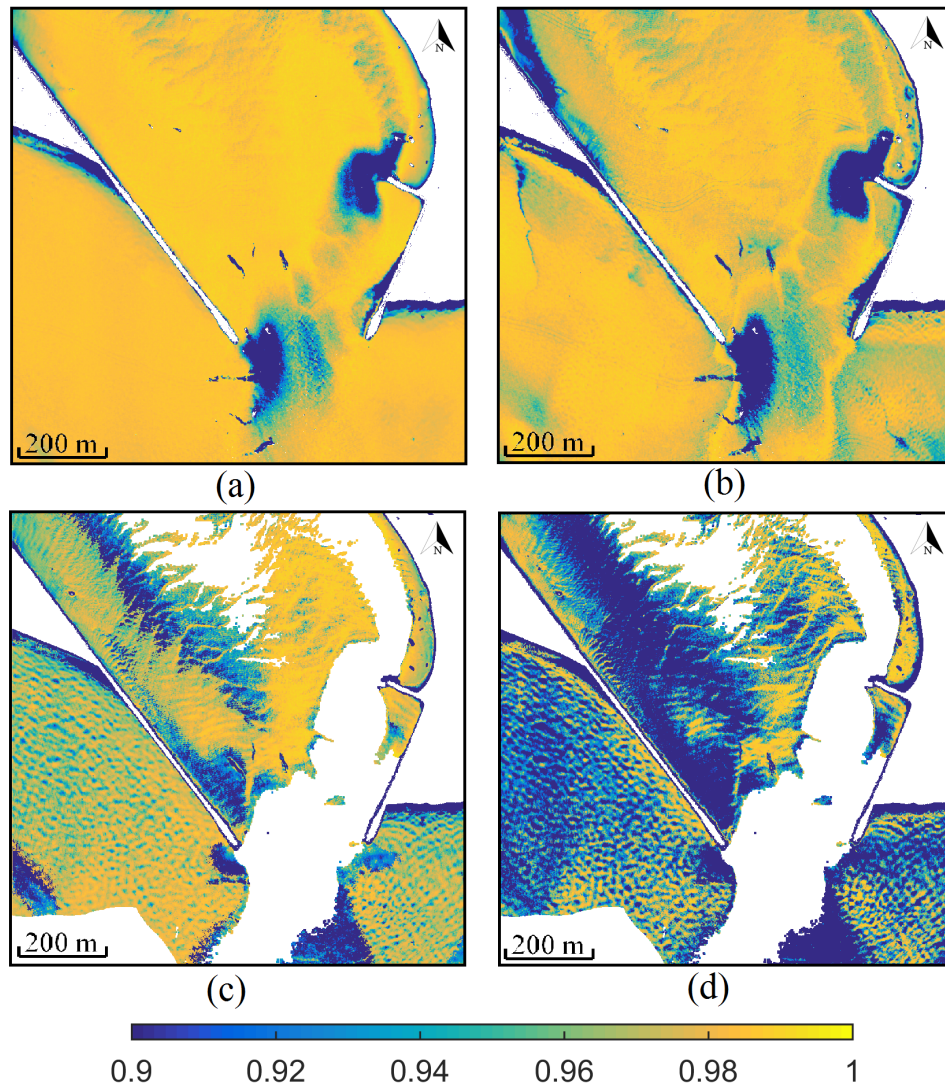


Figure 7.12 (a) R^2 map for nLSQ (hyperspectral imagery only); (b) R^2 map for mSVR (hyperspectral imagery only); (c) R^2 map for nLSQ (fusion); (d) R^2 map for mSVR (fusion).

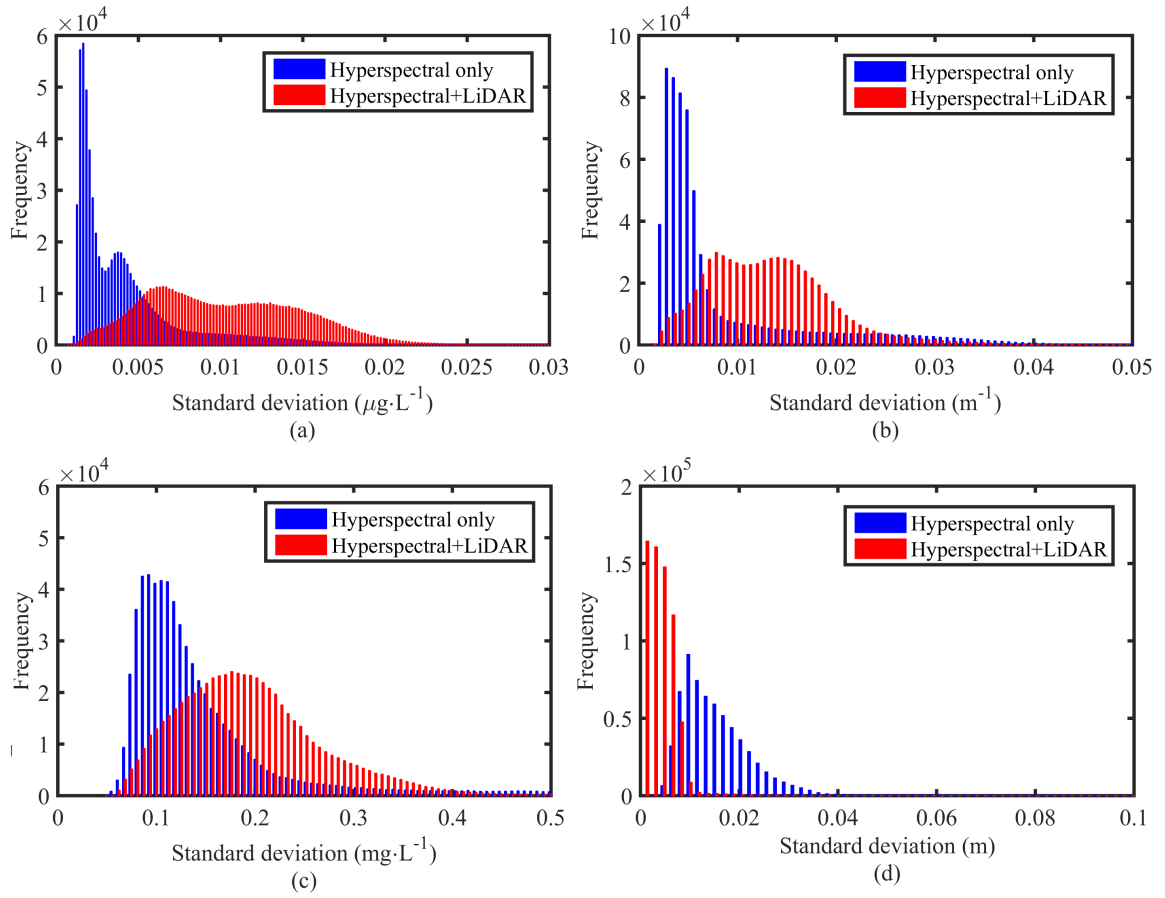


Figure 7.13 (a) Standard deviation distribution for CHL; (b) standard deviation distribution for CDOM; (c) standard deviation distribution for NAP; (d) standard deviation distribution for water depth.

and hyperspectral derived bathymetry products. However, the higher estimation standard deviation does not necessarily mean that fusing bathymetric LiDAR and hyperspectral imagery is insignificant. The benthic layer of this study area is mostly white sand which represents an ideal observation case and may mask the influence of the LiDAR observations. There is evidence elsewhere that the LiDAR constraint is significant to hyperspectral imagery for shallow water remote sensing when considering the varied substrate types (Torres-Madronero *et al.*, 2009, 2014)

7.4 Discussion

This Chapter presented different methods to estimate water column constituent concentrations and bathymetry from hyperspectral imagery. Four bathymetry products were derived from hyperspectral imagery with different methods: ASVR, LSVR, nLSQ, and mSVR. The hyperspectral imagery derived bathymetry products were compared to LiDAR bathymetry and also to field measured ADCP depths. ASVR didn't produce accurate and consistent results due to the inadequate number of ADCP samples. LSVR, however, showed overall best performance with a 14 cm IQR. nLSQ and mSVR showed similar results with 22 cm and 23 cm IQR respectively. Comparisons with LiDAR only bathymetry showed that LSVR yielded the best results for bathymetry retrieval with the highest accuracy. Both nLSQ and mSVR performance degrade for deeper water areas (>6 m) due to decreased benthic contribution in the observed reflectance. LiDAR bathymetry can also be used as a constraint in the hyperspectral imagery inversion optimization or as an extra feature for the derivation of water column characteristics using mSVR. Without in situ field measured water column parameters, the accuracy of both methods for the estimation for water column constituent was unfortunately not assessed in this study.

The estimated water column constituent concentrations for optically shallow water are

larger than in the deeper water areas in this study, especially for CHL products. This is because water column constituents have less effect on the observed remote sensing spectrum and thus the estimation uncertainty is higher (Cannizzaro and Carder, 2006). In addition, water depth estimation has higher uncertainty in deeper water because there is less benthic reflectance observed in the remote sensing spectrum (Jay and Guillaume, 2016), which can be seen from the comparison with ADCP water depths. More constrained and regularized methods have been proposed to inverse hyperspectral spectrum with both spatial and spectral proximity (Jay and Guillaume, 2014, 2016) on more complex scenes with varying substrate types. Also, Torres-Madronero *et al.* (2014) showed the possibility of using the bi-optical model for linear unmixing of substrate types. The more parameters included in the model, the more complexity and uncertainty in the resultant estimated parameters (Jay and Guillaume, 2016). Even though we lack the field measured water constituent concentrations to demonstrate that there are accuracy improvements through fusing LiDAR bathymetry and hyperspectral imagery, the mathematical advantages for data fusion imply that the LiDAR bathymetry constraints are likely to improve the estimation of other parameters. The fusion of LiDAR bathymetry and hyperspectral imagery was implemented for both the nLSQ and mSVR methods. LiDAR bathymetry either constrains the optimization solution or adds an extra feature respectively. The derived water column constituent concentrations were different, but unfortunately are not verified for their accuracy due to the lack of independent field measurements. We did however briefly evaluate the statistical influence by comparing the standard deviations from the mSVR method before and after the addition of the LiDAR bathymetry feature set. The water constituent estimation standard deviation degraded with the addition of LiDAR features due to the differences between the hyperspectral and LiDAR derived bathymetry. The significance of data fusion remains unknown, but the other references in the literature reported improvements with the fusion of LiDAR and hyperspectral imagery for bathymetry (Tuell and Park, 2004; Park *et al.*,

2010; Torres-Madronero *et al.*, 2009, 2014). Therefore, a validation of the significance of fusing LiDAR and hyperspectral imagery with the proposed methods is a future research direction.

In a conclusion, both nLSQ and mSVR methods can estimate shallow water column characteristics and bathymetry, and nLSQ is slightly better than the mSVR method with slightly better R^2 goodness of fit. However, the significance of mSVR is that it uses the forward modeling of hyperspectral spectrum and therefore is possible to include other radiative transfer models, for example, the forward HydroLight software. The nLSQ and mSVR both need the benthic spectra and spatial distribution to correctly estimate the water column constituent concentrations, which is also a limitation of the semi analytical method.

Chapter 8

Conclusions and Future Research Directions

8.1 Conclusions

This dissertation has evaluated the performance of full waveform bathymetric LiDAR and hyperspectral imagery for shallow water bathymetry estimation. Two distinct river systems and one coastal area were investigated and different processing algorithms were proposed for analyzing the remote sensing data. Significant improvements were realized compared to conventional processing strategies presented in the literature that analyze bathymetric LiDAR and hyperspectral imagery separately. The fusion of bathymetric LiDAR and hyperspectral imagery was also performed and assessed for bathymetry, but not fully assessed for water column constituent concentrations due to the lack of corresponding field measurements. The major conclusions are briefly summarized in the sections that follow.

From discrete to full waveform bathymetric LiDAR

Full waveform LiDAR processing produces a significantly denser point cloud with more multiple returns than discrete bathymetric LiDAR. The presence of multiple returns improves bathymetric estimation and enables the recovery of a more accurate benthic layer. In contrast to conventional Gaussian decomposition methods, the proposed CWT method showed better stability through varying water clarity conditions. However, a single waveform algorithm was not found to be superior for all water conditions, which indicates that in the future LiDAR full waveform processing packages should include many full waveform processing strategies, allowing the user to select the most appropriate algorithm that yields the best performance for their specific project. A single band full waveform bathymetric LiDAR system doesn't appear to be as accurate as a multi-wavelength system that utilizes

NIR LiDAR returns to detect the water surface. The degraded performance of the single band bathymetric LiDAR over the turbid river showed the significant influence of the water column return on the water depth determination. Therefore, the addition of water column backscattering in the full waveform modeling has a promising potential to further improve the performance of single band shallow water bathymetric LiDAR.

From band ratio to full spectra hyperspectral imagery bathymetry

Compared to the band ratio method commonly used for shallow water bathymetry retrieval (Legleiter *et al.*, 2009), the proposed SVR algorithm utilizes the full image spectra to retrieve water bathymetry. The generalized OBRA establishes a physical model and then uses an empirical method to find the optimal pair of spectral bands and neglects all other spectral channels. Its performance unfortunately doesn't improve with an increase in the training sample size. The proposed SVR algorithm investigates the intrinsic connection between physical parameters and the observed dataset and improves the bathymetry estimation significantly. The nonparametric regression characteristics of SVR also enabled the retrieval of water turbidity from hyperspectral imagery; further validating its superior applicability for water column characteristics retrieval. However, the requirement of supervised regression for SVR is also a limitation because sufficient training samples are required for a successful bathymetry retrieval.

From full waveform to orthowaveform bathymetric LiDAR

The conventional full waveform returns collected by airborne LiDAR systems are generally decomposed to determine the water surface and benthic returns to infer water depth with a constant speed of light in water. However, the assumption of a model may remove significant backscatter information encapsulated in the full waveform profile which could be exploited. Inspired by the research described in Park *et al.* (2014), Wang and Glennie

(2015) and Jung and Crawford (2012), we proposed an orthowaveform that was generated from overlapping full waveforms and investigated its performance for retrieving water bathymetry and turbidity. The generated orthowaveforms preserved most of the information contained in the full waveform, and when trained using in situ field measurements, SVR correlated well with water depths and turbidity measurements. The comparison between hyperspectral imagery and orthowaveform derived bathymetry showed a substantial improvement with orthowaveforms for more turbid water. The comparison between the orthowaveforms and the full waveform processing algorithms also shows a significant improvement for more turbid water when using the orthowaveforms. Water turbidity was also successfully retrieved from the orthowaveforms showing that there is potential to extract other water column parameters from full waveform LiDAR.

From statistical algorithms to spectral physics based algorithms for hyperspectral imagery remote sensing

The statistical methods presented in chapter 5 and 6 successfully estimated water bathymetry and turbidity from hyperspectral imagery. The bind between water column constituents and bathymetry makes it difficult to isolate any single parameter physically. The semi-analytical method shown in chapter 2 established a relationship between water column characteristics, bathymetry and remote sensing reflectance. This analytical model enables a hyperspectral inversion that estimates all water column characteristics and bathymetry simultaneously. The significance of the analytical modeling is that it does not only improve estimation of shallow water bathymetry, but also enables environmental assessment of fluvial and coastal areas. Lee *et al.* (2001), Brando *et al.* (2009) and Torres-Madronero *et al.* (2009) have further proved the efficiency of this model for substrate types classification. It is a promising approach to estimate water bathymetry, water column characteristics and substrate types simultaneously for a complete remote sensing solution for fluvial and near coastal region monitoring. In contrast to the inversion method,

the proposed model based SVR method learns the existing pattern from artificial spectra data, and then the derived optimal model was applied to observed hyperspectral imagery for the derivation of the water column constituents and bathymetry estimation. Comparable performance was achieved, and this forward model has high adaptability to other forward radiative transfer models, for example, HydroLight.

Fusion of bathymetric LiDAR and hyperspectral imagery

The fusion of bathymetric LiDAR and hyperspectral imagery was implemented both in chapters 6 and 7. In Chapter 6, the generated orthowaveforms were combined with hyperspectral imagery to estimate water bathymetry and water turbidity. The results show a slight improvement when compared to either orthowaveforms or hyperspectral imagery alone. In the analytical method present in chapter 7, LiDAR bathymetry was used to constrain the hyperspectral imagery inversion and also used to expand the feature set of the hyperspectral imagery. The fusion results did influence the estimation of water column characteristics, but the actual evaluation of the significance was not performed because of the lack of field measured water column constituents. However, the concept and the qualitative visual results suggest a promising potential for future fluvial or coastal remote sensing to implement fusion to acquire more accurate environmental parameter estimates.

In conclusion, LiDAR provides a direct and accurate measurement of water depth. Full waveform bathymetric LiDAR provides optimal shallow water bathymetry information and therefore we suggest to include the waveform capability for future LiDAR systems. The limitations of monochromatic spectrum for current bathymetric LiDAR systems suggest that hyperspectral imagery is an important supplement for shallow water remote sensing, especially when more than just depths are required. The derived water column characteristics and substrate types can further derive more products for many applications,

such as hydrodynamics modeling, coastal and fluvial systems change detection, and resource management. The in situ field measurements are necessary to calibrate the acquired hyperspectral imagery, and also, the semi analytical modeling of the water spectra shows promising potential for the shallow water remote sensing community. The fusion of bathymetric LiDAR and hyperspectral imagery has a promise as well because of each method's distinct advantages and disadvantages and it can improve the overall performance and facilitate shallow water remote sensing applications.

8.2 Future Work Directions

Bathymetric full waveform modeling

Chapter 4 presented full waveform processing for shallow water bathymetric LiDAR. The improvement in both accuracy and point density were encouraging for future application of full waveform capability from other bathymetric LiDAR systems. However, the accuracy of benthic layer retrieval for a single wavelength bathymetric LiDAR remains a challenge due to the difficulty in isolating the water surface from the water column returns. Abady *et al.* (2014) showed a simulation result to improve bathymetry performance with the modeling of the water column return, enabling better separation of the water surface. This research direction needs to be expanded beyond simulation and also examined for other bathymetric LiDAR systems. With this potential enhancement, single wavelength bathymetric LiDAR performance may be comparable to dual wavelengths systems that use NIR returns to define the water surface. The modeled water column return would also enable an evaluation of water column characteristics, which would benefit hyperspectral imagery inversion by providing additional potential constraints.

Feature extraction from orthowaveforms

In contrast to conventional full waveform processing techniques, the orthowaveforms generated from the full waveforms preserve both the shape and spatial features encapsulated in the full waveform. Turbidity extraction from orthowaveforms with SVR showed that they could be efficiently applied to water column characteristics extraction. In addition to the orthowaveform generation presented in this dissertation, the optimal way of creating orthowaveforms from full waveforms to preserve contained feature still remains unknown. Orthowaveforms also have the capability to determine the shallow water bathymetry using 3D filtering techniques and some preliminary results have been shown in Park *et al.* (2014); therefore the investigation of the optimal way to determine shallow water bathymetry from orthowaveforms is a good research input for shallow water full waveform study. Even though the optical physics behind the orthowaveforms or full waveform is not defined, which would require complex laser temporal and spectral radiative transfer models, the application of advanced machine learning methods still shows great potential for generating water bathymetry and classifying substrate types. More advanced machine learning methods are promising to investigate and improve the information extraction from the generated orthowaveforms. More machine learning tools should also be examined to extract water column characteristics and water depth from the orthowaveforms, for example, a context based machine learning technique is expected to perform the extraction better than the pixel based technique used in the dissertation.

Fusion of LiDAR and hyperspectral imagery

The fusion of LiDAR and hyperspectral imagery is implemented in both chapter 6 and 7. However, only a slight improvement was found in Chapter 6, and Chapter 7 showed a degraded performance for the fusion strategy. Despite the neutral to negative effect of data fusion, the general advantage is that bathymetric LiDAR can provide the essential direct

water depth measurements to calibrate the shallow water hyperspectral imagery. More fusion studies are necessary in the future to fully assess its efficiency. Furthermore, it is also necessary to expand the semi analytical model coupled with LiDAR bathymetry to more areas with varying substrate type and water column characteristics. These varying parameters can help to investigate the capability of the fusion on the complete shallow water remote sensing solution: water constituent concentration estimation, shallow water bathymetry extraction, and benthic layer classification. More in situ field measurements, including water constituent concentrations and water sample spectra, are also necessary to calibrate the semi analytical model, examine the performance of water column parameters extraction, and fully assess the performance of the fusion strategies.

Bibliography

- Optech. The summary specification sheet of the Aquarius sensor. URL http://www.teledyneoptech.com/wp-content/uploads/specification_aquarius.pdf. Accessed on October 30th, 2015.
- ReSe. Atcor4: Atmospheric & topographic correction for wide fov airborne optical scanner data. URL <http://www.rese.ch/products/atcor/atcor4/>. accessed 9/5/2014.
- Riegl. Datasheet for RIEGL VQ-820-G. URL <http://products.rieglusa.com/item/airborne-scanners/vq-820-g-airborne-laser-scanners/riegl-vq-820-g>. Accessed on October 30th, 2015.
- IHO Standards for Hydrographic Surveys, Special Publication N44, February 2008.
- Abady, Lydia; Bailly, Jean-Stephane; Baghdadi, Nicolas; Pastol, Yves, and Abdallah, Hani. Assessment of Quadrilateral Fitting of the Water Column Contribution in Lidar Waveforms on Bathymetry Estimates. *IEEE Geoscience and Remote Sensing Letters*, 11(4): 813–817, 2014. ISSN 1545-598X.
- Abdallah, H.; Baghdadi, N.; Bailly, J-S; Pastol, Y., and Fabre, F. Wa-LiD: A New LiDAR Simulator for Waters. *IEEE Geoscience and Remote Sensing Letters*, 9(4):744–748, 2012. ISSN 1545-598X.
- Allouis, Tristan; Bailly, Jean Stéphane; Pastol, Yves, and Le Roux, Catherine. Comparison of LiDAR waveform processing methods for very shallow water bathymetry using Raman, near-infrared and green signals. *Earth Surface Processes and Landforms*, 35: 640–650, 2010. ISSN 01979337.
- Axelsson, Peter. DEM generation from laser scanner data using adaptive TIN models. *International Archives of Photogrammetry and Remote Sensing*, 33:111–118, 2000.
- Bouhdaoui, Anis; Bailly, Jean-Stephane; Baghdadi, Nicolas, and Abady, Lydia. Modeling

- the Water Bottom Geometry Effect on Peak Time Shifting in LiDAR Bathymetric Waveforms. *IEEE Geoscience and Remote Sensing Letters*, 11(7):1285–1289, 2014. ISSN 1545-598X.
- Brando, V.E. and Dekker, A.G. Satellite hyperspectral remote sensing for estimating estuarine and coastal water quality. *IEEE Transactions on Geoscience and Remote Sensing*, 41(6):1378–1387, 2003. ISSN 0196-2892.
- Brando, Vittorio E.; Anstee, Janet M.; Wettle, Magnus; Dekker, Arnold G.; Phinn, Stuart R., and Roelfsema, Chris. A physics based retrieval and quality assessment of bathymetry from suboptimal hyperspectral data. *Remote Sensing of Environment*, 113(4):755–770, 2009. ISSN 00344257.
- Bruzzone, Lorenzo and Melgani, Farid. Robust multiple estimator systems for the analysis of biophysical parameters from remotely sensed data. *IEEE Transactions on Geoscience and Remote Sensing*, 43:159–173, 2005. ISSN 01962892.
- Camps-Valls, Gustavo; Bruzzone, Lorenzo; Rojo-Álvarez, José L., and Melgani, Farid. Robust support vector regression for biophysical variable estimation from remotely sensed images. *IEEE Geoscience and Remote Sensing Letters*, 3:339–343, 2006. ISSN 1545598X.
- Cannizzaro, Jennifer Patch and Carder, Kendall L. Estimating chlorophyll a concentrations from remote-sensing reflectance in optically shallow waters. *Remote Sensing of Environment*, 101(1):13–24, 2006. ISSN 00344257.
- Chang, Chih-Chung and Lin, Chih-Jen. LIBSVM: a library for support vector machines. *ACM Transactions on Intelligent Systems and Technology (TIST)*, 2:27, 2011.
- Chauve, Adrien; Mallet, Clement; Bretar, Frederic; Durrieu, Sylvie; Deseilligny,

- Marc Pierrot; Puech, William; Sensing, Remote, and Sciences, Spatial Information. Processing full-waveform lidar data: modelling raw signals. *ISPRS Workshop on Laser Scanning 2007 and SivilLaser 2007*, 2004:102–107, September 2007. ISSN 03029743.
- Collin, A.; Archambault, P., and Long, B. Mapping the shallow water seabed habitat with the shoals. *IEEE Transactions on Geoscience and Remote Sensing*, 46(10):2947–2955, 2008.
- Cooley, T.; Anderson, G.P.; Felde, G.W.; Hoke, M.L.; Ratkowski, A.J.; Chetwynd, J.H.; Gardner, J.A.; Adler-Golden, S.M.; Matthew, M.W.; Berk, A.; Bernstein, L.S.; Acharya, P.K.; Miller, D., and Lewis, P. FLAASH, a MODTRAN4-based atmospheric correction algorithm, its applications and validation. *International Geoscience and Remote Sensing Symposium (IGARSS)*, 3:1414–1418, 2002.
- Cossio, Tristan; Slatton, Clint K.; Carter, William E.; Shrestha, Kristofer Y., and Harding, David. Predicting Topographic and Bathymetric Measurement Performance for Low-SNR Airborne Lidar. *IEEE Transactions on Geoscience and Remote Sensing*, 47(7): 2298–2315, 2009. ISSN 0196-2892.
- Costa, B.M.; Battista, T.A., and Pittman, S.J. Comparative evaluation of airborne lidar and ship-based multibeam sonar bathymetry and intensity for mapping coral reef ecosystems. *Remote Sensing of Environment*, 113(5):1082 – 1100, 2009. ISSN 0034-4257.
- Cui, Minshan and Prasad, Saurabh. Class-Dependent Sparse Representation Classifier for Robust Hyperspectral Image Classification. *IEEE Transactions on Geoscience and Remote Sensing*, 53:2683–2695, 2015. ISSN 0196-2892.
- Cui, Minshan; Prasad, Saurabh; Mahrooghy, Majid; Aanstoos, James V.; Lee, Matthew A., and Bruce, Lori M. Decision fusion of textural features derived from polarimetric data for levee assessment. *IEEE Journal of Selected Topics in Applied Earth Observations and Remote Sensing*, 5:970–976, 2012. ISSN 19391404.

- Dalponte, Michele; Bruzzone, Lorenzo, and Gianelle, Damiano. Fusion of Hyperspectral and LIDAR Remote Sensing Data for Classification of Complex Forest Areas. *IEEE Transactions on Geoscience and Remote Sensing*, 46:1416–1427, 2008. ISSN 0196-2892.
- Degnan, John J and Field, Christopher T. Moderate to high altitude, single photon sensitive, 3d imaging lidars. In *SPIE Sensing Technology+ Applications*, pages 91140H–91140H. International Society for Optics and Photonics, 2014.
- Dekker, Arnold G.; Phinn, Stuart R.; Anstee, Janet; Bissett, Paul; Brando, Vittorio E.; Casey, Brandon; Fearn, Peter; Hedley, John; Klonowski, Wojciech, and Lee, Zhong P. Intercomparison of shallow water bathymetry, hydro-optics, and benthos mapping techniques in Australian and Caribbean coastal environments. *Limnology and Oceanography: Methods*, 9:396–425, 2011. ISSN 15415856.
- Dierssen, Heidi M.; Zimmerman, Richard C.; Leathers, Robert A.; Downes, T. Valerie, and Davis, Curtiss O. Ocean color remote sensing of seagrass and bathymetry in the Bahamas Banks by high resolution airborne imagery. *Limnology and Oceanography*, 48:444–455, 2003. ISSN 00243590.
- Eugenio, F.; Marcello, J., and Martin, J. High-Resolution Maps of Bathymetry and Benthic Habitats in Shallow-Water Environments Using Multispectral Remote Sensing Imagery. *IEEE Transactions on Geoscience and Remote Sensing*, 53(7):3539–3549, 2015. ISSN 0196-2892.
- Fernandez-Diaz, Juan Carlos; Glennie, Craig L.; Carter, William E.; Shrestha, Ramesh L.; Sartori, Michael P.; Singhanian, Abhinav; Legleiter, Carl J., and Overstreet, Brandon T. Early Results of Simultaneous Terrain and Shallow Water Bathymetry Mapping Using a Single-Wavelength Airborne LiDAR Sensor. *IEEE Journal of Selected Topics in Applied Earth Observations and Remote Sensing*, 7:623–635, 2014. ISSN 1939-1404.

- Fonstad, Mark A and Marcus, W Andrew. Remote sensing of stream depths with hydraulically assisted bathymetry (hab) models. *Geomorphology*, 72(1):320–339, 2005.
- Fonstad, Mark J. *Fluvial Remote Sensing for Science and Management*, chapter 4: Hyperspectral Imagery in Fluvial Environments, pages 71–84. John Wiley and Sons, 2012.
- Gao, Bo-Cai; Montes, Marcos J.; Li, Rong-Rong; Dierssen, Heidi Melita, and Davis, Curtiss O. An Atmospheric Correction Algorithm for Remote Sensing of Bright Coastal Waters Using MODIS Land and Ocean Channels in the Solar Spectral Region. *IEEE Transactions on Geoscience and Remote Sensing*, 45:1835–1843, 2007. ISSN 0196-2892.
- Ghilani, Charles D. *Adjustment Computations: Spatial Data Analysis*. John Wiley & Sons, Inc., Hoboken, NJ, USA, March 2010. ISBN 9780470586266.
- Gitelson, Anatoly A; Gurlin, Daniela; Moses, Wesley J, and Barrow, Tadd. A bio-optical algorithm for the remote estimation of the chlorophyll-a concentration in case 2 waters. *Environmental Research Letters*, 4(4):045003, 2009. ISSN 1748-9326.
- Glennie, Craig. Rigorous 3D error analysis of kinematic scanning LIDAR systems. *Journal of Applied Geodesy*, 1, 2007. ISSN 1862-9016.
- Glennie, Craig L.; Carter, William E.; Shrestha, Ramesh L., and Dietrich, William E. Geodetic imaging with airborne LiDAR: the Earth's surface revealed. *Reports on Progress in Physics*, 76:86801, 2013.
- Gregoire, John M; Dale, Darren, and van Dover, R Bruce. A wavelet transform algorithm for peak detection and application to powder x-ray diffraction data. *The Review of scientific instruments*, 82:015105, 2011. ISSN 1089-7623.
- Guenther, Gary C. Airborne laser hydrography: System design and performance factors. Technical report, DTIC Document, 1985.

- Guenther, Gary C. *Digital Elevation Model Technologies and Applications: The DEM Users Manual*, chapter 8: Airborne Lidar Bathymetry, pages 253–320. American Society for Photogrammetry and Remote Sensing, 2006.
- Guenther, Gary C.; Thomas, Robert W. L., and LaRocque, Paul E. Design considerations for achieving high accuracy with the SHOALS bathymetric lidar system. *Proc. SPIE*, 2964:54–71, 1996.
- Guenther, Gary C.; Cunningham, A. Grant; LaRocque, Paul E., and Reid, David J. Meeting the accuracy challenge in airborne lidar bathymetry. *Proceedings of EARSeL-SIG-Workshop LiDAR, Dresden/FRG*, (1):1–27, June 2000.
- Habib, Ayman; Bang, Ki In; Kersting, Ana Paula, and Lee, Dong-Cheon. Error Budget of Lidar Systems and Quality Control of the Derived Data. *Photogrammetric Engineering & Remote Sensing*, 75(9):1093–1108, 2009. ISSN 00991112.
- Hartzell, Preston J.; Glennie, Craig L., and Finnegan, David C. Empirical Waveform Decomposition and Radiometric Calibration of a Terrestrial Full-Waveform Laser Scanner. *IEEE Transactions on Geoscience and Remote Sensing*, pages 1–11, 2014. ISSN 0196-2892.
- Hauser, Darren L. *Three-Dimensional Accuracy Analysis of a Mapping-Grade Mobile Laser Scanning System*. Master of Sciences, University of Houston, 2013.
- Hecht, Eugene. *Optics*. Addison Wesley, New York, 4th edition, 2002. ISBN 978-0805385663.
- Hedley, J. D.; Harborne, A. R., and Mumby, P. J. Technical note: Simple and robust removal of sun glint for mapping shallow water benthos. *International Journal of Remote Sensing*, 26(10):2107–2112, 2005. ISSN 0143-1161.

- Heil, Christopher E. and Walnut, David F. Continuous and discrete wavelet transforms. *SIAM Review*, 31(4):628–666, 1989. ISSN 00361445.
- Hickman, G. Daniel and Hogg, John E. Application of an airborne pulsed laser for near shore bathymetric measurements. *Remote Sensing of Environment*, 1(1):47–58, 1969. ISSN 0034-4257.
- Hossain, M.S.; Bujang, J.S.; Zakaria, M.H., and Hashim, M. The application of remote sensing to seagrass ecosystems: an overview and future research prospects. *International Journal of Remote Sensing*, 36:61–114, 2014. ISSN 0143-1161.
- Irish, J.L. and Lillycrop, W.J. Scanning laser mapping of the coastal zone: the shoals system. *ISPRS Journal of Photogrammetry and Remote Sensing*, 54(23):123–129, 1999. ISSN 0924-2716.
- Irish, J.L.; McClung, J.K., and Lillycrop, W.J. Airborne lidar bathymetry-the shoals system. *Bulletin-International Navigation Association*, pages 43–54, 2000.
- Jay, S. and Guillaume, M. Regularized estimation of bathymetry and water quality using hyperspectral remote sensing. *International Journal of Remote Sensing*, 37(2):263–289, 2016. ISSN 0143-1161.
- Jay, Sylvain and Guillaume, Mireille. A novel maximum likelihood based method for mapping depth and water quality from hyperspectral remote-sensing data. *Remote Sensing of Environment*, 147:121–132, 2014. ISSN 00344257.
- Jung, J. and Crawford, M.M. Extraction of features from lidar waveform data for characterizing forest structure. *IEEE Geoscience and Remote Sensing Letters*, 9(3):492–496, 2012. ISSN 1545-598X.
- Kanno, Ariyo and Tanaka, Yoji. Modified lyzenga’s method for estimating generalized

- coefficients of satellite-based predictor of shallow water depth. *IEEE Geoscience and Remote Sensing Letters*, 9(4):715–719, 2012. ISSN 1545598X.
- Kim, Angela M.; Runyon, Scott C., and Olsen, Richard C. Comparison of full-waveform, single-photon sensitive, and discrete analog lidar data. *Proc. SPIE*, 9465:94650L–94650L–10, 2015.
- LaRocque, Paul E and West, Geraint R. Airborne laser hydrography: an introduction. In *Proc. ROPME/PERSGA/IHB Workshop on Hydrographic Activities in the ROPME Sea area and Red Sea*, volume 4, pages 1–15, 1999.
- Lee, Zhongping; Carder, Kendall L.; Mobley, Curtis D.; Steward, Robert G., and Patch, Jennifer S. Hyperspectral remote sensing for shallow waters. I. A semianalytical model. *Applied optics*, 37(27):6329–6338, 1998. ISSN 0003-6935.
- Lee, Zhongping; Carder, Kendall L.; Mobley, Curtis D.; Steward, Robert G., and Patch, Jennifer S. Hyperspectral Remote Sensing for Shallow Waters. 2. Deriving Bottom Depths and Water Properties by Optimization. *Applied Optics*, 38(18):3831, 1999. ISSN 0003-6935.
- Lee, Zhongping; Carder, Kendall L.; Chen, Robert F., and Peacock, Thomas G. Properties of the water column and bottom derived from Airborne Visible Infrared Imaging Spectrometer (AVIRIS) data. *Journal of Geophysical Research: Oceans*, 106(C6):11639–11651, 2001. ISSN 01480227.
- Legleiter, C.; Marcus, W.A., and Lawrence, R. Effects of sensor resolution on mapping instream habitats. *Photogrammetric Engineering and Remote Sensing*, 68(8):801–807, 2002.
- Legleiter, Carl J. Calibrating remotely sensed river bathymetry in the absence of field measurements: Flow REsistance Equation-Based Imaging of River Depths (FREEBIRD).

- Water Resources Research*, 51(4):2865–2884, 2015. ISSN 00431397.
- Legleiter, Carl J and Goodchild, Michael F. Alternative representations of in-stream habitat: classification using remote sensing, hydraulic modeling, and fuzzy logic. *International Journal of Geographical Information Science*, 19(1):29–50, 2005.
- Legleiter, Carl J.; Roberts, Dar A.; Marcus, W. Andrew, and Fonstad, Mark A. Passive optical remote sensing of river channel morphology and in-stream habitat: Physical basis and feasibility. *Remote Sensing of Environment*, 93(4):493–510, 2004. ISSN 00344257.
- Legleiter, Carl J; Roberts, Dar A, and Lawrence, Rick L. Spectrally based remote sensing of river bathymetry. *Earth Surface Processes and Landforms*, 34:1039–1059, 2009. ISSN 01979337.
- Legleiter, Carl J.; Overstreet, Brandon T.; Glennie, Craig L.; Pan, Zhigang; Fernandez-Diaz, Juan Carlos, and Singhanian, Abhinav. Evaluating the capabilities of the CASI hyperspectral imaging system and Aquarius bathymetric LiDAR for measuring channel morphology in two distinct river environments. *Earth Surface Processes and Landforms*, pages n/a–n/a, 2015. ISSN 1096-9837.
- Lyons, Mitchell; Phinn, Stuart, and Roelfsema, Chris. Integrating Quickbird Multi-Spectral Satellite and Field Data: Mapping Bathymetry, Seagrass Cover, Seagrass Species and Change in Moreton Bay, Australia in 2004 and 2007. *Remote Sensing*, 3:42–64, 2011. ISSN 2072-4292.
- Lyzenga, David R. Passive remote sensing techniques for mapping water depth and bottom features. *Applied Optics*, 17:379–383, 1978.
- Lyzenga, D.R.; Malinas, N.P., and Tanis, F.J. Multispectral bathymetry using a simple physically based algorithm. *IEEE Transactions on Geoscience and Remote Sensing*, 44(8):2251–2259, 2006. ISSN 0196-2892.

- Ma, Li; Crawford, Melba M., and Tian, Jinwen. Local manifold learning-based k-nearest-neighbor for hyperspectral image classification. *IEEE Transactions on Geoscience and Remote Sensing*, 48:4099–4109, 2010. ISSN 01962892.
- Ma, Sheng; Tao, Zui; Yang, Xiaofeng; Yu, Yang; Zhou, Xuan, and Li, Ziwei. Bathymetry retrieval from hyperspectral remote sensing data in optical-shallow water. *IEEE Transactions on Geoscience and Remote Sensing*, 52:1205–1212, 2014. ISSN 01962892.
- Marcus, W. Andrew and Fonstad, Mark A. Remote sensing of rivers: The emergence of a subdiscipline in the river sciences. *Earth Surface Processes and Landforms*, 35(15): 1867–1872, 2010. ISSN 01979337. doi: 10.1002/esp.2094.
- McKean, Jim; Nagel, Dave; Tonina, Daniele; Bailey, Philip; Wright, Charles Wayne; Bohn, Carolyn, and Nayegandhi, Amar. Remote Sensing of Channels and Riparian Zones with a Narrow-Beam Aquatic-Terrestrial LIDAR. *Remote Sensing*, 1:1065–1096, 2009. ISSN 2072-4292.
- Mobley, Curtis D. *Light and Water: Radiative Transfer in Natural Waters*. Academic Press, 1994. ISBN 978-0125027502.
- Mobley, Curtis D.; Sundman, Lydia K.; Davis, Curtiss O.; Bowles, Jeffrey H.; Downes, Trijntje Valerie; Leathers, Robert A.; Montes, Marcos J.; Bissett, William Paul; Kohler, David D. R.; Reid, Ruth Pamela; Louchard, Eric M., and Gleason, Arthur. Interpretation of hyperspectral remote-sensing imagery by spectrum matching and look-up tables. *Applied Optics*, 44(17):3576–3592, Jun 2005.
- Morel, Andre. Optical properties of pure water and pure sea water. *Optical aspects of oceanography*, 1:1–24, 1974.
- Mountrakis, G.; Im, J., and Ogole, C. Support vector machines in remote sensing: A review. *ISPRS Journal of Photogrammetry and Remote Sensing*, 66:247–259, 2011.

- Mumby, P.J.; Green, E.P.; Edwards, A.J., and Clark, C.D. The cost-effectiveness of remote sensing for tropical coastal resources assessment and management. *Journal of Environmental Management*, 55(3):157 – 166, 1999. ISSN 0301-4797.
- Oliver, Jonathan J.; Baxter, Rohan A., and Wallace, Chris S. Unsupervised learning using MML. *ICML*, 1996.
- O'Reilly, John E.; Maritorena, Stéphane; Mitchell, B. Greg; Siegel, David A.; Carder, Kendall L.; Garver, Sara A.; Kahru, Mati, and McClain, Charles. Ocean color chlorophyll algorithms for SeaWiFS. *Journal of Geophysical Research: Oceans*, 103(C11): 24937–24953, 1998. ISSN 01480227.
- Pacheco, A.; Horta, J.; Loureiro, C., and Ferreira, O. Retrieval of nearshore bathymetry from Landsat 8 images: A tool for coastal monitoring in shallow waters. *Remote Sensing of Environment*, 159:102 – 116, 2015. ISSN 0034-4257.
- Pan, Zhigang; Glennie, Craig; Legleiter, Carl, and Overstreet, Brandon. Estimation of Water Depths and Turbidity From Hyperspectral Imagery Using Support Vector Regression. *IEEE Geoscience and Remote Sensing Letters*, 12(10):2165–2169, 2015a. ISSN 1545-598X.
- Pan, Zhigang; Glennie, Craig L.; Hartzell, Preston J.; Fernandez-Diaz, Juan Carlos; Legleiter, Carl J., and Overstreet, Brandon T. Performance assessment of high resolution airborne full waveform LiDAR for bathymetry. *Remote Sensing*, 7:5133–5159, 2015b.
- Pan, Zhigang; Glennie, Craig; Fernandez-Diaz, Juan Carlos, and Starek, Michael. Comparison of bathymetry and seagrass mapping with hyperspectral imagery and airborne bathymetric lidar in a shallow estuarine environment. *International Journal of Remote Sensing*, 37(3):516–536, 2016a. ISSN 0143-1161.

- Pan, Zhigang; Glennie, Craig L.; Fernandez-Diaz, Juan Carlos; Legleiter, Carl J., and Overstreet, Brandon. Fusion of LiDAR Orthowaveforms and Hyperspectral Imagery for Shallow River Bathymetry and Turbidity Estimation. *IEEE Transactions on Geoscience and Remote Sensing*, pages 1–13, 2016b. ISSN 0196-2892.
- Paringit, E. C. and Nadaoka, K. Simultaneous estimation of benthic fractional cover and shallow water bathymetry in coral reef areas from high-resolution satellite images. *International Journal of Remote Sensing*, 33(10):3026–3047, 2012.
- Park, Joong Yong; Ramnath, Vinod; Feygels, Viktor; Kim, Minsu; Mathur, Abhinav; Aitken, Jennifer, and Tuell, Grady. Active-passive data fusion algorithms for seafloor imaging and classification from CZMIL data. In *SPIE Defense, Security, and Sensing*, volume 7695, page 769515. International Society for Optics and Photonics, 2010. ISBN 9780819481597.
- Park, Joong Yong; Ramnath, Vinod., and Tuell, Grady. Using lidar waveforms to detect environmental hazards through visualization of the water column. In *OCEANS 2014 - TAIPEI*, pages 1–5, April 2014.
- Parrish, Christopher E.; Jeong, Inseong; Nowak, Robert D., and Brent Smith, R. Empirical comparison of full-waveform lidar algorithms: Range extraction and discrimination performance. *Photogrammetric Engineering and Remote Sensing*, 77(8):825–838, 2011. ISSN 00991112.
- Parrish, Christopher E.; Rogers, Jeffrey N., and Calder, Brian R. Assessment of Waveform Features for Lidar Uncertainty Modeling in a Coastal Salt Marsh Environment. *IEEE Geoscience and Remote Sensing Letters*, 11:569–573, 2014. ISSN 1545-598X.
- Persson, Å; Söderman, U; Töpel, J, and Ahlberg, S. Visualization and analysis of full-waveform airborne laser scanner data. *International Archives of Photogrammetry*, 2005.

- Pfennigbauer, Martin; Ullrich, Andreas; Steinbacher, Frank, and Aufleger, Markus. High-resolution hydrographic airborne laser scanner for surveying inland waters and shallow coastal zones. *Proc. SPIE*, 8037:803706–803706–11, 2011.
- Philpot, William D. Bathymetric mapping with passive multispectral imagery. *Applied Optics*, 28:1569–1578, 1989.
- Pope, Robin M. and Fry, Edward S. Absorption spectrum (380-700 nm) of pure water II Integrating cavity measurements. *Applied Optics*, 36(33):8710, nov 1997. ISSN 0003-6935.
- Richardson, Laurie L. and LeDrew, Ellsworth F. *Remote sensing of aquatic coastal ecosystem processes*, volume 9 of *Remote Sensing and Digital Image Processing*. Springer Netherlands, Dordrecht, 2006. ISBN 978-1-4020-3967-6.
- Rogers, Jeffrey N.; Parrish, Christopher E.; Ward, Larry G., and Burdick, David M. Evaluation of field-measured vertical obscuration and full waveform lidar to assess salt marsh vegetation biophysical parameters. *Remote Sensing of Environment*, 156:264 – 275, 2015. ISSN 0034-4257.
- Sandidge, Juanita C. and Holyer, Ronald J. Coastal bathymetry from hyperspectral observations of water radiance. *Remote Sensing of Environment*, 65:341–352, 1998. ISSN 00344257.
- Shrestha, Kristofer Y.; Carter, William E.; Slatton, Clint K., and Cossio, Tristan K. Shallow Bathymetric Mapping via Multistop Single Photoelectron Sensitivity Laser Ranging. *IEEE Transactions on Geoscience and Remote Sensing*, 50(11):4771–4790, 2012. ISSN 0196-2892.
- Smola, Alex and Vapnik, Vladimir. Support vector regression machines. *Advances in Neural Information Processing Systems*, 9:155–161, 1997.

- Smola, Alex J and Schölkopf, Bernhard. A tutorial on support vector regression. *Statistics and computing*, 14:199–222, 2004.
- Stumpf, Richard P.; Holderied, Kristine, and Sinclair, Mark. Determination of water depth with high-resolution satellite imagery over variable bottom types. *Limnology and Oceanography*, 48:547–556, 2003. ISSN 00243590.
- Torres-Madronero, Maria C.; Velez-Reyes, Miguel, and Goodman, James A. Fusion of hyperspectral imagery and bathymetry information for inversion of biooptical models. *Proc. SPIE*, 7473:74730I–74730I–11, 2009.
- Torres-Madronero, Maria C.; Velez-Reyes, Miguel, and Goodman, James A. Subsurface unmixing for benthic habitat mapping using hyperspectral imagery and lidar-derived bathymetry. *Proceedings of SPIE - The International Society for Optical Engineering*, 9088, 2014.
- Tuell, Grady; Barbor, Kenneth, and Wozencraft, Jennifer. Overview of the coastal zone mapping and imaging lidar (CZMIL): a new multisensor airborne mapping system for the US Army Corps of Engineers. In *SPIE Defense, Security, and Sensing*, pages 76950R–76950R. International Society for Optics and Photonics, 2010.
- Tuell, Grady H. and Park, Joong Yong. Use of SHOALS bottom reflectance images to constrain the inversion of a hyperspectral radiative transfer model. *Proc. SPIE*, 5412: 185–193, 2004.
- Vetterli, Martin and Herley, Cormac. Wavelets and filter banks: Theory and design. *IEEE Transactions on Signal Processing*, 40(9):2207–2232, 1992. ISSN 1053587X.
- Wagner, Wolfgang; Ullrich, Andreas; Ducic, Vesna; Melzer, Thomas, and Studnicka, Nick. Gaussian decomposition and calibration of a novel small-footprint full-waveform digitising airborne laser scanner. *ISPRS Journal of Photogrammetry and Remote Sensing*,

- 60(2):100–112, 2006. ISSN 09242716.
- Wang, Chi-Kuei and Philpot, William D. Using airborne bathymetric lidar to detect bottom type variation in shallow waters. *Remote Sensing of Environment*, 106:123–135, 2007. ISSN 00344257.
- Wang, Chisheng; Li, Qingquan; Liu, Yanxiong; Wu, Guofeng; Liu, Peng, and Ding, Xiaoli. A comparison of waveform processing algorithms for single-wavelength LiDAR bathymetry. *ISPRS Journal of Photogrammetry and Remote Sensing*, 101:22–35, 2015. ISSN 09242716.
- Wang, Hongzhou and Glennie, Craig. Fusion of waveform LiDAR data and hyperspectral imagery for land cover classification. *ISPRS Journal of Photogrammetry and Remote Sensing*, 108:1–11, 2015. ISSN 09242716.
- Wilson, Margaret F.J.; O’Connell, Brian; Brown, Colin; Guinan, Janine C., and Grehan, Anthony J. Multiscale terrain analysis of multibeam bathymetry data for habitat mapping on the continental slope. *Marine Geodesy*, 30(1-2):3–35, 2007.
- Wu, Jiaying; van Aardt, J. A. N., and Asner, Gregory P. A Comparison of Signal Deconvolution Algorithms Based on Small-Footprint LiDAR Waveform Simulation. *IEEE Transactions on Geoscience and Remote Sensing*, 49(6):2402–2414, 2011. ISSN 0196-2892.

